Development of deep-red and near-infrared organic luminescent materials and their applications in organic light-emitting diodes and continuous-wave organic semiconductor lasers

叶, 浩

2019

Doctor thesis

Development of deep-red and near-infrared organic luminescent materials and their applications in organic light-emitting diodes and continuous-wave organic semiconductor lasers

Hao Ye

Department of Applied Chemistry
Graduate School of Engineering
Kyushu University

Table of contents

Chapter 1

Introduction

1-1. History of organic light-emitting diodes

The first electroluminescence (EL) in organic materials was reported by Pope et al. from an anthracene and a tetracene-doped anthracene crystal by recombination of electrons and holes in 1963 with a quite high driving voltage of over 400 V [1], which was far from practical application. After that, many attempts mainly based on organic single crystals required still high driving voltage of over 50 V to obtain bright EL [2-16]. Thus, it was natural to look for ways of fabricating very thin organic layers without sacrificing excellent electrical and optical properties of single crystals. Some studies of EL in an anthracene thin film made by Langmuir-Blodgett technique were reported [17-20], but in most cases, the current densities achieved appear to be too low to give significant EL brightness. After that, the very first EL based on a vacuum deposited anthracene film was reported by Vincett et al. in 1982 [21]. By using the thinnest samples with the thickness of about 180 nm, EL was visible with a naked eye in a darkened room at voltages as low as 12 V. This is the first report showing visible EL clearly from an organic material at voltages significantly below 50 V. Further, Hayashi et al. reported the threshold voltage of an EL device down to 4 V by using poly(3-methylthiophene) (P3MT) as a hole-injection layer (HIL) and a vacuum deposited perylene film as an emission layer (EML) in 1986 [22], which is the first practical multi-layered organic EL device. Later, Tang and VanSlyke demonstrated efficient EL by using tris(8-hydroxyquinoline) aluminum (Alq_3) as an EML, and 4,4'-cyclohexylidenebis[*N*,*N*-bis(4-methylphenyl)benzenamine] (TAPC) as a hole-transport layer (HTL) in 1987 [23]. Light emission, seen only in forward bias, was measurable from as low as about 2.5 V, and can be driven to produce high brightness (> 1000 cd/m^2) with a direct current voltage of less than 10 V and high external quantum efficiency (EQE) about 1%. After that, a multi-layered organic EL device has been called as organic light-emitting diodes (OLEDs). Here, in these reports, the two-layer-type organic EL devices

consisted of one layer with only unipolar injection or transport. To balance the charge injection, Adachi et al. reported a fundamental sandwiched three-layer structure consisting of a HTL, an EML and an electron-transport layer (ETL) in 1988 [24, 25]. Due to the ideal confinement of charge carries and excitons in three-layer structures, stable and bright OLEDs were developed. Further, Tang et al. demonstrated a doping technique by coevaporating Alq_3 as a host matrix and a small amount (<1 mol%) of the fluorescent dopant, either 4-(dicyanomethylene)-2-methyl-6-(4-dimethylaminostyryl)-4*H*-pyran (DCM) or 3-(2-benzothiazolyl)-7-(diethylamino)-2*H*-1-benzopyran-2-one (Coumarin 540) as the guest to allow the Förster resonance energy transfer (FRET) from the host to guest in 1989. This OLED exhibited emission from the dopant with a further boosted EQE of 2.5%, while an undoped green emitting device showed a lower EQE of 1.0% [26]. After that, multi-layered structures and host-guest system have been widely adopted in state-of-the-art OLEDs to achieve high EQE and stable devices.

The principle of OLEDs involves charge injection from the electrodes, transport of charge carriers, and recombination of holes and electrons to form two types of excitons under electrical excitation, i.e., singlet and triplet excitons with a ratio of 1:3 based on their spin statistics [27]. The OLED efficiency, EQE (η_{ext}), is an important factor for evaluating device performance, and is defined as the ratio of the number of extracted photons out of the device to the total number of injected electrons, which can be calculated by eq. 1-1:

$$\eta_{ext} = \eta_r \cdot \chi \cdot \Phi_{PL} \cdot \eta_{out}, \qquad \text{(eq. 1-1)}$$

where η_r is the charge carrier balance factor (~ 100%), determined by the fraction of formed excitons and injected charge carriers, and can be brought close to unity if appropriate injection and blocking layers are used in the corresponding OLED. χ is the spin statistic factor (~ 100%), indicating the ratio of excitons which can radiatively decay. Φ_{PL} is the photoluminescence quantum yield (PLQY, ~ 100%) of organic luminescent emitter. η_{out} is the light outcoupling

factor (20 ~ 40%), related to the amount of photons that can be extracted from the device.

The first generation OLED is referred to as a fluorescent OLED based on the radiative recombination of singlet excitons. Since only 25% of the generated excitons, i.e., singlets, participate in the emission while the rest of the excitons, i.e., triplets, nonradiatively decay in the form of heat, the EQE is limited to 5% for the fluorescent OLEDs. Later, Baldo et al. found a mechanism that utilizes the triplet excitons to luminescence by an efficient singlet-triplet mixing via strong spin-orbit coupling (SOC) in heavy metal-based, light-emitting organic complexes by employing organometallic compounds in 1998 [28]. All the singlet excitons can rapidly transfer to the triplet state by intersystem crossing (ISC) process and the generated triplet excitons decay radiatively. The devices exploiting such a mechanism are called phosphorescent OLEDs (PHOLEDs). Later, Adachi et al. realized nearly 100% internal quantum efficiency (IQE) by using bis(2-phenylpyridine)iridium(III) acetylacetonate [$(ppy)_2Ir(acac)$] doped into 3-phenyl-4(1'-naphthyl)-5-phenyl-1,2,4-triazole (TAZ) in 2001. A maximum EQE of (19.0 ± 1.0)% and luminous power efficiency of (60 ± 5) lm/W were achieved [29]. The PHOLED is referred to the second generation OLED, and the high efficiency PHOLEDs have been widely used in commercial products such as flat panel display. However, PHOLEDs containing transition metal-based compounds are rather expensive and unsustainable because they contain rare metals. To avoid the high-cost of these phosphors hindered the prospective applications of these devices in displays, a promising alternative to phosphorescence to convert triplet excitons into light had been firstly proposed by Adachi group in 2009 [30]. Later, Adachi et al. reported the green OLED with a high EQE = 19.5% with an emission peak at 520 nm which is comparable to the best PHOLEDs by using an efficient thermally-activated delayed fluorescence (TADF) emitter-1,2,3,5-tetrakis(carbazol-9-yl)-4,6-dicyanobenzene (4CzIPN) in 2012 [31]. Here, delayed fluorescence is the radiative

transition from a lowest singlet excited-state (S_1) to a ground-state (S_0) involving ISC and lowest triplet excited-state (T_1) to S_1 endothermic reverse intersystem crossing (RISC) processes as shown in Figure 1-1. This process displays the same spectrum with the prompt fluorescence. However, its decay time is longer than that of the prompt fluorescence because a molecule emits as light emission after accompanying the ISC and RISC processes. The advantage of TADF molecules owes to the perfect conversion of 75% electrically generated triplet excitons to singlet excitons to realize 100% internal EL quantum efficiency. The TADF OLED is now referred to the third generation OLED. The fluorescence, phosphorescence, and delayed fluorescence in accordance with different radiative decay processes are shown in Figure 1-1.

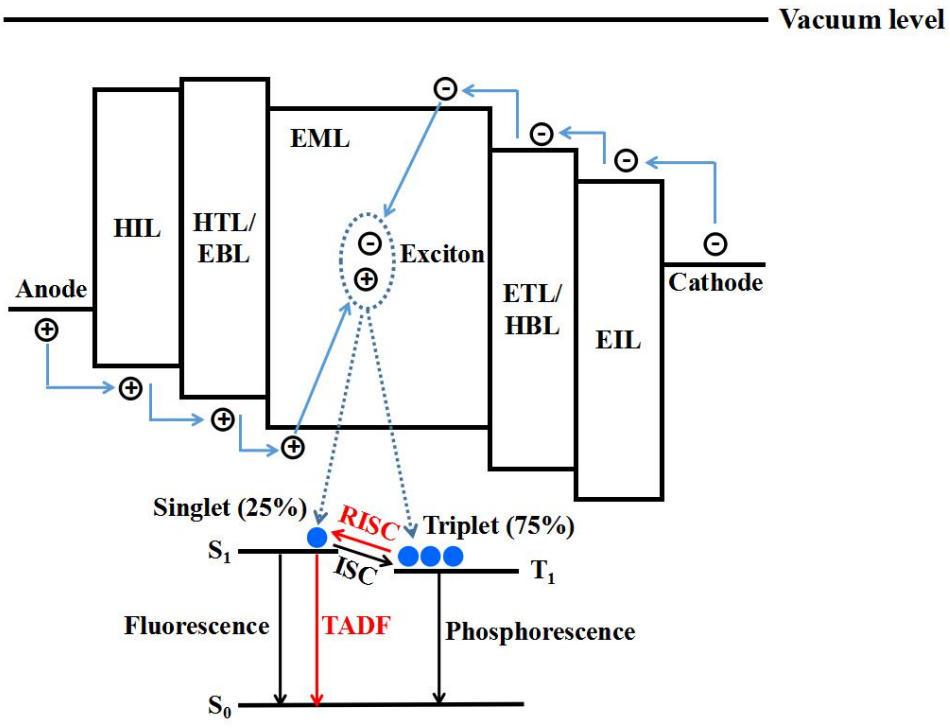

Figure 1-1. Operation principle of OLED. (HIL: hole-injection layer, HTL: hole-transport layer, EBL: electron-blocking layer, EML: emission layer, HBL: hole-blocking layer, ETL: electron-transport layer, EIL: electron-injection layer, S_1: lowest singlet excited-state, T_1: lowest triplet excited-state, S_0: ground-state, ISC: intersystem crossing, RISC: reverse intersystem crossing, and TADF: thermally-activated delayed fluorescence)

Although OLEDs fabricated by vacuum deposition of organic thin-film layers usually have good efficiency and multi-emission colors, there have been general problems associated with the long-term stability of the deposition films against recrystallization, high material cost, and high-cost device fabrication procedures based on vacuum deposition. Instead, Burroughes et al. utilized conjugated polymers as an active material in OLEDs, and demonstrated OLED fabrication based on wet-processing in 1990 [32]. This study demonstrated high potential of solution processing and a considerable amount of effort has been devoted to improve the efficiency and stability of OLEDs. Figure 1-2 shows the number of citations per year for the key words of "organic" and "electroluminescence" according to Web of Science [33], indicating that every breakthrough accelerates OLED research and development (R&D) significantly.

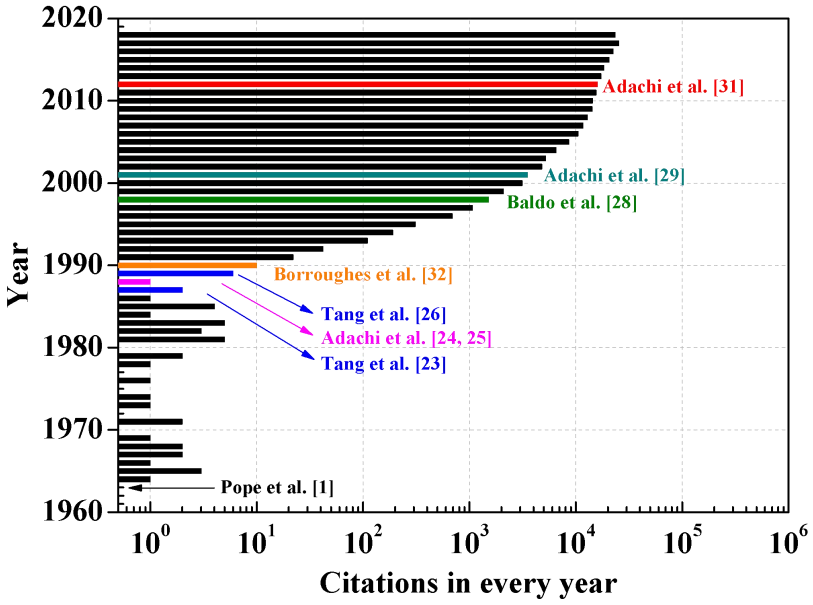

Figure 1-2. Evolution of citations in OLED R&D with breakthrough works highlighted in the corresponding year according to the Web of Science as of December 2018 [33].

Recently, extension of the spectrum of OLEDs from visible to deep-red and near-infrared (NIR) has commanded attention from both the academic and the industrial sector for their potential in display (e.g. night-vision devices, capillary mapping in identification systems, etc.)

[34, 35], medical (e.g. photodynamic therapy) [36], sensor (e.g. oxymetry) [37], and optical communication [38] as shown in Figure 1-3, which makes them become a new target in the field of OLED R&D.

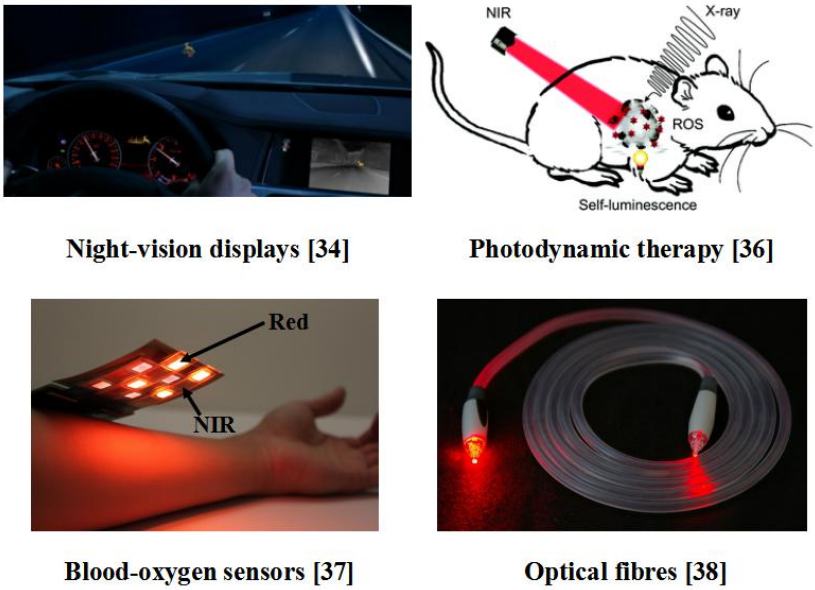

Figure 1-3. Applications of deep-red and NIR light technology.

For deep-red and NIR emitters, the PLQY values tend to decrease as the emission wavelengths increase according to the energy-gap law [39], which predicts that the quantum efficiency of organic emitter decreases as the energy-gap is reduced, owing to the increment of radiationless transitions. Additionally, many deep-red and NIR compounds exhibit weak or no emission in their neat film as a result of strong aggregation-caused quenching (ACQ) [40]. Although EQEs spanning from 5% to 24% have been achieved in OLEDs incorporating phosphorescent Pt-based porphyrins and carefully-designed derivatives with the EL wavelength between 705 to 773 nm [41-45], the use of expensive, toxic heavy metals and triplet related annihilation (e.g. serious efficiency rolloff with the increasing current density owing to the long-lived triplet excitons, etc.) have intrinsically limited the scope and applicability of phosphorescent OLEDs. In this regard, deep-red and NIR OLEDs based on pure organic

luminescent materials prove their advantages, since they do not need heavy metals and may effectively avoid the quenching of long-lived triplet excitons, especially for TADF molecules, which allow efficient upconversion of triplet excitons into a singlet state by RISC process. Significant efforts have been made to develop novel material systems to improve the efficiency of deep-red and NIR OLEDs, such as donor (D)-acceptor (A)-donor (D) type compounds [46-48], conjugated polymers [49], and exciplexes [50] as highlighted with molecular structures in Figures 1-4 and 1-5 and the EQE, and EL peak summarized in Table 1-1. However, it is still a challenge for researchers to develop efficient further NIR TADF molecules. The main reason is because simultaneously achieving a sufficiently small energy-gap (ΔE_{ST}) value between the S_1 and T_1 states and a large fluorescence radiative decay rate (k_r) in one molecule is inherently difficult. The limited orbital overlap required to obtain a small ΔE_{ST} value would generally lead to a low k_r, which is detrimental to the obtainment of a high PLQY for the system due to competition from radiationless transitions. In this thesis, I endeavor to overcome these problems through molecular design and improve the efficiency of NIR OLEDs.

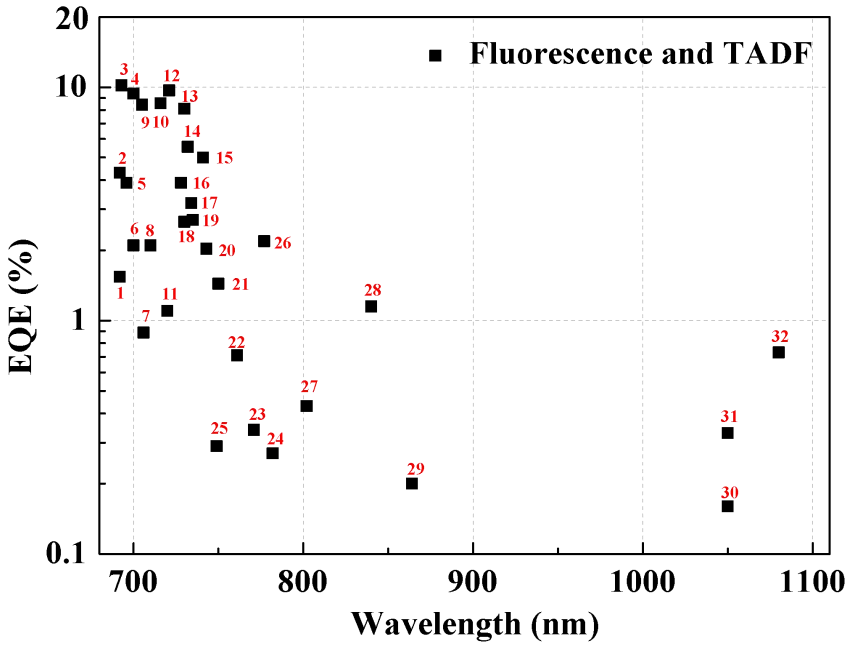

Figure 1-4. State-of-the-art of pure organic luminescent materials for deep-red and NIR OLEDs [46-58].

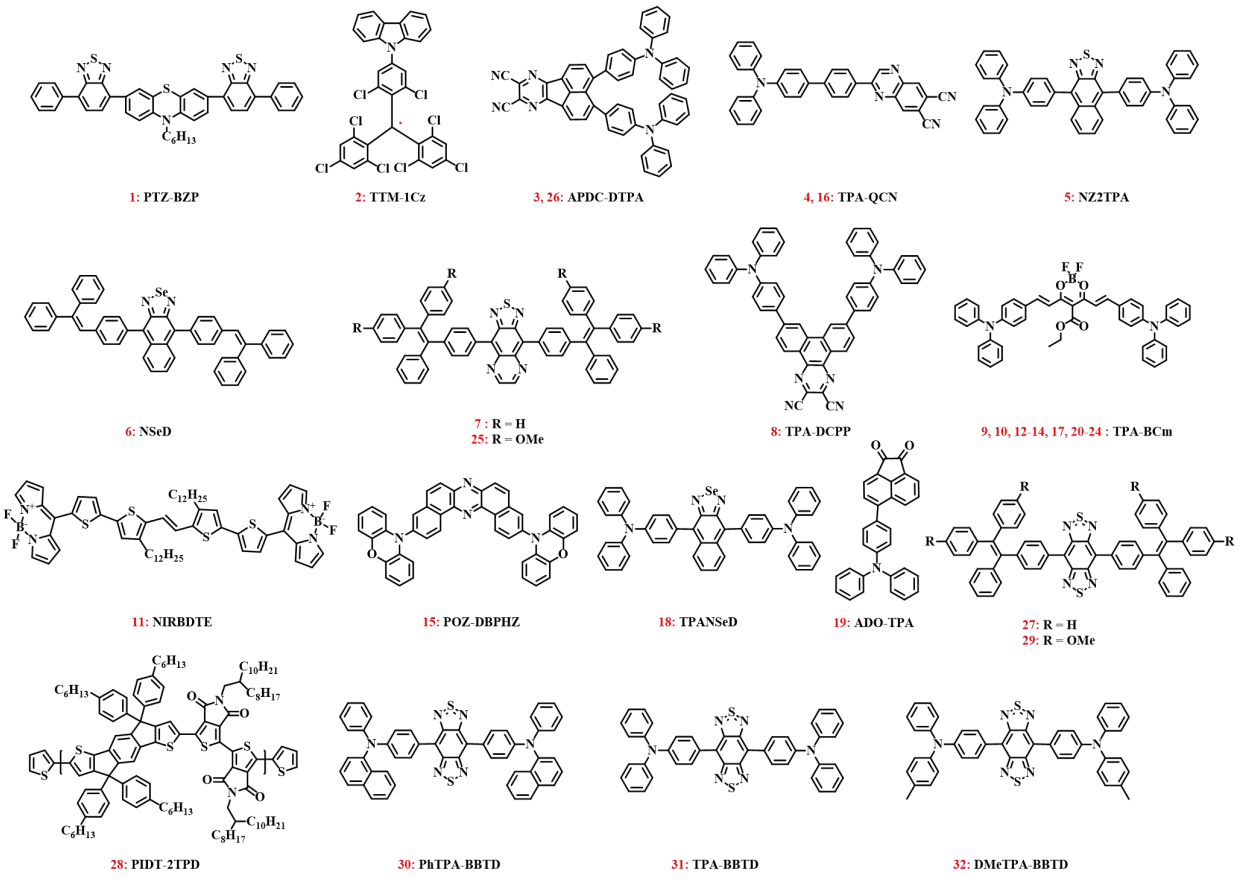

Figure 1-5. Structures of molecules 1-32 [46-58].

Table 1-1. Summary of the maximum EQE and EL peak in molecules 1-32 [46-58].

	1	**2**	**3**	**4**	**5**	**6**	**7**	**8**
Peak (nm)	692	692	693	700	696	700	706	710
EQE (%)	1.54	4.3	10.19	9.4	3.9	2.1	0.89	2.1
	9	**10**	**11**	**12**	**13**	**14**	**15**	**16**
Peak (nm)	705	716	720	721	730	732	741	728
EQE (%)	8.41	8.53	1.1	9.69	8.09	5.56	5	3.9
	17	**18**	**19**	**20**	**21**	**22**	**23**	**24**
Peak (nm)	734	730	735	743	750	761	771	782
EQE (%)	3.19	2.65	2.7	2.03	1.44	0.71	0.34	0.27
	25	**26**	**27**	**28**	**29**	**30**	**31**	**32**
Peak (nm)	749	777	802	840	864	1050	1050	1080
EQE (%)	0.29	2.19	0.43	1.15	0.2	0.16	0.33	0.73

1-2. History of organic lasers

The history of organic lasers is almost as long as the history of OLEDs, since the first stimulated emission from organic material was reported by Sorokin et al. in March 1966 [59], followed by Schafer et al. reported the first organic laser in September 1966 [60]. This work marked a true revolution in laser science, leading to a significant success in spectroscopy in the following years [61]. Later, the continuous-wave (CW) operation was demonstrated by Peterson et al. in 1970 [62], which opened the door to the development of the first ultrashort laser [63, 63] and the application of optical tweezers [65] which awarded the Nobel Prize in Physics 2018 [66]. However, most of the devices used the solution of π-conjugated highly luminescent molecules as the medium, which were sometimes inconvenience to solid-state applications. The first solid-state laser was proposed in 1967, with incorporating the laser dyes in solid-state polymeric matrices, indicating that these devices have the benefit to convenient, compact light source with low cost [67]. However, the very first stimulated emission from solid-state has not been realized until 1990s. The first organic solid-state semiconductor laser (OSSL) was demonstrated by Hide et al. under optical pulse pumping in 1996 [68], and the lasing from solid-state conjugated-polymer microcavities was also reported by Tessler et al. at the same year [69]. Subsequently, many works then focused on improving the dye and host matrix photostability, decreasing the required pump threshold intensity, operating under the CW condition, and even realizing organic semiconductor laser diodes (OSLDs). The first optically pumped quasi-CW lasers from organic solid-state films was realized by Rabe et al. in 2006 [70], and a indirect electrical pumping OSSL was reported by Samuel et al. in 2008 [71]. Samuel et al. used LEDs as a pumping light source. This work was important progress in solid-state coherent light source technology. However, no direct OSLDs which will realize a new class of extremely compact, tunable, cheap, and flexible lasers have been reported.

Inspiringly, Sandanayaka et al. demonstrated low threshold surface-emitting organic distributed feedback (DFB) lasers operating in the quasi-CW regime at 80 MHz as well as under long pulse photo-excitation of 30 ms in 2017 [72]. This outstanding performance was achieved using an organic semiconductor thin film with high optical gain, high PLQY, and no triplet absorption loss at the lasing wavelength combined with a mixed-order DFB grating to achieve a low lasing threshold. A simple encapsulation technique greatly reduced the laser-induced thermal degradation and suppressed the ablation of the gain medium. This study provides evidence that the realization of a CW OSSLs or OSLDs is possible via the development of the gain medium and engineering of the device architecture.

The history of organic lasers is briefly summarized in Figure 1-6. The considerable efforts have been done since the first reported stimulated emission from organic luminescent material in 1966. During the last 22 years, solid-state organic thin film lasers have been widely studied. In near future, we can expect that an electrically driven OSLDs will drive the world of new light creation applications.

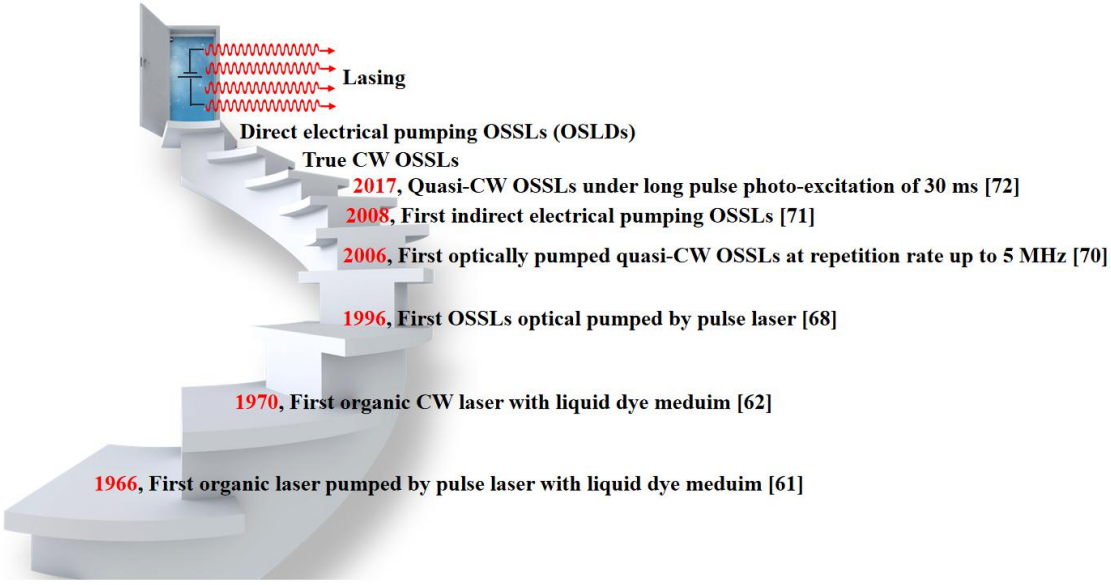

Figure 1-6. History of organic lasers with some breakthrough works. (CW: continuous-wave, OSSLs: organic solid-state semiconductor lasers, and OSLDs: organic semiconductor laser diodes)

1-3. Principle of laser

1-3-1. Basic of molecular design for organic lasers

The word of "laser" stands for the abbreviation for "Light Amplification by Stimulated Emission of Radiation", and it consists basically of three processes, (1) Excitation: excitation of molecules optically or electrically, (2) Light amplification: population inversion in gain medium, and (3) Optical confinement: cavities and resonators based on mirrors for optical confinement to obtain coherent characteristics.

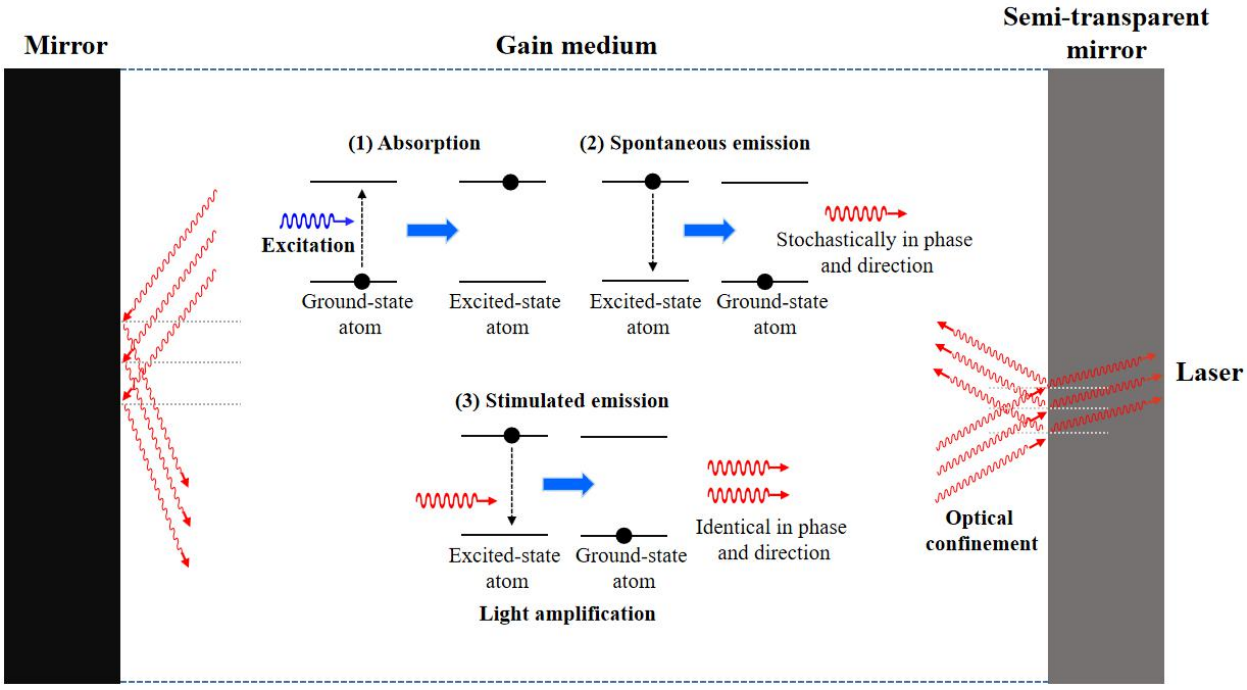

Figure 1-7. Schematic illustration of light-matter interaction and lasing mechanism.

Normally, light can interact with matter based on the following three processes, absorption, spontaneous emission, and stimulated emission in the gain medium as shown in Figure 1-7. To induce laser action, the number of molecules at higher excited-states (N_2) should be larger than those at lower ground-states (N_1), i.e., the formation of the population inversion. In the thermal equilibrium condition, based on the Maxwell-Boltzmann statistics, N_2 is usually smaller than N_1. Thus, we need intense excitation to induce population inversion. The population inversion

is hard to realize in a two energy-level system due to decreasing pumping efficiency. Hence, three-level and four-level systems are requisite to obtain population inversion. In ideal case, only a few molecules are required to be excited into the upper laser level to form a population inversion in four-level system [61].

Thus, a prerequisite for inducing lasing is the formation of a four-level system. When light travels through an amplifying medium, its intensity grows exponentially according to eq. 1-2:

$$I = I_0 \exp\left[(g(\lambda) - \alpha)l\right], \qquad \text{(eq. 1-2)}$$

where I_0 is the initial intensity, $g(\lambda)$ is the gain coefficient, α is the loss coefficient and l is the distance travelled in the gain medium. When the pump intensity is high enough for the gain to exceed the scattering losses ($g(\lambda) > \alpha$), then spontaneously emitted photons are exponentially amplified as they travel through the gain medium. After light amplification, the overall emission spectrum changes dramatically. A collapse of the emission spectrum (full width at half maximum, FWHM), called gain narrowing, is observed and this is called as amplified spontaneous emission (ASE). The measurement of ASE is an easy and simple method to characterize organic molecules as laser gain materials. The technique is to photo-pumping organic emitters in a slab waveguide, which can be made by vacuum-deposited or spin-coated a neat or doped thin film on a low-refractive-index substrate. The pumping energy when the optical gain surpasses the losses is defined as the ASE threshold E_{th}. Achieving a low ASE threshold system is one of the important goal to obtain a high performance lasing system and realize future OSLDs [73].

The threshold E_{th} is given by eq. 1-3 [74, 75]:

$$E_{th} = C' \frac{1}{\Gamma n_{eff} \Phi_{PL}} \left(\int \frac{\sigma_a}{\lambda} d\lambda \right)^{-2}, \qquad \text{(eq. 1-3)}$$

where C' is a constant, Γ is the confinement factor, n_{eff} is the effective refractive index in an

emission region, Φ_{PL} is the PLQY, σ_a is the steady-state absorption cross-section, and λ is the wavelength. Here, the Φ_{PL} can be given by eq. 1-4:

$$\Phi_{PL} = k_r \times \tau_r = \frac{k_r}{k_r + k_{nr}}, \quad \text{(eq. 1-4)}$$

where k_r, τ_r and k_{nr} are the radiative decay constant, fluorescence emission life time and nonradiative decay constant, respectively. Here, if eq. 1-5 satisfies:

$$\left(\int \frac{\sigma_a}{\lambda} d\lambda \right) = \text{constant}, \quad \text{(eq. 1-5)}$$

E_{th} is inversely proportional to k_r as eq. 1-6:

$$E_{th} \propto 1 + \frac{k_{nr}}{k_r}. \quad \text{(eq. 1-6)}$$

To reduce E_{th}, we would expect a higher k_r. Here, k_r is proportional to Einstein's B coefficient as eq. 1-7 [76]:

$$B \propto \left(c^3 / 8\pi h \nu^3 \right) k_r, \quad \text{(eq. 1-7)}$$

where h is Planck's constant, ν is the frequency of light, and c is the velocity of light. To get a higher k_r, larger Einstein's B coefficient is needed. Here, Einstein's B coefficient is also proportional to oscillator strength f which can be given by eq. 1-8 [77]:

$$B = \sqrt[\nu]{fc\sigma_a / h\nu}, \quad \text{(eq. 1-8)}$$

where the magnitude of the oscillator strength f for an electronic transition is proportional to the square of transition dipole moments (TDM) $\boldsymbol{\mu}$ produced by the action of electromagnetic radiation on a classical electric dipole as show in eq. 1-9 [78, 79]:

$$f \propto \vec{\mu}^2 = (e\vec{r})^2, \quad \text{(eq. 1-9)}$$

where e is elementary charge, and $\boldsymbol{r}$ is the extent of charge displacement (dipole length) of the positive and negative centers of the charge with the polarization of the transition. From these

eqs., the basic design rule for a suitable low threshold gain material should be based on a large TDM. Comparing with the classical electrical dipole theory, the quantum description of TDM between an initial state *m* and a final state *n* can be described by eq. 1-10:

$$\left|\vec{\mu}_{m,n}\right|^2 = \left\langle \psi_m \left| (\vec{er}) \right| \psi_n \right\rangle, \qquad \text{(eq. 1-10)}$$

where ψ_m and ψ_n are the wave functions of the electronic state *m* and *n*, respectively, which are responsible for the TDM. Hence, there are two major contributions to improve the value of TDM. One is the symmetries of initial state and final state should be different to allow the efficient transitions [80], and the other is the significant spatial overlap throughout the molecule between the initial and final state. For organic luminescent materials, especially for organic rigid planar system, spatial overlap of wave functions from different states like highest occupied molecular orbital (HOMO) and lowest unoccupied molecular orbital (LUMO) at an electronic excited-state appears to be sufficient to realize an intense electronic transition if the symmetries of the HOMO and LUMO wave functions are different. However, for most of charge transfer (CT) TADF molecules based on a molecular platform of D and A combined structure, such as D-A, D-π linker-A, D-A-D, and D-σ-A [81], the wave functions of HOMO and LUMO are separated. Thus, the molecular design for organic lasers based on TADF has been limited because of a twisted conformation or a non-conjugated bridge between the intra-/intermolecular D-A system. However, two new types of TADF molecules with an effective HOMO-LUMO overlap based on multiple resonance effect and non-adiabatic coupling effect have been reported with low ASE threshold [46, 82]. I will discuss more about the non-adiabatic coupling effect in Chapter 3.

1-3-2. Basic of resonator

ASE in waveguide structures is sometimes called mirrorless lasing as it has many similar properties of a real laser such as a distinct threshold in the input-output characteristics and the emission of a concentrated, polarized, and nearly monochromatic beam. Nonetheless, the absence of resonant modes and the incoherent output distinguishes ASE from lasing. Compared with the lasing, the FWHM in ASE is rather broader than that in lasing.

During pumping, absorption, spontaneous emission, and stimulated emission occur simultaneously. To create conditions where stimulated emission becomes predominant over spontaneous emission, an optical cavity or resonator is needed to reflect the beam back and forth through the amplifying medium as shown in Figure 1-7. In this situation, the coherent light satisfying the cavity condition can survive in the system, and the other light escapes the cavity from different directions. The positive feedback induced by the resonator is one of the basic elements of any laser systems.

Here, I introduced the most frequently used resonators geometries for OSSLs as shown in Figure 1-8. In the case of planar cavities, one mirror has a high reflectivity at the laser emission spectra range and the other has a partial transmission which functions as an output beam. However, due to the low round trip gain associated with the short gain length, the laser threshold of these devices is relatively high [61]. For working with whispering galleries and single crystals related lasers, multiple lithographic processing steps and special care have to be taken when interpreting results [83, 84]. To overcome these issues and achieve low threshold, long gain length during the round trip is needed. The efficiency of waveguide lasers can be further improved by diffractive structures, which do not rely on mirrors, but on periodic, wavelength scale corrugations that diffract the light in the spectral regions of optical gain. The lasing wavelength also can be tuned by changing the period of the grating. There have been

many different diffractive structures explored for OSSLs, including one-, two- and three-dimensional DFB structures, two- and three-dimensional photonic crystal structures, and concentric circular gratings that provide a radial feedback about a particular point, etc. [61, 83, 84]. To date, DFB structures have been proven to be the most effective and successful one for OSSLs [85-87].

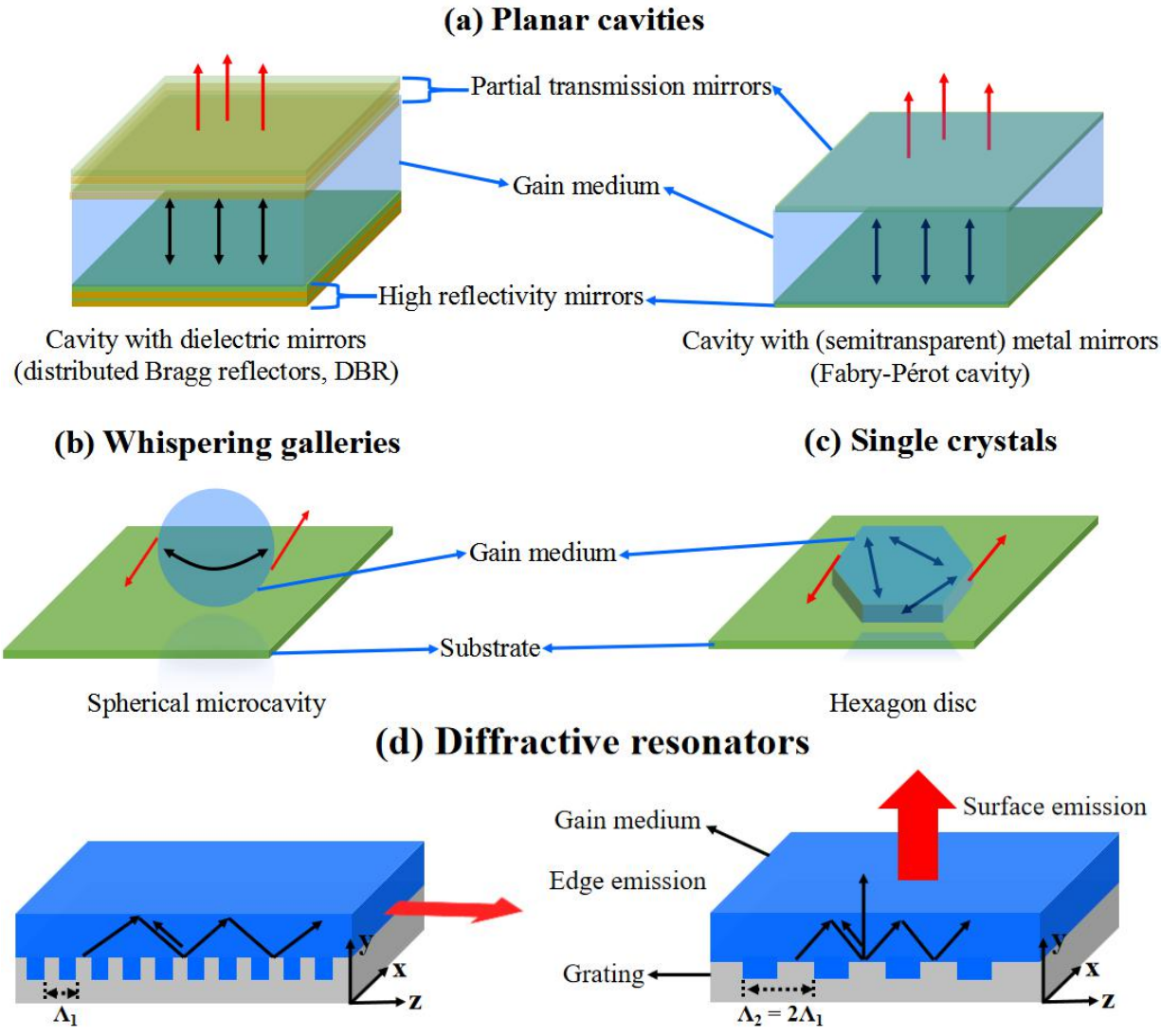

Figure 1-8. Schematic resonators used for OSSLs, modified from Refs. [83, 84]. The black arrows show feedback of the resonators, and the red arrows show the outcoupling of devices. (Λ is the period of the grating)

In DFB structures, the laser wavelength is given by the Bragg condition using eq. 1-11:

$$\lambda = 2n_{\text{eff}}\Lambda / n, \qquad \text{(eq. 1-11)}$$

where the Λ is the period of the grating, n_{eff} is the effective refractive index of the waveguide, n is the order of diffraction process. When n = 1, it is called first-order DFB, providing low threshold laser operation [88]. However, it always suffers from poor laser beam quality because of the edge emission. In case of organic thin film devices, it is difficult to fabricate a sharp edge due to their very thin films. The second-order DFB (n = 2) can provide an efficient and practical way to emit light normal to the surface. However, the threshold of second-order DFB normally is higher than that of first-order DFB [89]. To overcome this and combine the advantages of the first-order and the second-order DFB lasers, a mixed-order DFB laser which has not only the lower threshold but also efficient surface emission has been proposed [72, 90, 91]. The first-order regions provide strong feedback and the second-order regions placed in-between the first-order regions provide perpendicular outcoupling to the waveguide region. Figure 1-9 shows the mixed-order DFB structure I used in Chapter 4.

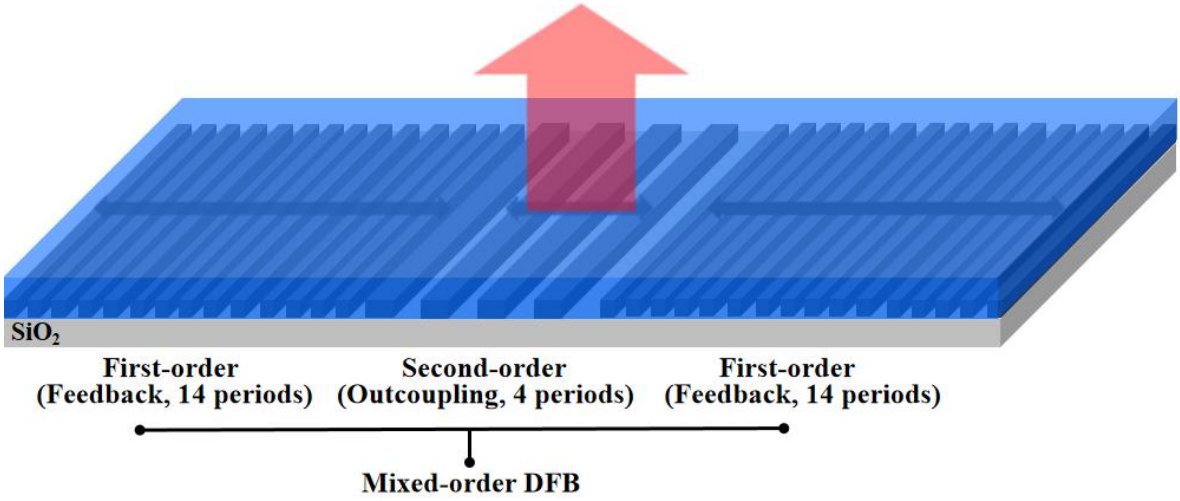

Figure 1-9. Schematic representation of the mixed-order DFB used in Chapter 4. (Blue part means the gain medium, the black arrows show feedback of the resonators, and the red arrows show the outcoupling of devices)

1-3-3. Exciton processes in organic lasers

Due to the low dielectric constant of organic semiconductors, the interaction between charge carriers (radical cations and anions) and the surrounding molecules is much stronger than that in inorganic compounds. Charge carriers induce a lattice distortion within their surrounding area. Hence, the interaction of charge carriers with molecular vibrations is stronger than in inorganic semiconductors. Therefore, the properties of charge carriers in organic semiconductors in combination with lattice distortions are usually described as a quasi-particle, which is referred to as polaron. Due to relaxation of the molecule, the polaronic states are within the energy-gap between the HOMO and LUMO levels. For OSSLs, these polaronic states induce additional absorption bands. Polaron induced absorption is assumed to be an important loss mechanism and a major obstacle towards the realization of the OSLDs.

Excitons are the state of neutral excited-states in molecules, and they have ability to diffuse from one molecule to another and hence comply with the definition of an exciton being a mobile excitation quasi-particle [36]. In organic semiconductors, the ASE and laser emission are generated in the S_1 states which are referred to as singlet excitons. However, the singlets can deactivate to the long-lived triplet excited-state T_1 through the ISC process. In most cases, the T_1 relaxes to the ground-state S_0 with a nonradiative decay, leading to the loss mechanism. Simultaneously, the molecule in the T_1 state can also be promoted to the higher-lying triplet excited-state T_n named as triplet absorption by a spin-allowed transition and this is also a deactivation process for lasing.

For intermolecular processes, bimolecular exciton annihilation processes also occur, inducing singlet-triplet annihilation (STA), triplet-triplet annihilation (TTA), and singlet-singlet annihilation (SSA).

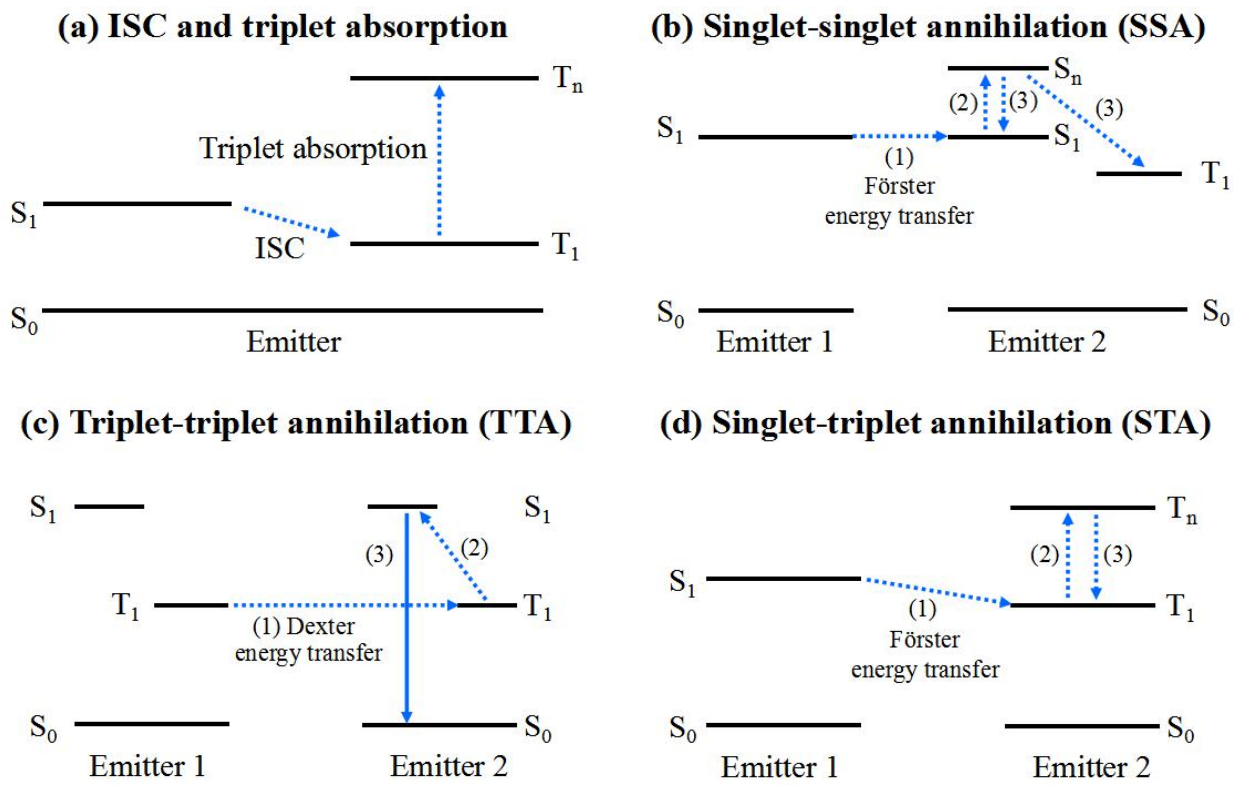

Figure 1-10. Exciton annihilation processes in organic semiconductors. (ISC: intersystem crossing, the dash arrow shows nonradiative decay, the solid arrow shows radiative decay, and (1)(2)(3) mean the annihilation processes according to priority)

An SSA is a process happening between two singlet excitons. During this phenomenon, the energy from one of the excited molecules is transferred to the second one. As a result, the first molecule falls back to its ground state and the second molecule gets promoted to a higher singlet excited-state S_n, then relax to S_1 with a probability 0.25 or to the T_1 with a probability 0.75 [92], which is exactly in the same proportions as when two polarons (one hole and one electron) encounter to make an exciton under electrical excitation.

A TTA is a process happening between two triplet excitons. The process is similar to the SSA, but can be considered as a positive quenching phenomenon, as it helps depleting the triplet population and creating singlets out of triplets. Because triplet state to singlet state transition is spin-forbidden for fluorescent materials, TTA can be explained by Dexter

exchange interaction [93].

An STA process quenches the singlet excitons by triplet excitons strongly. In this process, the energy of a singlet exciton is transferred to a triplet exciton, which is excited to a higher lying triplet excited-state. Subsequently, the excited triplet exciton quickly relaxes by intercombination to the first triplet excited-state. Overall, due to the harmful processes of triplet absorption and STA, triplet excitons accumulated should be removed in OSSLs. The exciton annihilation processes are summarized in Figure 1-10.

1-3-4. Continuous-wave lasing

True CW operation is a tough topic for the development of OSLDs because of the long-lived states of triplets can hinder lasing in the CW regime by quenching singlets.

In order to analysis CW condition for OSSLs, Forget et al. [61, 94] proposed eq. 1-12 for the triplet state as:

$$T_1^{ss} = k_{ISC}\tau_T S_1^{ss}, \quad \text{(eq. 1-12)}$$

where T_1^{ss} and S_1^{ss} are the steady-state population of the T_1 and S_1 state, respectively. k_{ISC} is the intersystem crossing rate and τ_T is the triplet lifetime. In order to have a rough estimate, they only consider triplet absorption as the loss, and neglect the STA or other losses. Under this condition, CW lasing will then be possible whenever triplet absorption probability will be lower than stimulated emission probability as eq. 1-13:

$$\sigma_{TT} T_1^{ss} < \sigma_{em} S_1^{ss}, \quad \text{(eq. 1-13)}$$

or eq. 1-14:

$$k_{ISC}\tau_T < \sigma_{em} / \sigma_{TT}, \quad \text{(eq. 1-14)}$$

where σ_{em} and σ_{TT} are the emission cross-section and triplet absorption cross-section, respectively. Normally, for the organic materials, the order of magnitude of σ_{em} and σ_{TT} are almost same, then the condition should be at least $k_{ISC} \times \tau_T < 1$. However, k_{ISC} is in the order of 10^7 s^{-1} for most organic luminescent materials, which means the triplet lifetime should be shorter than 100 ns to realize the true CW lasing. Thus, this condition is quite difficult to satisfy.

Based on above eqs., a good organic luminescent material for CW lasing should have at least a low k_{ISC} and a small τ_T to minimize the triplet population. In other words, the triplet absorption spectrum should be shifted as much as possible away from the emission spectrum of lasing. However, true CW lasing and OSLDs have not been realized because of the various

losses, mainly the triplet accumulation. Different ways have been developed to scavenge triplets like using the triplet quenchers [95, 96], but the generated triplet excitons still remain unused. To take full advantage of the triplet exctions, the TADF molecules may be a useful alternative based on their efficient RISC process. During the past six years, while triplet converting TADF molecules have been widely developed, the development of lower k_{ISC} and higher reverse intersystem crossing rate (k_{RISC}) is still unsolved problems [97, 98]. However, two promising TADF molecules have been shown low ASE threshold 1.6 ± 0.3 μJ/cm^2 at 494 nm and 6.7 μJ/cm^2 at 747 nm, respectively [46, 82]. To overcome the triplet accumulation and combine the advantages of the OSSLs and TADF molecules, triplet harvest TADF molecules should be promising for the realization of the true CW OSSLs and OSLDs.

1-4. Motivation and outline of this thesis

Organic luminescent materials have been identified as a suitable candidate for OLEDs and lasing. By taking account of various molecular structures, a wide variety of organic single crystals, small molecules, and polymers have been examined for this purpose. However, deep-red and NIR organic luminescent materials for high efficient OLEDs and low ASE and lasing threshold are still limited as shown in Figure 1-11 with molecular structures in Figure 1-12, and threshold with ASE and lasing peak are summarized in Table 1-2 [81-91, 99-113].

Although there are some reports on deep-red and NIR ASE or lasing, the thresholds are rather high, making them very difficult to be applied in CW OSSLs. The reason should come from the energy-gap law and ACQ, as I introduced before, decreasing the PLQY in these low energy-gap materials. However, the deep-red and NIR lasing materials are expected to play an important role not only in the same application fields of OLEDs, but also widely used in eye-tracking in virtual reality and augmented reality displays [114] and advanced driver assistance system [115] due to their color purity and identical in phase and direction.

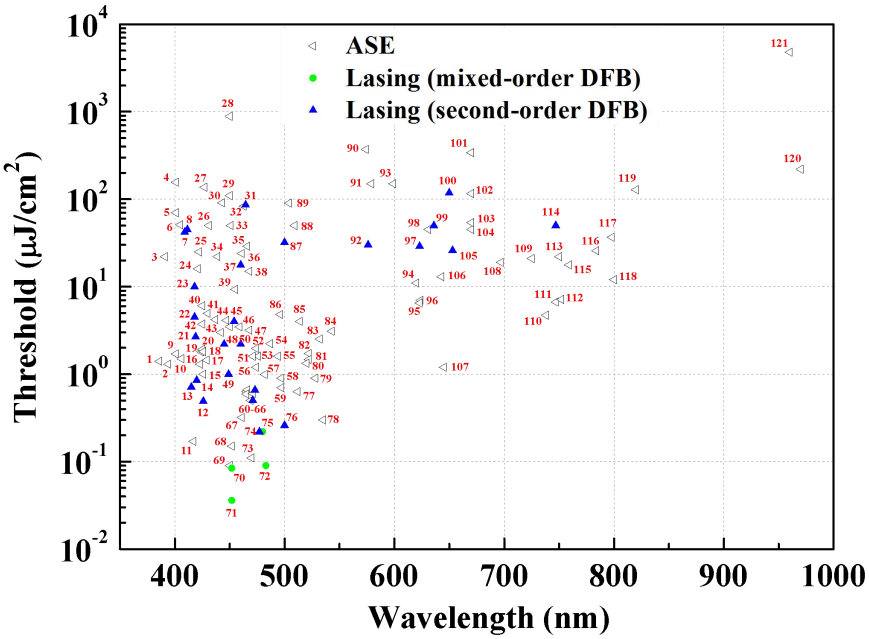

Figure 1-11. State-of-the-art of organic luminescent materials for ASE and lasing [46, 75, 81-91, 99-113].

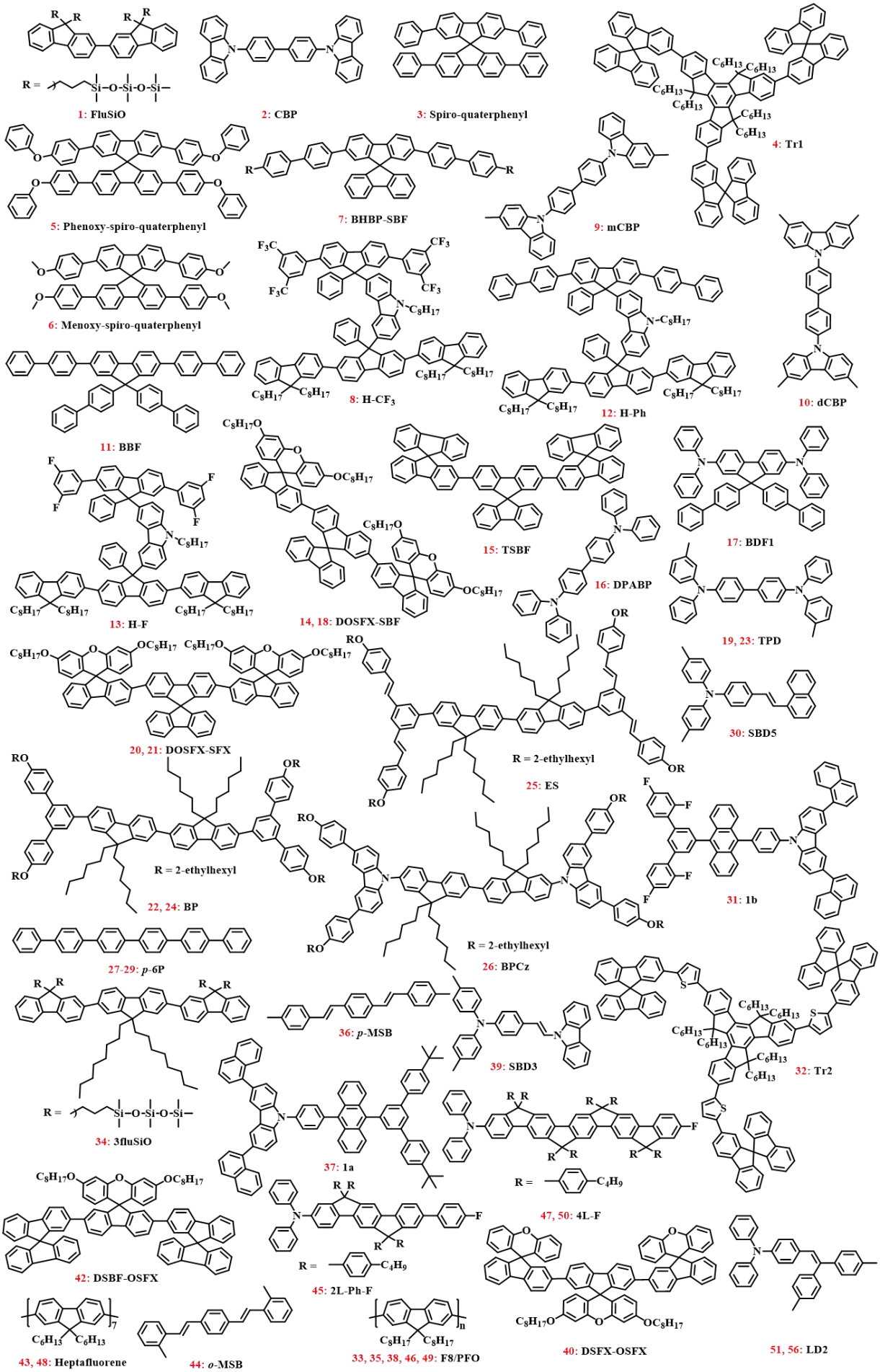
1: FluSiO
2: CBP
3: Spiro-quaterphenyl
4: Tr1
5: Phenoxy-spiro-quaterphenyl
6: Menoxy-spiro-quaterphenyl
7: BHBP-SBF
8: H-CF3
9: mCBP
10: dCBP
11: BBF
12: H-Ph
13: H-F
14, 18: DOSFX-SBF
15: TSBF
16: DPABP
17: BDF1
19, 23: TPD
20, 21: DOSFX-SFX
22, 24: BP
25: ES
R = 2-ethylhexyl
26: BPCz
27-29: p-6P
30: SBD5
31: 1b
32: Tr2
34: 3fluSiO
36: p-MSB
37: 1a
39: SBD3
40: DSFX-OSFX
42: DSBF-OSFX
43, 48: Heptafluorene
44: o-MSB
45: 2L-Ph-F
47, 50: 4L-F
51, 56: LD2
33, 35, 38, 46, 49: F8/PFO

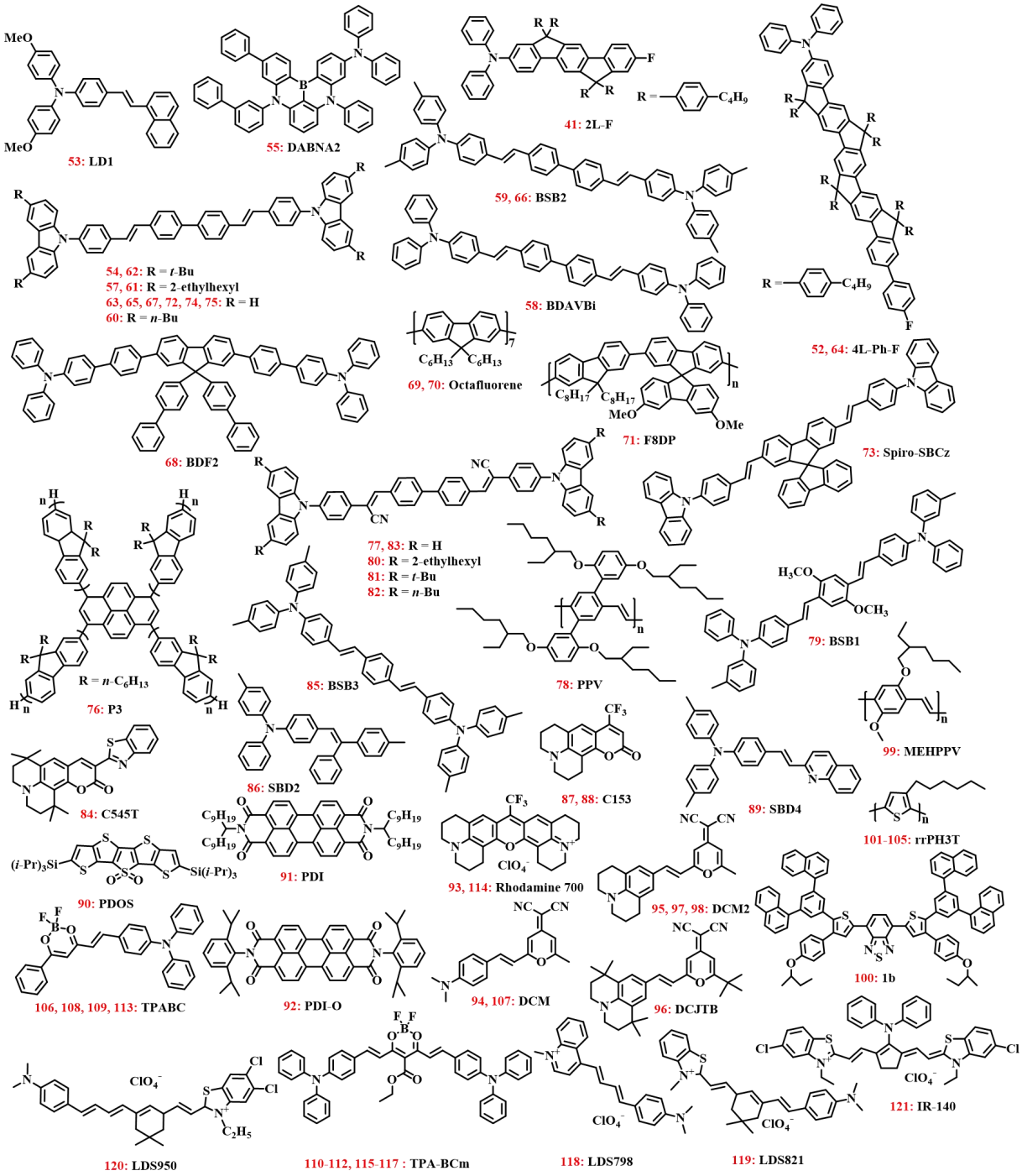

Figure 1-12. Structures of molecules 1-121 [46, 75, 81-91, 99-113].

Table 1-2. Summary of the threshold and ASE/lasing peak in molecules 1-121 [46, 75, 81-91, 99-113].

	1	**2**	**3**	**4**	**5**	**6**	**7**	**8**	**9**	**10**	**11**	**12**	**13**	**14**
Peak (nm)	386	394	391	401	401	405	409	412	401	406	417	426	415	420
Threshold ($\mu J/cm^2$)	1.4	1.3	22	156	70	51	42	45	1.7	1.5	0.17	0.49	0.71	0.85
	15	**16**	**17**	**18**	**19**	**20**	**21**	**22**	**23**	**24**	**25**	**26**	**27**	**28**
Peak (nm)	426	423	429	426	424	425	419	418	418	421	422	431	427	450
Threshold ($\mu J/cm^2$)	1	1.3	1.45	1.81	1.8	1.92	2.67	4.5	10	16	25	50	137	885
	29	**30**	**31**	**32**	**33**	**34**	**35**	**36**	**37**	**38**	**39**	**40**	**41**	**42**
Peak (nm)	450	443	465	463	451	439	466	461	460	468	455	425	430	425
Threshold ($\mu J/cm^2$)	110	91	86.1	83	50	22	29	24	17.7	15	9.3	6.06	4.95	3.72
	43	**44**	**45**	**46**	**47**	**48**	**49**	**50**	**51**	**52**	**53**	**54**	**55**	**56**
Peak (nm)	442	437	447	454	468	445	449	460	471	474	476	487	494	474
Threshold ($\mu J/cm^2$)	3	4.2	4.12	4	3.18	2.2	1	2.2	1.6	1.97	1.6	2.23	1.6	1.2
	57	**58**	**59**	**60**	**61**	**62**	**63**	**64**	**65**	**66**	**67**	**68**	**69**	**70**
Peak (nm)	482	497	497	465	465	466	473	471	471	469	461	452	450	452
Threshold ($\mu J/cm^2$)	0.99	0.9	0.7	0.63	0.59	0.66	0.66	0.5	0.6	0.5	0.32	0.15	0.09	0.08
	71	**72**	**73**	**74**	**75**	**76**	**77**	**78**	**79**	**80**	**81**	**82**	**83**	**84**
Peak (nm)	452	483	470	477	480	500	512	535	528	520	522	522	532	543
Threshold ($\mu J/cm^2$)	0.04	0.09	0.11	0.22	0.22	0.26	0.63	0.3	0.9	1.33	1.47	1.72	2.52	3.1
	85	**86**	**87**	**88**	**89**	**90**	**91**	**92**	**93**	**94**	**95**	**96**	**97**	**98**
Peak (nm)	514	496	500	509	504	574	579	576	599	620	623	624	623	631
Threshold ($\mu J/cm^2$)	4	4.8	32	50	90	370	150	30	150	11	6.5	7	29	45
	99	**100**	**101**	**102**	**103**	**104**	**105**	**106**	**107**	**108**	**109**	**110**	**111**	**112**
Peak (nm)	636	650	670	670	670	670	653	643	645	697	725	738	747	752
Threshold ($\mu J/cm^2$)	50	118	340	116	54	45	26	13	1.2	19	21	4.7	6.67	7.14
	113	**114**	**115**	**116**	**117**	**118**	**119**	**120**	**121**					
Peak (nm)	750	747	759	784	798	800	820	970	960					
Threshold ($\mu J/cm^2$)	22	50	17.7	25.8	36.7	12	128	220	4800					

Based on the expected new market in future, there is an intense interest to develop new organic deep-red and NIR molecules for OLEDs with high external quantum efficiency and CW OSSLs with low threshold. Therefore, this thesis focuses on molecular design for highly efficient deep-red and NIR organic luminescent materials. The outline of this thesis is as follows. In Chapter 2, I reported the ASE performance from a new deep-red molecule based on squaraine derivatives with the threshold as low as about 10 $\mu J/cm^2$ at 687 nm. By doping squaraine derivative into the host material, efficient FRET and suppressed ACQ were realized at low doping concentration. In Chapter 3, I examined two different boron-dipyrromethene materials and found the excellent performance of NIR ASE emission and thermally-activated delayed fluorescence. The dimeric borondifluoride curcuminoid derivative achieved the maximum external quantum efficiency value of 5.1% at a maximum emission wavelength of 758 nm. In addition, ASE with a maximum emission wavelength can be tuned between 801 and 860 nm, and a threshold as low as 7.5 $\mu J/cm^2$ was observed, providing additional evidence that borondifluoride curcuminoid derivatives are promising candidates for NIR OSSLs. Based on the results in Chapters 2 and 3, I demonstrated true CW lasing using the boron-dipyrromethene materials in Chapter 4. By harvesting the triplets from the TADF molecule, the clear demonstration of lasing under optical pumping with photo-excitation duration as long as 100 s was achieved. In Chapter 5, I summarized this thesis, providing the future prospect and the possible way to realize the final goal, the development of ideal NIR organic luminescent materials aiming for highly efficient OLEDs and current driven CW OSLDs.

1-5. References

[1] M. Pope and H. P. Kallmann, *J. Chem. Phys*., **1963**, 38, 2042.

[2] J. Dresner, *RCA Rev.*, **1969**, 30, 322.

[3] W. G. Williams, P. L. Spong, and D. J. Gibbons, *J. Phys. Chem. Solids*, **1972**, 33, 1879.

[4] W. Helfrich and W. G. Schneide, *Phys. Rev. Lett.*, **1965**, 14, 229.

[5] D. F. Williams and M. Schadt, *J. Chem. Phys.*, **1970**, 53, 3480.

[6] W. Helfrich and W. G. Schneider, *J. Chem. Phys.*, **1966**, 44, 2902.

[7] M. Sano, M. Pope, and H. Kallmann, *J. Chem. Phys.*, **1965**, 43, 2920.

[8] T. C. Werner, J. Chang, and D. M. Hercules, *J. Am. Chem. Soc.*, **1970**, 92, 763.

[9] H. P. Schwob, D. Weitz, and D. F. Williams, *Mol. Cryst. Liq. Cryst.*, **1973**, 24, 271.

[10] J. Kalinowski, J. Godlewski, and R. Signerski, *Mol. Cryst. Liq. Cryst.*,**1976**, 33, 247.

[11] J. Glinski, J. Godlewski, and J. Kalinowski, *Mol. Cryst. Liq. Cryst.*, **1978**, 48, 1.

[12] J. Kalinowski and J. Godlewski, *Chem. Phys. Lett.*, **1975**, 36, 345.

[13] N. E. Geacintov, M. Binder, C. E. Swenberg, and M. Pope, *Phys. Rev. B*, **1975**, 12, 4113.

[14] F. Lohmann and W. Mehl, *J. Chem. Phys.*, **1969**, 50, 500.

[15] W. Hwang and K. C. Kao, *J. Chem. Phys.*, **1974**, 60, 3845.

[16] L. L. T. Bradley, H. P. Schwob, D. Weitz, and D. F. D. Williams, *Mol. Cryst. Liq. Cryst.*, **1973**, 23, 271.

[17] P. S. Vincett, W. A. Barlow, F. T. Boyle, J. A. Finney, and G. G. Roberts, *Thin Solid Films*, **1979**, 60, 265.

[18] G. G. Roberts, T. M. McGmmty, W. A. Barlow, and P. S. Vincett, *Thin Solid Films*, **1980**, 68, 223.

[19] A. R. Elsharkawi and K. C. Kao, *J. Phys. Chem. Solids*, **1977**, 38, 95.

[20] P. S. Vincett and W. A. Barlow, *Thin Solid Films*, **1980**, 71, 305.

[21] P. S. Vincett, W. A. Barlow, R. A. Hann, and G. G. Roberts, *Thin Solid Films*, **1982**, 94, 171.

[22] S. Hayashi, H, Etoh, and S. Saito, *Jpn. J. Appl. Phys.*, **1986**, 25, 773.

[23] C. W. Tang and S. A. VanSlyke, *Appl. Phys. Lett.*, **1987**, 51, 913.

[24] C. Adachi, S. Tokito, T. Tsutsui, and S. Saito, *Jpn. J. Appl. Phys.*, **1988**, 27, 269.

[25] C. Adachi, S. Tokito, T. Tsutsui, and S. Saito, *Jpn. J. Appl. Phys.*, **1988**, 27, 713.

[26] C. W. Tang, S. A. VanSlyke, and C. H. Chen, *J. Appl. Phys.*, **1989**, 65, 3610.

[27] M. A. Baldo, D. F. O'Brien, M. E. Thompson, and S. R. Forrest, *Phys. Rev. B*, **1999**, 60, 14422.

[28] M. A. Baldo, D. F. O'Brien, Y. You, A. Shoustikov, S. Sibley, M. E. Thompson, and S. R. Forrest, *Nature*, **1998**, 395, 151.

[29] C. Adachi, M. A. Baldo, M. E. Thompson, and S. R. Forrest, *J. Appl. Phys.*, **2001**, 10, 5048.

[30] A. Endo, M. Ogasawara, A. Takahashi, D. Yokoyama, Y. Kato, and C. Adachi, *Adv. Mater.*, **2009**, 21, 4802.

[31] H. Uoyama, K. Goushi, K. Shizu, H. Nomura, and C. Adachi, *Nature*, **2012**, 492, 234.

[32] J. H. Burroughes, D. D. C. Bradley, A. R. Brown, R. N. Marks, K. Mackay, R. H. Friend, P. L. Burns, and A. B. Holmes, *Nature*, **1990**, 347, 539.

[33] http://apps.webofknowledge.com/WOS_GeneralSearch_input.do?product=WOS&search_mode=GeneralSearch&SID=E4yUmPueKxzxIIyjMyX&preferencesSaved=

[34] https://www.extremetech.com/extreme/193402-what-is-night-vision-how-does-it-work-and-do-i-really-need-it-in-my-next-car

[35] A. Zampetti, A. Minotto, B. M. Squeo, V. G. Gregoriou, S. Allard, U. Scherf, C. L. Chochos, and F. Cacialli, *Sci. Rep.*, **2017**, 7, 1611.

[36] W. P. Fan, P. Huang, and X. Y. Chen, *Chem. Soc. Rev.*, **2016**, 45, 6488.

[37] Y. Khan, D. G. Han, A. Pierre, J. Ting, X. C. Wang, C. M. Lochner, G. Bovo, N. Yaacobi-Gross, C. Newsome, R. Wilson, and A. C. Arias, *Proc. Natl. Acad. Sci. USA*, **2018**, 115, E11015.

[38] http://blogs.nature.com/onyourwavelength/2018/05/14/near-infrared-a-fact-sheet/

[39] J. V. Caspar, E. M. Kober, B. P. Sullivan, and T. J. Meyer, *J. Am. Chem. Soc.*, **1982**, 104, 630.

[40] S. W. Thomas III, G. D. Joly, and T. M. Swager, *Chem. Rev.*, **2007**, 107, 1339.

[41] C. Borek, K. Hanson, P. I. Djurovich, M. E. Thompson, K. Aznavour, R. Bau, Y. R. Sun, S. R. Forrest, J. Brooks, L. Michalski, and J. Brown, *Angew. Chem. Int. Ed.*, **2007**, 46, 1109.

[42] K. T. Ly, R. W, Chen-Cheng, H. W. Lin, Y. J. Shiau, S. H. Liu, P. T. Chou, C. S. Tsao, Y. C. Huang, and Y. Chi, *Nat. Photon.*, **2017**, 11, 63.

[43] K. R. Graham, Y. X. Yang, J. R. Sommer, A. H. Shelton, K. S. Schanze, J. G. Xue, and J. R. Reynolds, *Chem. Mater.*, **2011**, 23, 5305.

[44] M. Cocchi, D. Virgili, V. Fattori, J. A. G. Williams, and J. Kalinowski, *Appl. Phys. Lett.*, **2007**, 90, 023506.

[45] L. Huang, C. D. Park, T. Fleetham, and J. Li, *Appl. Phys. Lett.*, **2016**, 109, 233302.

[46] D. H. Kim, A. D'Aléo, X. K. Chen, A. S. D. Sandanayaka, D. D. Yao, L. Zhao, T. Komino, E. Zaborova, G. Canard, Y. Tsuchiya, E. Y. Choi, J. W. Wu, F. Fages, J. L. Brédas, J. C. Ribierre, and C. Adachi, *Nat. Photon.*, **2018**, 12, 98.

[47] Y. Yuan, Y. Hu, Y. X. Zhang, J. D. Lin, Y. K. Wang, Z. Q. Jiang, L. S. Liao, and S. T. Lee, *Adv. Funct. Mater.*, **2017**, 27, 1700986.

[48] A. Minotto, P. Murto, Z. Genene, A. Zampetti, G. Carnicella, W. Mammo, M. R. Andersson, E. G. Wang, and F. Cacialli, *Adv. Mater.*, **2018**, 30, 1706584.

[49] P. Data, P. Pander, M. Okazaki, Y. Takeda, S. Minakata, and A. P. Monkman, *Angew. Chem. Int. Ed.*, **2016**, 55, 5739.

[50] L. Yao, S. T. Zhang, R. Wang, W. J. Li, F. Z. Shen, B. Yang, and Y. G. Ma, *Angew. Chem. Int. Ed.*, **2014**, 126, 2151.

[51] T. X. Liu, L. P. Zhu, C. Zhong, G. H. Xie, S. L. Gong, J. F. Fang, D. G. Ma, and C. L. Yang, *Adv. Funct. Mater.*, **2017**, 27, 1606384.

[52] A. Obolda, X. Ai, M. Zhang, and F. Li, *ACS Appl. Mater. Interfaces*, **2016**, 8, 35472.

[53] S. P. Wang, X. J. Yan, Z. Cheng, H. Y. Zhang, Y. Liu, and Y. Wang, *Angew. Chem. Int. Ed.*, **2015**, 54, 13068.

[54] P. Murto, A. Minotto, A. Zampetti, X. F. Xu, M. R. Andersson, F. Cacialli, and E. G. Wang, *Adv. Opt. Mater.*, **2016**, 4, 2068.

[55] C. L. Li, R. H. Duan, B. Y. Liang, G. C. Han, S. P. Wang, K. Q. Ye, Y. Liu, Y. P. Yi, and Y. Wang, *Angew. Chem. Int. Ed.*, **2017**, 56, 11525.

[56] X. B. Du, J. Qi, Z. Q. Zhang, D. G. Ma, and Z. Y. Wang, *Chem. Mater.*, **2012**, 24, 2178.

[57] G. Qian, Z. Zhong, M. Luo, D. B. Yu, Z. Q. Zhang, Z. Y. Wang, and D. G. Ma, *Adv. Mater.*, **2009**, 21, 111.

[58] Y. Hu, Y. Yuan, Y. L. Shi, J. D. Lin, Z. Q. Jiang, and L. S. Liao, *J. Mater. Chem. C*, **2018**, 6, 1407.

[59] P. P. Sorokin and R. Lankard, *IBM J. Res. Develop.*, **1966**, 10, 162.

[60] F. P. Schafer, W. Schmidt, and J. Volze, *Appl. Phys. Lett.*, **1966**, 9, 306.

[61] S. Forget and S. Chénais, *Organic Solid-State Lasers*. Springer-Verlag: Berlin Heidelberg, 2013.

[62] O. G. Peterson, S. A. Tuccio, and B. B. Snavely, *Appl. Phys. Lett.*, **1970**, 17, 245.

[63] R. L. Fork, B. I. Greene, and C. V. Shank, *Appl. Phys. Lett.*, **1981**, 38, 671.

[64] E. P. Ippen, C. V. Shank, and A. Dienes, *Appl. Phys. Lett.*, **1972**, 21, 348.

[65] D. Strickland and G. Mourou, *Opt. Commun.*, **1985**, 56, 219.

[66] https://www.nobelprize.org/prizes/physics/2018/press-release/

[67] B. H. Soffer and B. B. McFarland, *Appl. Phys. Lett.*, **1967**, 10, 266.

[68] F. Hide, B. J. Shwartz, M. A. Díaz-García, and A. J. Heeger, *Chem. Phys. Lett.*, **1996**, 256, 424.

[69] N. Tessler, G. J. Denton, and R. H. Friend, *Nature*, **1996**, 382, 695.

[70] T. Rabe, K. Gerlach, T. Riedl, H. H. Johannes, W. Kowalsky, J. Niederhofer, W. Gries, J. Wang, T. Weimann, P. Hinze, F. Galbrecht, and U. Scherf, *Appl. Phys. Lett.*, **2006**, 89, 081115.

[71] Y. Yang, G. A. Turnbull, and I. D. W. Samuel, *Appl. Phys. Lett.*, **2008**, 92, 163306.

[72] A. S. D. Sandanayaka, T. Matsushima, F. Bencheikh, K. Yoshida, M. Inoue, T. Fujihara, K. Goushi, J. C. Ribierre, and C. Adachi, *Sci. Adv.*, **2017**, 3, e1602570.

[73] Y. Setoguchi and C. Adachi, *J. Appl. Phys.*, **2010**, 108, 064516.

[74] T. Komino, H. Nomura, M. Yahiro, K. Endo, and C. Adachi, *J. Phys. Chem. C*, **2011**, 115, 19890.

[75] M. Inoue, T. Matsushima, and C. Adachi, *Appl. Phys. Lett.*, **2016**, 108, 133302.

[76] T. Aimono, Y. Kawamura, K. Goushi, H. Yamamoto, H. Sasabe, and C. Adachi, *Appl. Phys. Lett.*, **2005**, 86, 071110.

[77] R. C. Hilborn, *Am. J. Phys.*, **1982**, 50, 982.

[78] K. Kirby and D. L. Cooper, *J. Chem. Phys.*, **1989**, 90, 4895.

[79] E. N. Lassettre, A. Skerbele, and M. A. Dillon, *J. Chem. Phys.*, **1969**, 50, 1829.

[80] R. Obaid and M. Leibscher, *J. Chem. Phys.*, **2015**, 142, 064315.

[81] J. H. Kim, J. H. Yun, and J. Y. Lee, *Adv. Opt. Mater.*, **2018**, 6, 1800255.

[82] H. Nakanotani, T. Furukawa, T. Hosokai, T. Hatakeyama, and C. Adachi, *Adv. Opt.*

Mater., **2017**, 5, 1700051.

[83] I. D. W. Samuel and G. A. Turnbull, *Chem. Rev*., **2007**, 107, 1272.

[84] A. J. C. Kuehne and M. C. Gather, *Chem. Rev*., **2016**, 116, 12823.

[85] M. Hirade, H. Nakanotani, R. Hattori, A. Ikeda, M. Yahiro, and C. Adachi, *Mol. Cryst. Liq. Cryst.*, **2009**, 504, 1.

[86] J. H. Kim, M. Inoue, L. Zhao, T. Komino, S. M. Seo, J. C. Ribierre, and C. Adachi, *Appl. Phys. Lett.*, **2015**, 106, 053302.

[87] A. S. D. Sandanayaka, K. Yoshida, M. Inoue, C. J. Qin, K. Goushi, J. C. Ribierre, T. Matsushima, and C. Adachi, *Adv. Opt. Mater.*, **2016**, 4, 834.

[88] C. Karnutsch, C. Gärtner, V. Haug, U. Lemmer, T. Farrell, B. S. Nehls, U. Scherf, J. Wang, T. Weimann, G. Heliotis, C. Pflumm, J. C. deMello, and D. D. C. Bradley, *Appl. Phys. Lett.*, **2006**, 89, 201108.

[89] R. D. Xia, W. Y. Lai, P. A. Levermore, W. Huang, and D. D. C. Bradley, *Adv. Funct. Mater.*, **2009**, 19, 2844.

[90] C. Karnutsch, C. Pflumm, G. Heliotis, J. C. deMello, D. D. C. Bradley, J. Wang, T. Weimann, V. Haug, C. Gärtner, and U. Lemmer, *Appl. Phys. Lett.*, **2007**, 90, 131104.

[91] D. H. Kim, A. S. D. Sandanayaka, L. Zhao, D. Pitrat, J. C. Mulatier, T. Matsushima, C. Andraud, J. C. Ribierre, and C. Adachi, *Appl. Phys. Lett.*, **2017**, 110, 023303.

[92] C. Gärtner, *Organic Laser Diodes: Modelling and Simulation*, Universitätsverlag Karlsruhe, Karlsruhe, 2009.

[93] A. Kohler and H. Bassler, *Mater. Sci. Eng. R Rep.*, **2009**, 66, 71.

[94] S. Chénais and S. Forget, *Polym. Int.*, **2012**, 61, 390.

[95] Y. F. Zhang and S. R. Forrest, *Phys. Rev. B*, **2011**, 84, 241301.

[96] L. Zhao, M. Inoue, K. Yoshida, A. S. D. Sandanayaka, J. H. Kim, J. C. Ribierre, and C.

Adachi, *IEEE Quantum Electron.*, **2016**, 22, 1300209.

[97] H. Noda, H. Nakanotani, and C. Adachi, *Sci. Adv.*, **2018**, 4, eaao6910.

[98] X. Cai, X. Li, G. Xie, Z. He, K. Gao, K. Liu, D. Chen, Y. Cao, and S. J. Su, *Chem. Sci.*, **2016**, 7, 4264.

[99] K. Yamashita, T. Kuro, K. Oe, and H. Yanagi, *Appl. Phys. Lett.*, **2006**, 88, 241110.

[100] J. Thompson, M. Anni, S. Lattante, D. Pisignano, R. I. R. Blyth, G. Gigli, and R. Cingolani, *Synth. Met.*, **2004**, 143, 305.

[101] M. Fang, J. Huang, S. J. Chang, Y. Jiang, W. Y. Lai, and W. Huang, *J. Mater. Chem. C*, **2017**, 5, 5797.

[102] Y. Okumura, M. Nagawa, C. Adachi, M. Satsuki, S. Suga, T. Koyama, and Y. Taniguchi, *Chem. Lett.*, **2000**, 29, 754.

[103] T. Aimono, Y. Kawamura, K. Goushi, H. Yamamoto, H. Sasabe, and C. Adachi, *Appl. Phys. Lett.*, **2005**, 86, 071110.

[104] Y. Kawamura, H. Yamamoto, K. Goushi, H. Sasabe, and C. Adachi, *Appl. Phys. Lett.*, **2004**, 84, 2724.

[105] H. Nakanotani, S. Akiyama, D. Ohnishi, M. Moriwake, M. Yahiro, T. Yoshihara, S. Tobita, and C. Adachi, *Adv. Funct. Mater.*, **2007**, 17, 2328.

[106] R. Kabe, H. Nakanotani, T. Sakanoue, M. Yahiro, and C. Adachi, *Adv. Mater.*, **2009**, 21, 4034.

[107] M. Anni and S. Lattante, *J. Phys. Chem. C*, **2015**, 119, 21620.

[108] S. Yuyama, T. Nakajima, K. Yamashita, and K. Oe, *Appl. Phys. Lett.*, **2008**, 93, 033062.

[109] A. Maity, A. Sarkar, A. Sil, S. B. N. Bhaktha, and S. K. Patra, *New J. Chem.*, **2017**, 41, 2296.

[110] M. Mamada, T. Fukunaga, F. Bencheikh, A. S. D. Sandanayaka, and C. Adachi, *Adv.*

Funct. Mater., **2018**, 1802130.

[111] Y. Qian, Q. Wei, G. Del Pozo, M. M. Mroz, L. Lueer, S. Casado, J. Cabanillas-Gonzalez, Q. Zhang, L. H. Xie, R. D. Xia, and W. Huang, *Adv. Mater.*, **2014**, 26, 2937.

[112] Z. Y. Zuo, C. J. Ou, Y. J. Ding, H. Zhang, S. X. Sun, L. H. Xie, R. D. Xia, and W. Huang, *J. Mater. Chem. C,* **2018**, 6, 4501.

[113] J. Huang, Q. Liu, J. H. Zou, X. H. Zhu, A. Y. Li, J. W. Li, S. Wu, J. B. Peng, Y. Cao, R. D. Xia, D. D. C. Bradley, and J. Roncali, *Adv. Funct. Mater.*, **2009**, 19, 2978.

[114] https://patents.justia.com/patent/9869847

[115] https://www.extremetech.com/extreme/193402-what-is-night-vision-how-does-it-work-and-do-i-really-need-it-in-my-next-car

Chapter 2

Deep-red amplified spontaneous emission from *cis*-configured squaraine

2-1. Introduction

OSLDs have been received intense attention since the first demonstration of optically pulse pumped OSSLs in 1996 [1], because of their applications in flexible and low-cost devices as data communication, chemical sensing, and spectroscopic tools. Numerous organic molecules emitting at visible wavelengths with high optical gain and low lasing threshold have been developed, especially for blue-emitting materials [2-5]. However, molecules showing deep-red and NIR ASE and lasing are still very rare. The dyes, 4-(dicyanomethylene)-2-methyl-6-julolidyl-9-enyl-4*H*-pyran (DCM2) [6] and perylene diimide (PDI) [7], have been reported to show deep-red and NIR ASE and lasing. The reason for the lack of such molecules is that nonradiative decay from excited-states increases exponentially as energy gaps' decreasing, namely, the energy-gap law as I introduced in Chapter 1. Squaraine (SQ) derivatives are known to display intense, narrow, and sharp absorption with extremely high molar extinction coefficients on the order of 10^5 M^{-1} cm^{-1} and narrow photoluminescence (PL) peaks because of their rigid molecular backbones as well as emitting deep-red to NIR emission. SQs typically have a D-A-D CT structure or an asymmetrical D-π linker-A structure. Because of their simple synthetic routes and good stability in the ambient environment, SQ derivatives have been used for a wide variety of applications, for example, dye-sensitized solar cells, field effect transistors, photovoltaic cells, and OLEDs [8-15]. However, SQs displaying ASE and lasing properties have not yet been reported.

SQ derivatives frequently suffer from serious aggregation induced quenching in solid-state, which lowers their PLQYs. Doping technology has been widely used to suppress molecular aggregation and increase PLQYs. In guest-doped host films, PL occurs from guest molecules by virtue of energy transfer, like FRET between host and guest molecules. For FRET, a large overlap between the PL spectrum of host molecules and the absorption spectrum of guest

molecules is necessary. SQ derivatives generally exhibit no or weak absorption in the blue and green region, which makes it difficult to induce efficient FRET because few suitable host materials are available that can be effectively excited by the 337 nm pulsed N_2 gas laser used in this Chapter. To achieve the better spectral overlap and the sufficient light absorption, I chose 4,4'-bis(*N*-carbazolyl)-1,1'-biphenyl (CBP) as a host material for SQ derivatives.

In this Chapter, deep-red ASE from *cis*-configured SQ (*cis*-DCSQ1) doped into CBP film was demonstrated. *Cis*-DCSQ1 has strong push-pull indolenine-based dicyanovinyl acceptor substituents. By introduction of the dicyanovinyl group, the inversion center is inevitably destroyed and the increased steric demand of the additional acceptor groups forces the donor groups into a *cis*-like arrangement. Thus, by introduction of the D-A-D system, two indolenine ring and the dicyanovinyl unit are in plane with the central squarate ring to exhibit an almost planar π skeleton. This planarity allows *cis*-DCSQ1 has high dipole moment and efficient FRET from CBP to *cis*-DCSQ1 occurs in the doped film because of their large spectral overlap. Additionally, the ACQ is suppressed in the doped film. The improved FRET and suppressed PL quenching contribute to the demonstration of ASE from the SQ derivative.

2-2. Experimental

Starting materials and all the solvents were purchased from Wako Pure Chemical Industries, Ltd., Tokyo Chemical Industry Co., Ltd., and Sigma-Aldrich Co., Ltd., and used without further purification, unless otherwise stated. ^{1}H nuclear magnetic resonance (NMR) and ^{13}C NMR spectra were recorded in $CDCl_3$ by using an Avance III 500 spectrometer (Bruker Biospin) operating at 500 MHz for ^{1}H NMR and 125 MHz for ^{13}C NMR. Fused silica substrates were cleaned by sequential ultrasonication in detergent, pure water, acetone, and isopropanol. The SQ neat films and doped CBP films were deposited on the fused silica substrates by spin-coating from chloroform solutions in air. The absorption and steady-state PL spectra were measured using a UV-vis spectrophotometer (Lambda 950-PKA, PerkinElmer) and a spectrofluorometer (FP-6500, JASCO), respectively. The PLQYs of spin-coated films were measured using a xenon lamp and integrating sphere (C11347-11 Quantaurus QY, Hamamatsu Photonics). The transient PL decay characteristics of solution and film samples were recorded using a Quantaurus-Tau fluorescence lifetime measurement system (C11367-03, Hamamatsu Photonics). The solution concentration used for the above optical measurements was 10^{-5} M in dimethylformamide, chloroform, and dichloromethane (CH_2Cl_2). The excitation wavelength was 300 nm for the PL and PLQY measurements and 340 nm for the PL lifetime measurements.

To characterize their ASE properties, the samples were optically pumped by a pulsed nitrogen laser (KEN-2020, Usho) emitting 337-nm UV light. This laser delivered pulses with a duration of 700 ps at a repetition rate of 20 Hz. The pump beam intensities were varied using a set of neutral density filters. The pump beam was focused into a 0.4 × 0.1 cm area. The emission spectra from the edge of the films were collected using an optical fiber connected to a charge-coupled device spectrometer (PMA-11, Hamamatsu Photonics). The thickness of the films was approximately determined by a surface profilometer (Dektak 8, Veeco).

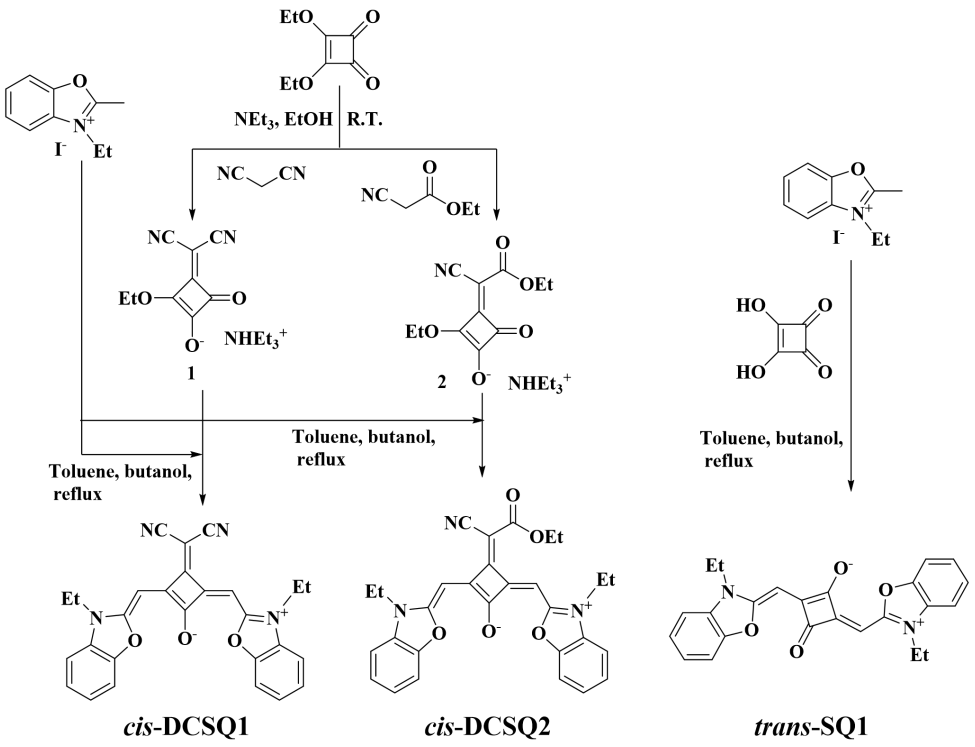

Scheme 2-1. Synthetic routes for *cis*-DCSQ1, *cis*-DCSQ2, and *trans*-SQ1.

Synthetic routes for *trans*-SQ1, *cis*-DCSQ1, and *cis*-DCSQ2 are schematically shown in Scheme 2-1. The compounds 1 and 2 and three SQ derivatives were synthesized using the same methods previously published [8].

For the synthesis of *cis*-DCSQ1 and *cis*-DCSQ2, a mixture of the compound 1 or 2 (1.00 mmol) and the corresponding donor molecules (2.00 mmol) were refluxed in 30 mL of a 1:1 mixture of toluene and *n*-butanol using a Dean-Stark trap for 14 h. After total conversion of the starting materials (monitored by TLC), the solvent was evaporated and the residue was subject to column chromatography (silica gel, CH_2Cl_2/MeOH 99:1) and subsequent precipitation from CH_2Cl_2/hexane to afford the pure product.

For the synthesis of *trans*-SQ1, a mixture of squaric acid (1.00 mmol) and the corresponding donor (2.00 mmol) were refluxed in 20 mL of a 1:1 mixture of *n*-butanol and toluene using a Dean-Stark trap for 18 h. After total conversion of the starting materials

(monitored by TLC), the solvent was evaporated and the residue was purified by column chromatography (silica gel, $CHCl_3$/MeOH 95:5), and subsequent precipitation from a $CHCl_3$/hexane to afford the pure product.

cis-DCSQ1: Yield: 75.3 mg (16.7%), violet solid; ^{1}H NMR (500 MHz, $CDCl_3$) δ (ppm): 7.60 (d, J = 7.8 Hz, 2H), 7.33 (dt, J = 7.7 Hz, 1.1 Hz, 2H), 7.28 (dt, J = 7.7 Hz, 1.3 Hz, 2H), 7.15 (d, J = 7.8 Hz, 2H), 5.80 (s, 2H), 4.07 (m, 4H), 1.49 (t, J = 7.4 Hz, 1.3 Hz, 6H); ^{13}C NMR (125 MHz, $CDCl_3$) δ (ppm): 182.3, 168.5, 160.1, 154.3, 147.6, 136.8, 130.9, 125.6, 124.7, 119.4, 111.8, 109.1, 72.4, 39.6, 12.8.

cis-DCSQ2: Yield: 204.2 mg (41.3%), violet solid; ^{1}H NMR (500 MHz, $CDCl_3$) δ (ppm): 7.58 (d, J = 7.8 Hz, 2H), 7.33-7.29 (dt, J = 7.65 Hz, 1.05 Hz, 2H), 7.12 (d, J = 7.65 Hz, 2H), 7.05 (s, 2H), 6.89 (s, 2H), 4.12-4.08 (m, 4H), 1.72-1.69 (t, J = 7.15 Hz, 2H), 1.50 (d, J = 5.9 Hz, 3H), 0.98-0.95 (t, J = 7.4 Hz, 6H); ^{13}C NMR (125 MHz, $CDCl_3$) δ (ppm): 183.4, 171.3, 165.2, 160.4, 151.3, 142.7, 134.9, 130.1, 126.2, 120.8, 114.2, 110.3, 75.3, 58.3, 39.6, 19.3, 14.3.

trans-SQ1: Yield: 50 mg (12.5%), blue solid; ^{1}H NMR (500 MHz, $CDCl_3$) δ (ppm): 7.54 (d, J = 7.6 Hz, 2H), 7.27 (d, J = 7.3 Hz, 2H), 7.21-7.18 (dd, J = 7.85 Hz, 3.2 Hz, 2H), 7.05 (d, J = 7.5 Hz, 2H), 5.35 (s, 2H), 4.03-3.99 (m, 4H), 1.43-1.40 (t, J = 7.25 Hz, 6H); ^{13}C NMR (125 MHz, $CDCl_3$) δ (ppm): 179.4, 177.3, 152.1, 141.8, 129.5, 125.0, 123.9, 111.6, 108.4, 79.3, 42.1, 12.7.

2-3. Results

2-3-1. Photoluminescent properties of *cis*-DCSQ1

Cis-DCSQ1 was highly soluble in homogeneous organic solvents such as chloroform, dichloromethane, and dimethylformamide. The molar extinction coefficient of *cis*-DCSQ1 was high: ~1.87×10^5 M^{-1} cm^{-1} for a chloroform solution with a concentration of 10^{-5} M. The PLQY of the solution was 82.5%. In addition, *cis*-DCSQ1 displayed marked negative solvatochromism. The main absorption peak for chloroform existed at 621 nm with the additional weak hypsochromic absorption band at 385 nm as shown in Figure 2-1(a). Density functional theory (DFT) calculations confirmed these qualitative structure-property relationships as shown in Figures 2-1(b) and (c). The calculated electron density distribution showed a distribution of the electron density over the whole π molecular system for the HOMO-1 and HOMO. In contrast to that, the LUMO exhibited the electron density concentrated along the cyanine-type polymethine bridge and neither the dicyanovinyl nor the oxygen acceptor showed a notable contribution. Together with the orbital energies of these frontier molecular orbitals, an assignment of the observed optical transition probability became possible [16]. Thus, the main S_0-S_1 absorption band related to a transition from the HOMO to the LUMO level with a large transition probability of 99.0% due to the excellent overlap of the HOMO and LUMO orbitals. The observed additional hypsochromic absorption band could be ascribed to higher energy transitions from the HOMO-1 to the LUMO level with transition probability of 96.4%. Compared with the spectra of the neat film, the single sharp absorption band in visible range of the spectra suggests the monomeric nature of *cis*-DCSQ1 in such diluted solutions. And owing to a pronounced excitonic coupling of these densely packed *cis*-DCSQ1, a substantial red shift and band broadening is observed in the neat film.

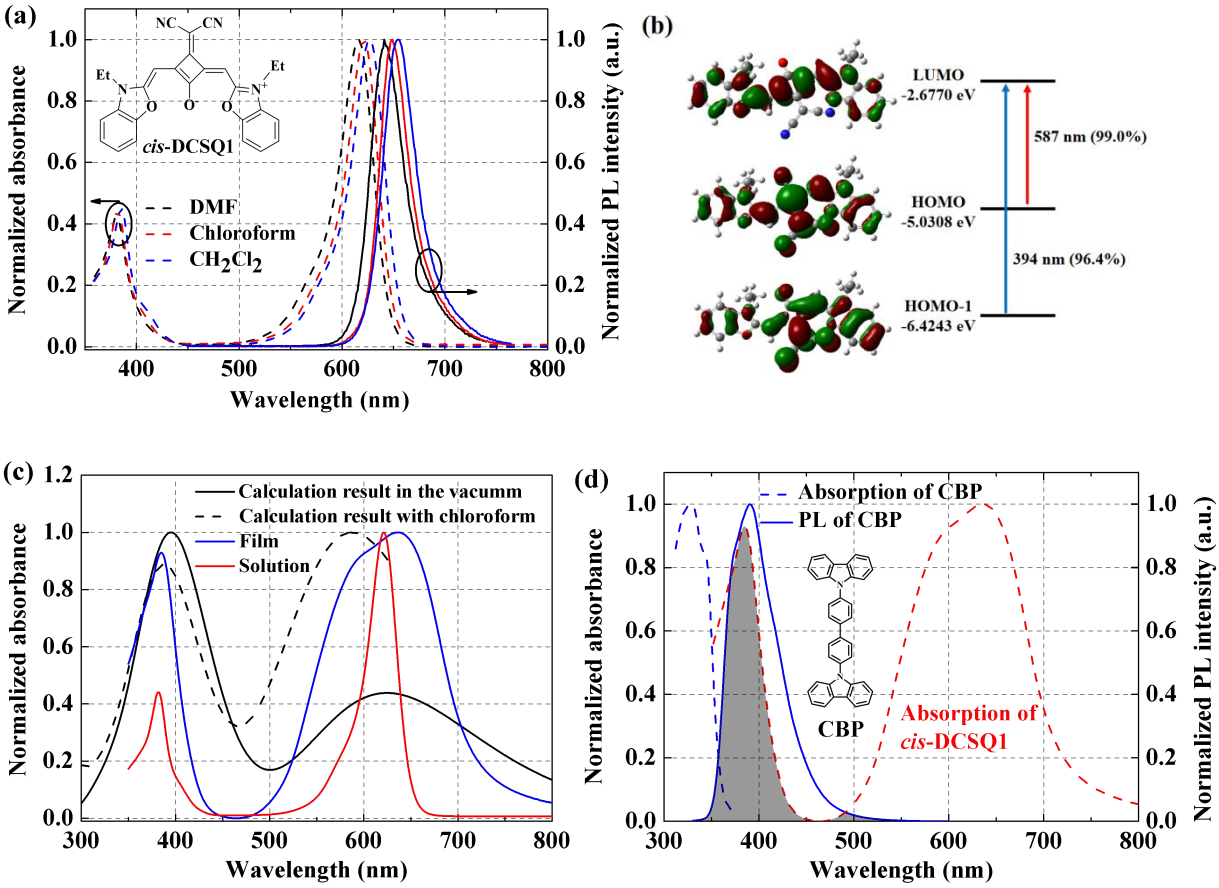

Figure 2-1. (a) Absorption and PL spectra of *cis*-DCSQ1 in a 1 × 10^{-5} M chloroform, dimethylformamide (DMF), and dichloromethane (CH_2Cl_2) solution. Inset is the chemical structure of *cis*-DCSQ1. (b) Spatial distributions of *cis*-DCSQ1 calculated by DFT at B3LYP/6-31+g(d) level with chloroform as the solvent using Gaussian 09 program package (Gaussian 09, revision A.02, M. J. Frisch et al., Gaussian, Inc., Wallingford CT, 2016). (c) Absorption of *cis*-DCSQ1 from calculation result, 1 × 10^{-5} M chloroform sample, and a neat film sample. (d) Absorption and PL spectra of a CBP neat film and the absorption spectrum of a *cis*-DCSQ1 neat film. Inset is the chemical structure of CBP. The gray shaded shows the overlap between the emission from a CBP neat film and the absorption from a *cis*-DCSQ1 neat film.

CBP films doped with different concentrations of *cis*-DCSQ1 were prepared by spin-coating procedure from chloroform solutions at identical conditions (2000 rpm for 30 s in air), and their optical properties were investigated at room temperature. The FRET efficiency depends significantly on the spectral overlap between the host emission and guest absorption.

Figure 2-1(d) reveals that the large spectral overlap between the PL spectrum of CBP and the weak hypsochromic absorption band of *cis*-DCSQ1 leads to FRET. This means that CBP is a suitable host for *cis*-DCSQ1. Another advantage of using CBP is the effective absorption of 337 nm pulsed excitation light from the N_2 laser used for ASE measurements [17, 18].

Figures 2-2(a) and (b) show the absorption and PL spectra, respectively, of doped films with the *cis*-DCSQ1 concentrations ranging from 0.01 to 10 wt%. When the *cis*-DCSQ1 concentration exceeded 5 wt%, the PL from both CBP and *cis*-DCSQ1 was very weak because of the strong ACQ. At the low doping concentration below 0.01 wt%, the doped films displayed strong blue PL originating from CBP because of inefficient FRET from CBP to *cis*-DCSQ1 as shown in Figure 2-2(b). The above observations are consistent with the photographs of the doped films under ultraviolet (UV) irradiation (365 nm) in Figure 2-2(c).

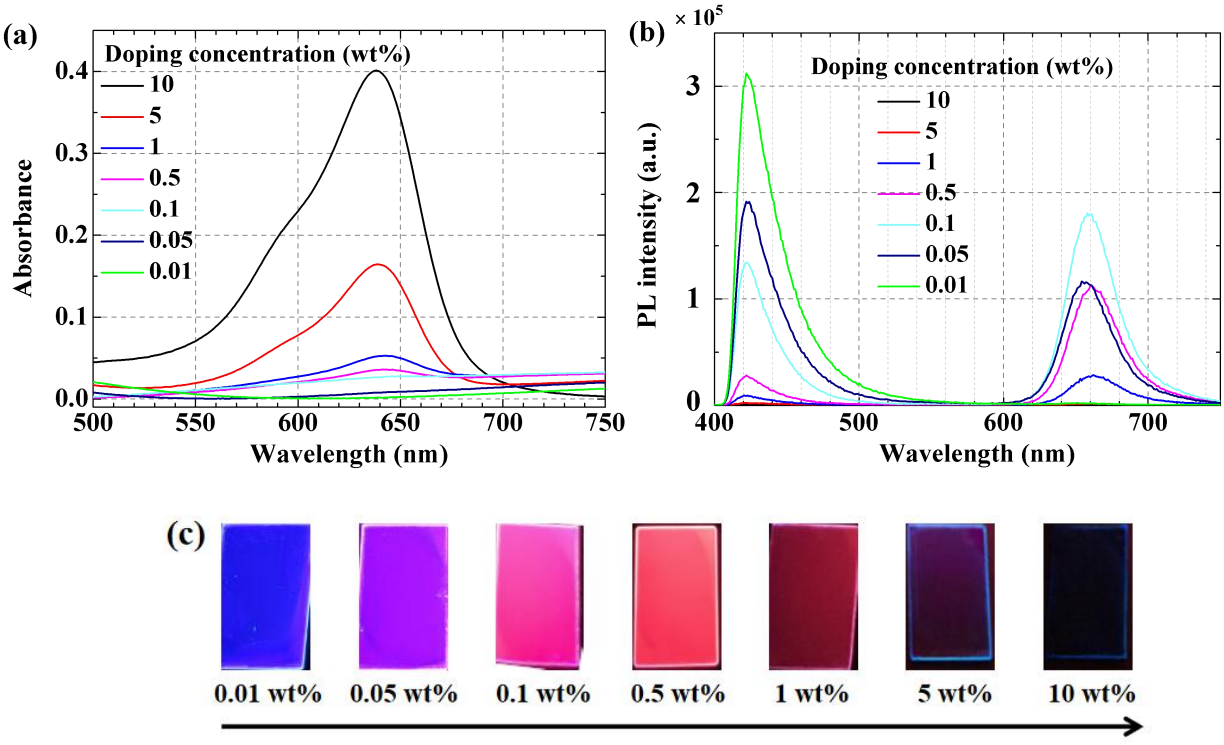

Figure 2-2. (a) Absorption (b) PL and (c) Photographs of doped films of *cis*-DCSQ1 in CBP with different doping concentrations. The photographs were taken under 365-nm UV light.

The FRET efficiency (E) from CBP to *cis*-DCSQ1 was estimated from Figure 2-2(b) by using the eq. 2-1 [19, 20]:

$$E = 1 - I_{HG}/I_{H}, \qquad \text{(eq. 2-1)}$$

where I_{HG} and I_{H} are the intensities of PL from CBP in *cis*-DCSQ1 doped film and CBP neat film, respectively. The calculated FRET efficiency is shown in Figure 2-3. The FRET efficiency rapidly increased from 2.8% to 95.5% as the doping concentrations were increased from 0.01 to 1 wt% and became almost constant at a doping concentration higher than 1 wt%.

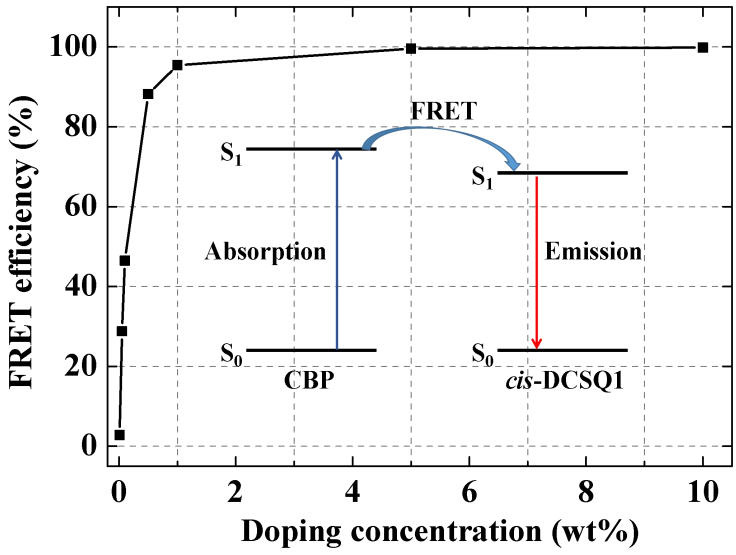

Figure 2-3. FRET efficiency of the doped films.

The concentration dependence of the optical parameters of the films is summarized in Table 2-1. The PLQYs dramatically decreased from 61.8% to 0.5% with increasing *cis*-DCSQ1 doping concentration from 0.1 to 10 wt%. This is because the ACQ became more dominant than the improved FRET at high *cis*-DCSQ1 concentration. All of the doped films exhibited single exponential fluorescence decays. The PL lifetimes estimated from the decays shortened at high *cis*-DCSQ1 concentrations. This is additional proof that ACQ occurs at high *cis*-DCSQ1 concentration.

Table 2-1. Summary of the absorption wavelength (λ_{abs}), maximum PL wavelength (λ_{PL}), PL lifetime (τ), PLQY (Φ_{PL}), and radiative decay constant (k_r) of *cis*-DCSQ1-doped CBP films and a *cis*-DCSQ1 solution in chloroform.

Doping concentration (wt%)	λ_{abs} **(nm)**	λ_{PL} **(nm)**	τ **(ns)**	Φ_{PL} **(%)**	k_r **(10^8 s^{-1})**
Solution	621	649	5.04	82.5	1.64
0.01	NA	NA	1.38[a]	43.6	3.38
0.05	NA	NA	5.55	53.5	0.96
0.1	NA	658	5.26	61.8	1.17
0.5	643	660	3.29	35.5	1.08
1	643	662	1.2	10.3	0.86
5	639	NA	0.39	0.7	0.18
10	638	NA	0.35	0.5	0.14

a: Calculated based on choosing 400 nm as the emission wavelength of the host CBP. NA: Not available.

2-3-2. Thickness effect on amplified spontaneous emission threshold in *cis*-DCSQ1

For the ASE measurement, I prepared a doped film by spin-coating onto a pre-cleaned fused silica substrate. The set-up for ASE experiments is shown in Figure 2-4(a). The controlling factors of ASE are based on the photophysical properties of materials, such as Φ_{PL}, τ, and k_r. Our group recently demonstrated that k_r is well correlated with the E_{th} [2]. A larger k_r leads to lower E_{th} because Einstein's B constant (stimulated emission coefficient) is proportional to k_r as shown in Chapter 1. The k_r values at 0.05 and 0.1 wt% *cis*-DCSQ1 are larger than those at 0.5 and 1 wt% as shown in Table 2-1, but ASE at these lower concentrations were difficult to be observed. The reason for which could be ascribed to the inefficient FRET as shown in Figure 2-3. Further, no ASE was observed when the doping concentration of *cis*-DCSQ1 higher than 1 wt%. This is because of a decrease of k_r caused by aggregation of *cis*-DCSQ1 at the higher concentrations.

When the irradiation intensity was low, the PL from the 0.5 wt% *cis*-DCSQ1-doped film with the thickness of 183 nm showed a peak wavelength of 670 nm as shown in Figure 2-4(b) and the shape showed no dependence on the irradiation intensity. However, a sharp peak appeared at 687 nm when the irradiation intensity exceeded a certain value, which can be assigned to ASE as shown in Figure 2-4(b). With increasing the irradiation power from 12 μJ/cm^2, the PL intensity began to amplify and the FWHM suddenly decreased from 60 nm (spontaneous emission) to 8 nm (ASE) as shown in Figure 2-4(c). This irradiation intensity (12 μJ/cm^2) corresponds to the ASE threshold. The ASE wavelength shifted to slightly shorter wavelength by about 5 nm as the irradiation intensity was increased from 48 to 117 μJ/cm^2. This wavelength shift would be caused by the vibration of the molecule due to heating the film under optical pumping [21]. Under the same conditions, the ASE threshold of a 1 wt% *cis*-DCSQ1-doped film was 32.3 μJ/cm^2, which is higher than that of the 0.5 wt% *cis*-DCSQ1-

doped film (12 μJ/cm^2). However, this is the first deep-red ASE observed from an SQ derivative.

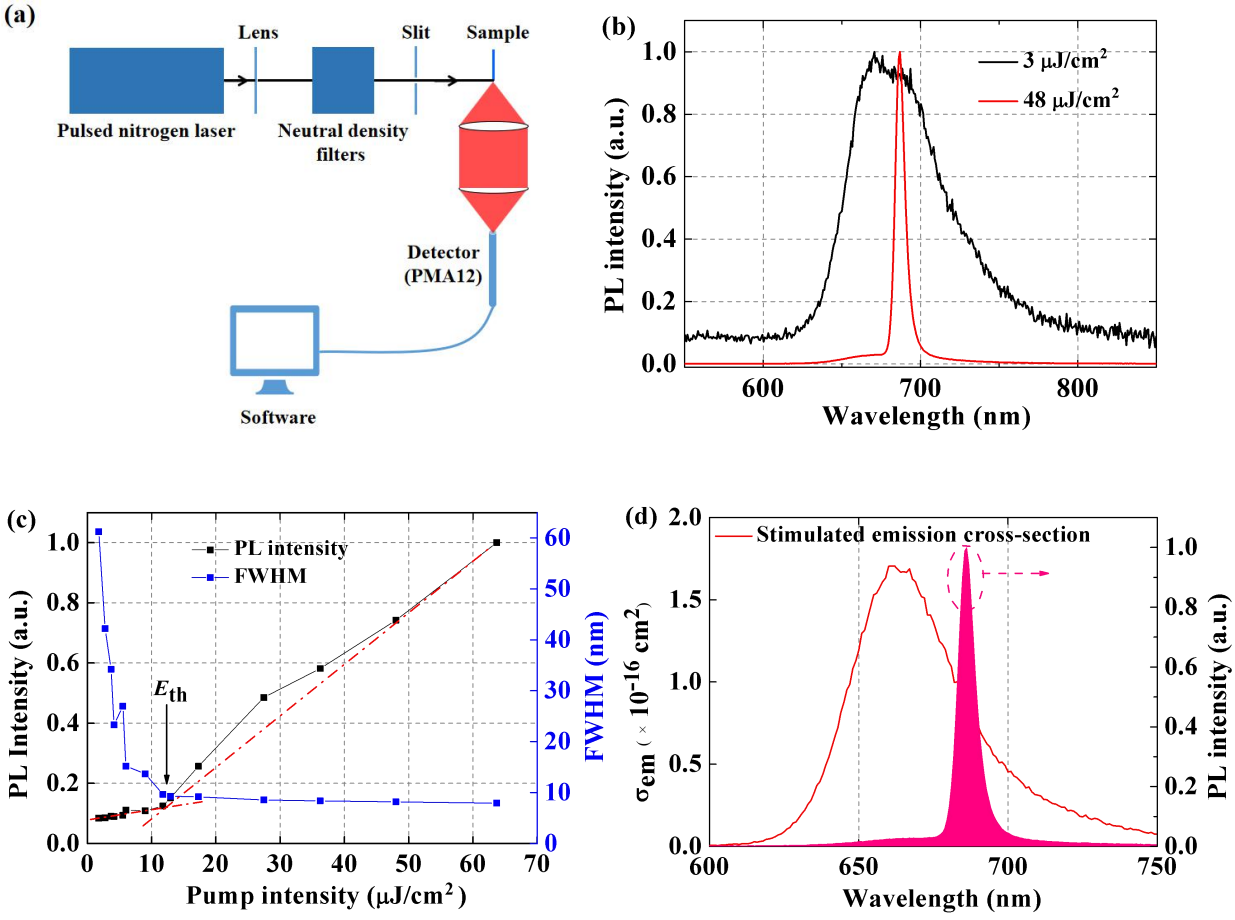

Figure 2-4. (a) Schematic representations of the ASE measurement. (b) PL spectra of a 0.5 wt% *cis*-DCSQ1 doped film collected from the sample edge at different excitation intensities below and above the ASE threshold. (c) Plots of PL intensity (black squares) and FWHM (blue squares) as a function of irradiation intensity for a 0.5 wt% *cis*-DCSQ1-doped CBP film with a thickness of 183 nm. (d) Stimulated emission cross-section and a representative ASE spectrum measured in 0.5 wt% *cis*-DCSQ1-doped CBP film.

To assess the optical gain in the 0.5 wt% *cis*-DCSQ1 doped film, I estimated the stimulated emission cross-section (σ_{em}), which is related to the Einstein *B* coefficient. σ_{em} is obtained by using eq. 2-2 [22]:

$$\sigma_{em}(\lambda) = \frac{\lambda^4 E_f(\lambda)}{8\pi n^2(\lambda) c \tau}, \qquad \text{(eq. 2-2)}$$

where $E_f(\lambda)$ corresponds to the distribution of the PL efficiency, $n(\lambda)$ is the dispersion of the refractive index, τ is the transient lifetime, and c is the vacuum light velocity. I estimated σ_{em} from a 0.5 wt% *cis*-DCSQ1 doped film. It can be seen that the σ_{em} is a high value of about 0.83 $\times$ 10^{-16} cm^2 at the ASE peak wavelength, providing evidence that the sample is expected to show ASE behavior as shown in Figure 2-4(d).

In order to optimize the ASE threshold, the different thicknesses of 0.5 wt% *cis*-DCSQ1 doped films in a range from 117 to 251 nm were prepared by controlling substrate rotation speeds during spin-coating. As shown in Figure 2-5(a), the lowest threshold was around 10 $\mu J/cm^2$ at the thickness of 175 nm. Similar thickness dependence of the ASE threshold has been reported in other organic materials [5]. This behavior can be ascribed to the interplay between the guided propagation mode confinement and the progressive variations of the spatial overlap between maximum electric field region and excited region when the thickness changed in the *cis*-DCSQ1 active waveguide [23, 24]. In order to model the modes in the asymmetric waveguide, the cutoff wavelength of waveguides with an isotropic core layer was calculated. For a given thickness of the *cis*-DCSQ1 blend layer in an asymmetric waveguide, the transverse electric (TE) and transverse magnetic (TM) modes have a distinct cutoff wavelength, above which no guided mode exists. If the wavelength of the propagating light is shorter than the cutoff wavelength, the light can propagate inside the waveguide without leakage. The cutoff wavelength for the ASE, λ_{TE} and λ_{TM}, depends on the refractive index of gain materials, surroundings glass, air, and the thickness of the guided light. λ_{TE} is expressed by the following equation that represents the TE mode of waveguiding [25]:

$$\lambda_{TE} = \frac{2\pi d\sqrt{n_m^2 - n_g^2}}{\arctan\left(\sqrt{\frac{n_g^2 - n_a^2}{n_m^2 - n_g^2}}\right) + m\pi}, \qquad \text{(eq. 2-3)}$$

and λ_{TM} [25],

$$\lambda_{TM} = \frac{2\pi d\sqrt{n_m^2 - n_g^2}}{\arctan\left(\frac{n_m^2}{n_a^2}\sqrt{\frac{n_g^2 - n_a^2}{n_m^2 - n_g^2}}\right) + m\pi}, \quad \text{(eq. 2-4)}$$

where n_m, n_g, n_a, d, and m are the refractive index of gain material, substrate (glass), cladding layer (air), thickness, and mode number, respectively. The films under this study constitute asymmetric planar waveguides since their refractive index is larger than that of the glass and the air. I find that for the thinnest films, the zero-order TE mode is the only mode guided in the film whereas for the thicker film, light can also be guided in the zero-order TM mode as shown in Figure 2-5(b). This data agreed well with other materials, which also for the thicker films, both TE and TM modes being allowed to guide at the emission wavelengths [26].

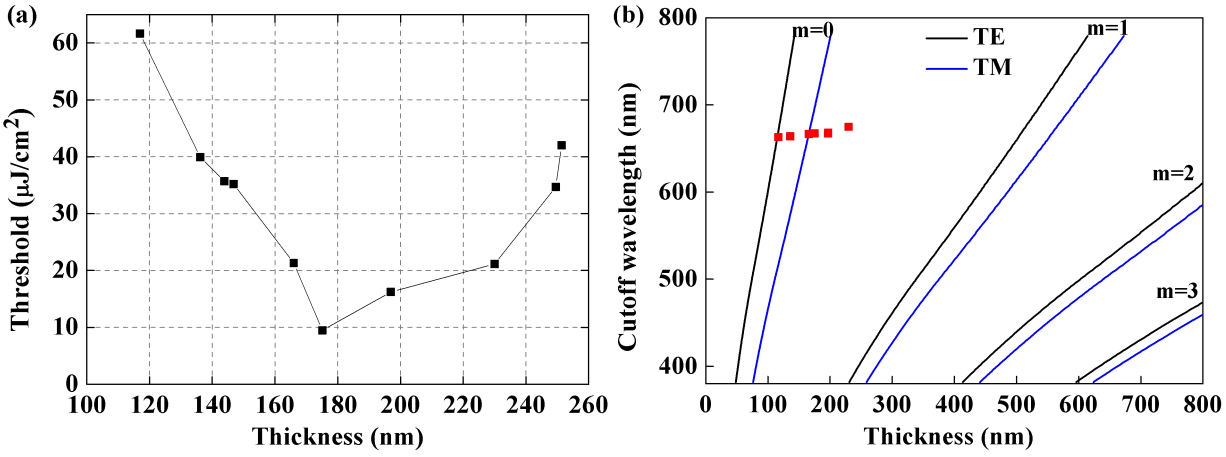

Figure 2-5. (a) Plot of ASE threshold as a function of doped film thickness at the *cis*-DCSQ1 concentration of 0.5 wt%. The excitation wavelength was 337 nm for all of the measurements. (b) Calculated cutoff wavelength of TE and TM modes propagating in slab waveguides (black and blue lines), and experimental values of peak wavelengths of edge emissions (red squares).

2-3-3. Stability of doped film under intense light irradiation

The photostability of a 0.5 wt% *cis*-DCSQ1 doped film with a thickness of 197 nm was investigated upon the excitation of 337 nm at the power of 16.5 μJ/cm^2 (close to the ASE threshold). The rapid degradation was observed as shown in Figure 2-6 both in air and N_2 condition. The experiments in N_2 rule out the possibility of degradation from oxygen and moisture. Although the emission property worsening during laser exposure is a common property of many organic active materials, a reason for the quick degradation observed here would be based on the photostablity against pumped excitation UV laser light, resulting in the irreversible loss of its ability to fluoresce.

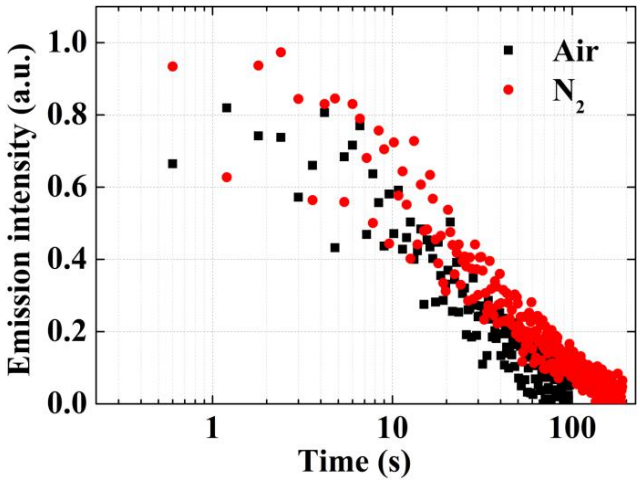

Figure 2-6. Measurement of photostability of a *cis*-DCSQ1 doped CBP film under laser irradiation at the power of 16.5 μJ/cm^2.

In order to understand the fast bleaching effect, the photochemical stability of the doped film under incoherent UV (365nm)-irradiation was examined too. The photochemical properties of the 0.5 wt% *cis*-DCSQ1 doped CBP blend film were studied by means of PL spectroscopy. The irradiation energy from the UV lamp is about 0.88 mW/cm^2. By increasing the irradiation time, the PL intensities dramatically decreased to 20% of the initial PL intensity, indicating the significant photo-decomposition within the first 20 minutes as shown in Figure 2-7(a). With the

longer time irradiation, the PL intensity from *cis*-DCSQ1 decreased further, while the emission from the host was almost same, indicating that the host is rather stable under UV-irradiation. It should be noted that a new peak around 550 nm was observed after the passage of 20 minutes, which could be originated from the decomposition of *cis*-DCSQ1. Furthermore, the exposure to the UV or laser light causes the gradual decrease of the emission band in the visible range which should be caused by the competitive process of the excited *cis*-DCSQ1 that leads to decomposition.

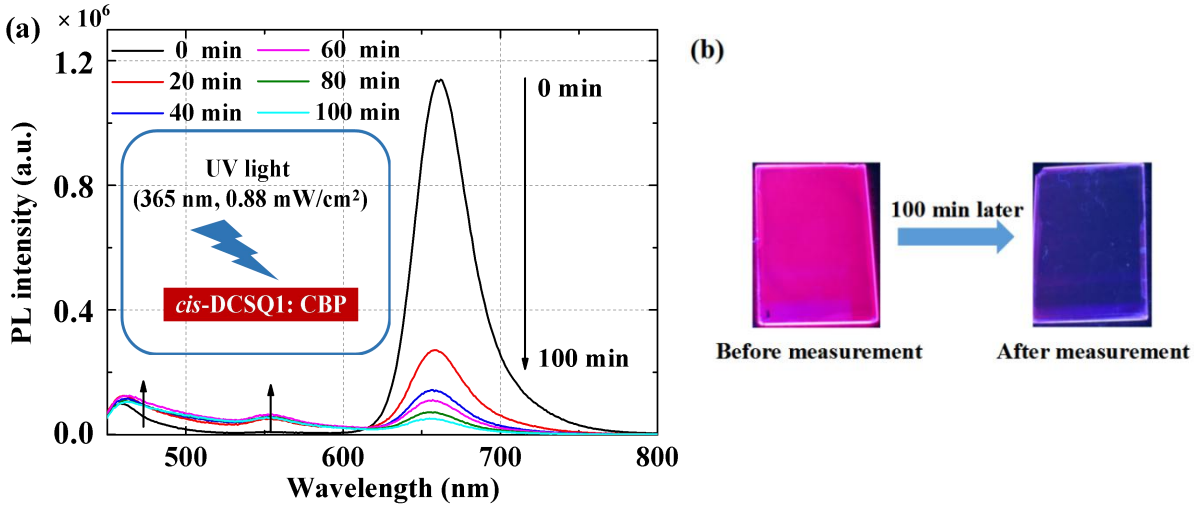

Figure 2-7. (a) The changes of PL spectra in a 0.5 wt% *cis*-DCSQ1 doped CBP blend film under 365 nm-UV irradiation. The arrows indicate the direction of change with the passage of the irradiation time. (b) Photographs of the 0.5 wt% *cis*-DCSQ1 doped CBP blend film under 365 nm-UV irradiation before and after 100 min irradiation.

In order to eliminate the formation of aggregates and the effect from host CBP, the diluted solutions have been used to study its photostability in different solvents. Here, chloroform and DMF were used because of different polarity and photoreactive with *cis*-DCSQ1 and its excited states for comparison. Solvent polarity strongly affects the charge transfer and the competing energy transfer, which are fundamental processes to check the stability. Here, chloroform is polar, and DMF is polar aprotic solvent. The very fast *cis*-DCSQ1 bleaching, seen as the

decrease of the intensity of the bands at 623 nm and 382 nm, was observed in the chloroform solution as shown Figure 2-8(a). Just after 10 min of exposure, these bands decreased. It clearly indicates the rapid photodegradation process of the dye caused by the radical products of the chloroform photolysis [27]. Simultaneously, the slight increase of the absorption in the range of 500-550 nm. Further, a slightly decrease of the intensity of the bands at 617 nm and 381 nm was also observed in the DMF solution as shown Figure 2-8(b), while a slight increase of the absorption occurred in the range of 400-470 nm, suggesting the formation of the new product. The photolysis process of squaraine dye in DMF can be caused by the direct interaction of the excited *cis*-DCSQ1 with solvent molecules undergoing decomposition.

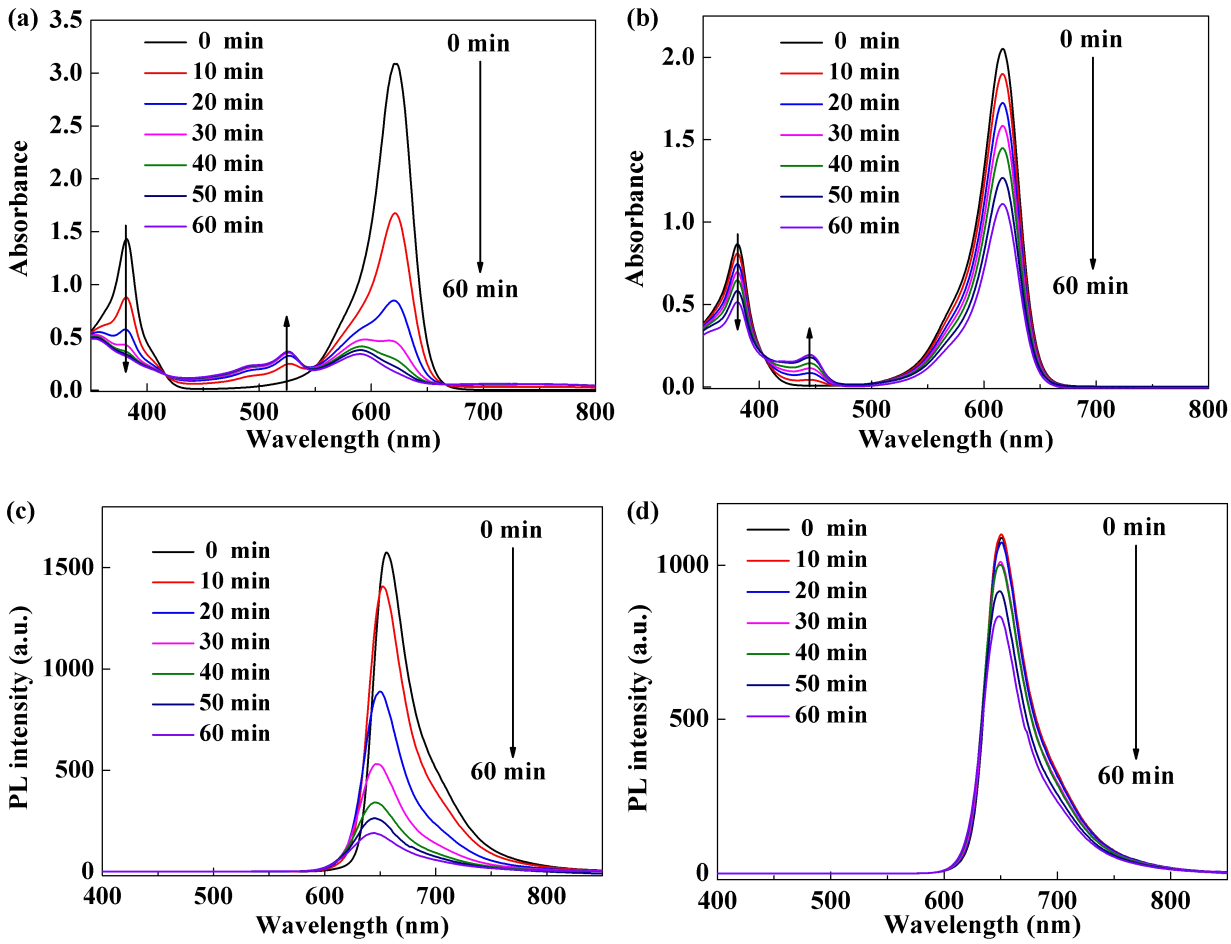

Figure 2-8. The changes of absorption spectra and PL spectra during *cis*-DCSQ1 exposed to incoherent UV (365nm) in different solvents: (a), (c) chloroform and (b), (d) DMF.

The decrease of PL intensity was observed in both chloroform and DMF as shown in Figures 2-8(c) and (d). However, it decreases quicker in chloroform than in DMF, which is consistent with the trend in their absorption spectra. The studied *cis*-DCSQ1 may exhibit the similar properties like polymethine-dyes. The negatively charged O in the cyclobutene moiety and positively charged N in the indolenine groups nitrogen atoms are the potential sites of interactions with solvent molecules and photochemical reactions in the films. However, in my study, identification of the decomposition compound was difficult.

2-4. Other derivatives

For fine-tuning the energy levels and preparing different substituted squaraine dyes, the development of a systematic strategy for molecular design is important. I focused on the Hammett substituent constant and molecular symmetry as quantitative indicators for choosing appropriate substituents. Further, two novel SQ derivatives were designed. One had a *cis*-configured structure containing a -$COOCH_2CH_3$ substituent (*cis*-DCSQ2) instead of the -CN substituent in *cis*-DCSQ1. The Hammett substituent constants of the -COOEt and -CN groups are 0.297 and 0.579, respectively [28], indicating that -COOEt is less electron withdrawing than -CN; therefore, I expected that the former might raise the energy levels of both the HOMO and the LUMO and reduce the overlap with CBP. The other had no acceptor units made an inversion center in the middle of the central squaric carbonyl group with a *trans* arrangement of the donor groups (*trans*-SQ1) as reference squaraines. Although *cis*-DCSQ1 and *cis*-DCSQ2 had similar optical properties in solution as shown in Figure 2-9, no ASE from 0.5 wt% *cis*-DCSQ2 doped CBP film could be obtained while a *cis*-DCSQ1 doped film with the same doping concentration showed ASE. The reason for the absence of ASE could be assumed to the lower FRET efficiency (79.9%), lower PLQY (21.4%), and lower k_r (0.67×10^8 s^{-1}) for *cis*-DCSQ2.

The PLQY of *cis*-DCSQ1 was higher than that of *cis*-DCSQ2 in solutions as shown in Table 2-2 and doped films, because the -$COOCH_2CH_3$ substituent is less electron withdrawing than the -CN substituent and thus the dipole moment of *cis*-DCSQ2 is lower than that of *cis*-DCSQ1. Additionally, the bulkier -$COOCH_2CH_3$ group increases the distortion of the π system away from planarity. As a consequence, additional vibrational states are coupled to the electronic transition, which promotes nonradiative deactivation processes of the excited-state, leading to the decrease in the PLQY of the *cis*-DCSQ2-doped film. For the same reason, *trans*-

SQ1 also has a lower PLQY of 30.7% in solution and no detectable PL in the doped film, making ASE difficult in this material. In addition, *trans*-SQ1 has weaker absorbance below 500 nm than that of *cis*-DCSQ1 because of the molecular symmetry changes. This means that there is smaller overlap between the absorption of *trans*-SQ1 and the PL of CBP compared with the case for *cis*-DCSQ1. These results suggest that SQ derivatives with high PLQY and large absorption in the film state, as observed for *cis*-DCSQ1, are necessary to realize ASE.

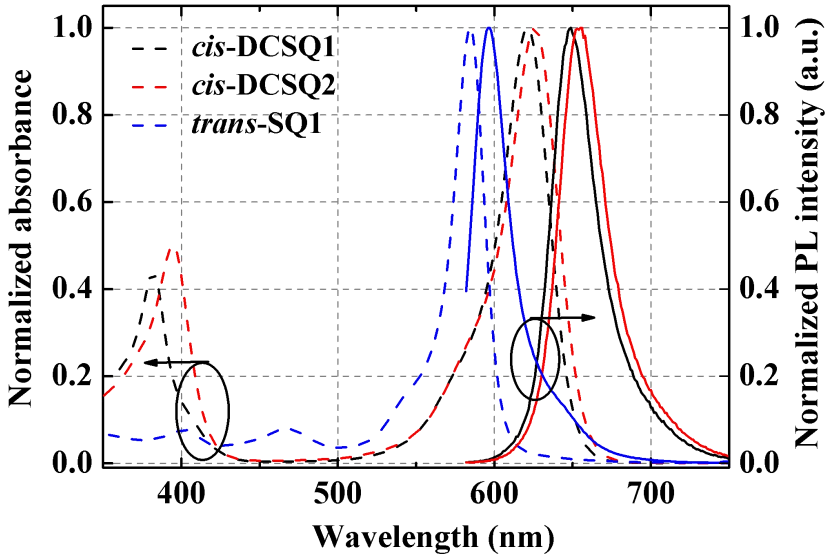

Figure 2-9. Absorption and PL spectra of SQ derivatives in chloroform.

Table 2-2. Summary of the maximum absorption wavelength (λ_{abs}), maximum PL wavelength (λ_{PL}), Stokes shift, FWHM, PL lifetime (τ), PLQY (Φ_{PL}), and radiative decay constant (k_r) of *cis*-DCSQ1, *cis*-DCSQ2, and *trans*-SQ1 solutions in chloroform at room temperature.

Materials	λ_{abs} (nm)	λ_{PL} (nm)	Stokes shift (nm)	FWHM (nm)	τ (ns)	Φ_{PL} (%)	k_r (10^8 s^{-1})
***cis*-DCSQ1**	621	649	28	37	5.04	82.5	1.64
***cis*-DCSQ2**	626	656	30	40	4.94	71.1	1.44
***trans*-SQ1**	585	597	12	24	1.67	30.7	1.84

2-5. Conclusion

Deep-red ASE from an SQ derivative (*cis*-DCSQ1) by using a host-guest system to suppress aggregation and induce efficient energy transfer was demonstrated. At a *cis*-DCSQ1 doping concentration of 0.5 wt%, the lowest ASE threshold was 10 μJ/cm^2 at 687 nm. Further development should be based on the spectral overlap with a suitable host, keeping the high PLQY with large dipole moment based on the strongly electron withdrawing substituent, and suppressing ACQ. Overall, my study opens a way to fabricate deep-red and NIR OSSLs using SQ derivatives. The new squaraine molecules system should have a strong absorption at pump wavelength and minimal absorption at lasing wavelength to minimize reabsorption losses for the emission. A good thermal and photochemical stability should also be considered for further advanced molecular design.

2-6. References

[1] F. Hide, M. A. D. Garcia, B. J. Schwartz, M. R. Andersson, Q. B. Pei, and A. J. Heeger, *Science*, **1996**, 273, 1833.

[2] Y. Kawamura, H. Yamamoto, K. Goushi, H. Sasabe, C. Adachi, and H. Yoshizaki, *Appl. Phys. Lett.*, **2004**, 84, 2724.

[3] T. Aimono, Y. Kawamura, K. Goushi, H. Yamamoto, H. Sasabe, and C. Adachi, *Appl. Phys. Lett.*, **2005**, 86, 071110.

[4] H. Nakanotani, S. Akiyama, D. Ohnishi, M. Moriwake, M. Yahiro, T. Yoshihara, S. Tobita, and C. Adachi, *Adv. Funct. Mater.*, **2007**, 17, 2328.

[5] D. H. Kim, A. S. D. Sandanayaka, L. Zhao, D. Pitrat, J. C. Mulatier, T. Matsushima, C. Andraud, J. C. Ribierre, and C. Adachi, *Appl. Phys. Lett.*, **2017**, 110, 023303.

[6] Y. F. Zhang, and S. R. Forrest, *Phys. Rev. B: Condens. Matter Mater. Phys.*, **2011**, 84, 241301.

[7] E. M. Calzado, J. M. Villalvilla, P. G. Boj, J. A. Quintana, R. Gómez, J. L. Segura, and M. A. D. García, *Appl. Opt.*, **2007**, 46, 3836.

[8] U. Mayerhöffer, K. Deing, K. Gruß, H. Braunschweig, K. Meerholz, and F. Würthner, *Angew. Chem. Int. Ed*., **2009**, 48, 8776.

[9] B. Stender, S. F. Völker, C. Lambert, and J. Pflaum, *Adv. Mater.*, **2013**, 25, 2943.

[10] S. Sreejith, P. Carol, P. Chithraa, and A. Ajayaghosh, *J. Mater. Chem.*, **2007**, 18, 264.

[11] S. Cohen, J. R. Lacher, and J. D. Park, *J. Am. Chem. Soc.*, **1959**, 81, 3480.

[12] C. J. Qin, Y. Numata, S. F. Zhang, A. Islam, X. D. Yang, K. Sodeyama, Y. Tateyama, and L. Y. Han, *Adv. Funct. Mater.*, **2013**, 23, 3782.

[13] A. Ajayaghosh, *Acc. Chem. Res.*, **2005**, 38, 449.

[14] S. Sreejith, P. Carol, P. Chithra, and A. Ajayaghosh, *J. Mater. Chem.*, **2008**, 18, 264.

[15] P. Anees, S. Sreejith, and A. Ajayaghosh, *J. Am. Chem. Soc.*, **2014**, 136, 13233.

[16] U. Mayerhöffer, M. Gsanger, M. Stolte, B. Fimmel, and F. Würthner, *Chem. Eur. J.*, **2013**, 19, 218.

[17] A. S. D. Sandanayaka, K. Yoshida, M. Inoue, C. J. Qin, K. Goushi, J. C. Ribierre, T. Matsushima, and C. Adachi, *Adv. Opt. Mater.*, **2016**, 4, 834.

[18] A. S. D. Sandanayaka, T. Matsushima, F. Bencheikh, K. Yoshida, M. Inoue, T. Fujihara, K. Goushi, J. C. Ribierre, and C. Adachi, *Sci. Adv.*, **2017**, 3, e1602570.

[19] V. K. Praveen, S. J. George, R. Varghese, C. Vijayakumar, and A. Ajayaghosh, *J. Am. Chem. Soc.*, **2006**, 128, 7542.

[20] A. Ajayaghosh, V. K. Praveen, C. Vijayakumar, and S. J. George, *Angew. Chem. Int. Ed.*, **2007**, 46, 6260.

[21] A. K. Sheridan, G. A. Turnbull, D. D. C. Bradley, and I. D. W. Samuel, *Synth. Met.*, **2001**, 121, 1759.

[22] H. Nakanotani, C. Adachi, S. Watanabe, and R. Katoh, *Appl. Phys. Lett.*, **2007**, 90, 231109.

[23] M. Anni, A. Perulli, and G. Monti, *J. Appl. Phys.*, **2012**, 111, 093109.

[24] E. M. Calzado, J. M. Villalvilla, P. G. Boj, J. A. Quintana, and M. A. Díaz-García, *J. Appl. Phys.*, **2005**, 97, 093103.

[25] D. Yokoyama, M. Moriwake, and C. Adachi, *J. Appl. Phys.*, **2008**, 103, 123104.

[26] A. K. Sheridan, G. A. Turnbull, A. N. Safonv, and I. D. W. Samuel, *Phys. Rev. B*, **2000**, 62, R11929(R).

[27] K. K. Anna, Z. B. Marta, C. Dorota, K. Przemysław, and K. Halina, *J. Photochem. Photobiol. A: Chem.*, 2016, 318, 77.

[28] C. J. Qin, Y. Numata, S. F. Zhang, X. D. Yang, A. Islam, K. Zhang, H. Chen, and L. Y. Han, *Adv. Funct. Mater.*, **2014**, 24, 3059.

Chapter 3

Near-infrared electroluminescence and low threshold of amplified spontaneous emission above 800 nm from a thermally-activated delayed fluorescent emitter

3-1. Introduction

NIR organic devices like OLEDs have attracted increasing interest in the recent years due to their potential applications in bioimaging, chemosensing, night-vision devices and information-secured displays [1, 2]. In fact, different kinds of emitters have been investigated for NIR EL, which include conjugated polymers [3, 4], organic conjugated D-A molecules [5-7], lanthanide-metal complexes [8, 9], phosphorescent metal complexes [10-12] and colloidal inorganic quantum dots (QDs) [13, 14]. However, the EQE values reported for NIR fluorescent organic emitters including both solution-processable polymers and thermally-evaporated small molecules remain below 2.1% [5, 15]. Lanthanide based NIR OLEDs with extremely sharp emission bands between 800 and 1600 nm have also been demonstrated but their EQE values remain still lower than 0.05% [8]. While high-efficiency solution-processable inorganic QDs have been used in LEDs emitting in the visible region with EQE close to 20% [16, 17], their EL performances in the NIR are not as good, with the highest EQE value of 8.6% obtained using silicon nanocrystals QDs emitting at about 850 nm [18]. The best NIR OLED performance achieved so far has been obtained using phosphorescent heavy metal complexes. In particular, a new class of phosphorescent platinum(II) complexes was recently proposed and used in NIR OLEDs with the EQE value over 24% [10]. However, due to the issues related to the shortage and high cost of heavy metals as well as the serious efficiency rolloff taking place at high current densities in PHOLEDs, the development of novel metal-free NIR fluorescent emitters with high PLQY that can overcome the spin statistic limitation of conventional fluorescent dyes is of great importance.

During the last six years, TADF emitters have been the subject of intensive studies and are now considered as the third generation of OLED materials [19]. High performance TADF OLEDs with 100% IQE have been already reported in the visible spectral range, providing

evidence of the strong potential of these purely aromatic emitters for display and lighting applications [20]. The molecular architecture of most efficient TADF OLED emitters developed so far is based on intramolecular CT twisted D-A systems exhibiting a small spatial overlap between their HOMO and LUMO distributions. Such a small spatial overlap leads to small energy-gap ΔE_{ST} between the S_1 and T_1, which greatly facilitates the RISC process and the triplet harvesting in TADF OLEDs. It is important to mention that a fine molecular design is required to tune the conjugation between the acceptor and donor moieties in these twisted D-A TADF systems, which is usually achieved by controlling their dihedral angle. This is a critical aspect to obtain simultaneously an effective RISC process and a large k_r. While this strategy has been proven to be successful for TADF OLEDs in the visible spectral range, the development of such twisted D-A TADF emitters remains challenging for high efficiency far-red and NIR EL [21]. This is essentially due to the fact that PLQY tends to decrease as the emission is red-shifted according to the energy-gap law [22] and also because of stronger ACQ effects [23] occurring in NIR emitting thin films.

In Chapter 2, the new material of squaraine derivatives toward deep-red emitter aimed for low ASE threshold was developed. However, these molecules are seriously lacking of photostability. To apply for organic lasers particularly under high current injection, the stability issues are very fundamental. Recently, our research group reported on highly efficient NIR TADF OLEDs with a maximum EQE value close to 10% at the maximum emission wavelength at the 721 nm using a solution-processable D-A-D borondifluoride curcuminoid derivative, named TPA-BCm as shown in Figure 3-1(a) [24]. The excellent NIR TADF properties of this compound were explained by the nonadiabatic coupling effect [24] taking place between its low lying excited-states. The high PLQY values (up to 70%), and large k_r measured in the NIR emitting films were associated with a strong spatial overlap between the

hole and electron wave functions. In case of small energy-gap materials, even though they have large overlap integral, we can obtain small ΔE_{ST} with high PLQY. This is quite different situation compared with that of visible TADF emitter. In addition to its strong potential for high performance NIR TADF OLEDs, this curcuminoid derivative was found to be also promising for NIR OSSLs, due to the direct consequence of the large PLQY and fast k_r of this emitter [24]. This latter finding is extremely relevant for further works devoted to the realization of CW OSSLs and OSLDs [25-28].

In this Chapter, I report novel solution-processable dimeric borondifluoride curcuminoid derivative DTPA-BC (see its chemical structures in Scheme 3-1 and Figure 3-1) containing triphenylamine (TPA) donor groups and acetylacetonate borondifluoride acceptor units. This molecule DTPA-BC has an electron withdrawing group in the meso position instead of the ester function in TPA-BCm. Although the efficiency of the electron-withdrawing properties of the ester in TPA-BCm and the acetylacetone borondifluoride appended in the meso position in DTPA-BC is similar, strong excitonic coupling effects taking place in TPA-BCm should result in a substantial shift of the emission toward longer wavelengths. Such a molecular structure is therefore expected to lead to a high-efficiency NIR TADF emission and a low threshold ASE further in the NIR as compared to those of TPA-BCm. The results demonstrated that the original molecular design of the dimeric curcuminoid derivative reported in this study offers indeed the possibility to extend the emission wavelength of NIR TADF OLEDs and OSSLs above 800 nm while keeping excellent EL, ASE and lasing performances. Importantly, the unprecedented demonstration of ASE at wavelengths longer than 800 nm in an organic semiconductor thin film should have a strong impact on future research devoted to OSSLs and optical amplifiers operating at telecommunication wavelengths.

3-2. Experimental

All solvents for synthesis were of analytic grade. NMR spectra (^{1}H, ^{13}C) were recorded at room temperature on JEOL JNM ECS 400 operating at 400 and 100 MHz for ^{1}H and ^{13}C, respectively. Data are listed in parts per million (ppm) and are reported relative to tetramethylsilane (^{1}H and ^{13}C); residual solvent peaks of the deuterated solvents were used as internal standards. Mass spectra were realized in Spectropole de Marseille.

Cyclic voltammetry (CV) data were acquired using a BAS 100 Potentiostat (Bioanalytical Systems) and a PC computer containing BAS100W software (v2.3). A three-electrode system with a Pt working electrode (diameter 1.6 mm), a Pt counter electrode and an Ag/AgCl (with 3 M NaCl filling solution) reference electrode was used. [(*n*-Bu)$_4$N]PF$_6$ (0.1 M in CH_2Cl_2) served as an inert electrolyte. Cyclic voltammograms were recorded at a scan rate of 100 mV s^{-1}. Ferrocene was used as internal standard.

Synthesis of DTPA-BC

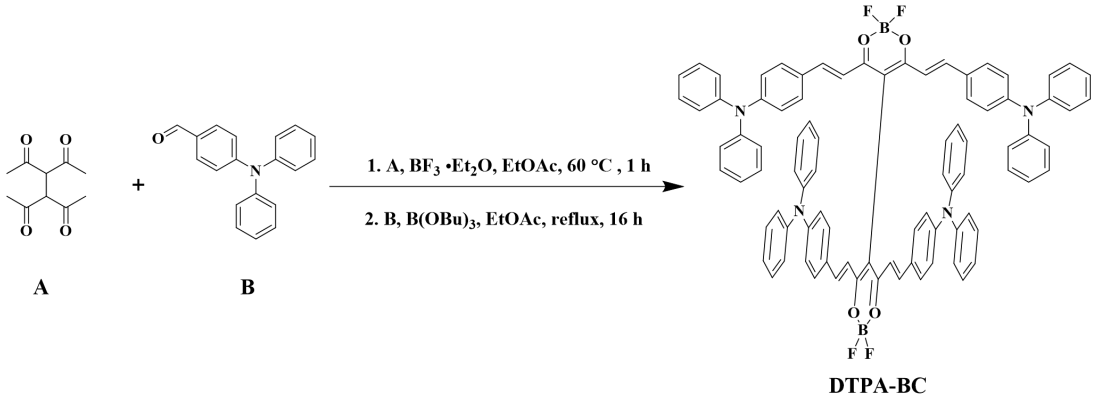

Scheme 3-1. Synthetic pathway for the synthesis of DTPA-BC.

In a 100 mL flask, the mixture of 1,1,2,2-tetraacetylethane **A** (500 mg, 2.523 mmol, 1 eq) and $BF_3{\cdot}Et_2O$ (666 µL, 5.297 mmol, 2.1 eq) in 3 mL ethyl acetate was heated for 30 min at 50-60 °C in air. Dissolved 4-(*N*,*N*-Diphenylamino)-benzaldehyde **B** (2.90 g, 10.597 mmol, 4.2 eq)

and $B(OBu)_3$ (2.439 g, 10.597 mmol, 4.2 eq) into 40 mL ethyl acetate, then the solution was injected into the first mixture. Kept the reaction at 50-60 ^oC for another 30 min. First portion of morpholine (176 μL, 2.018 mmol, 0.8 eq) was added dropwise into the reaction. After 6 h heating, second portion of morpholine (176 μL, 2.018 mmol, 0.8 eq) was added, and the reaction was kept heating at 50-60 ^oC overnight. All the solvents were evaporated. The crude product could be obtained by flash column chromatography (silica, CH_2Cl_2). Further purification was done by many times precipitation in CH_2Cl_2/petroleum ether, giving dark green powder DTPA-BC (712 mg, 22% yield).

^1H NMR (400 MHz, CD_2Cl_2) δ (ppm): 8.02 (d, J = 15.2 Hz, 1H), 7.41 (d, J = 9.2 Hz, 2H), 7.32 (m, 4H), 7.14 (m, 6H), 6.69 (d, J = 9.2 Hz, 2H), 6.58 (d, J = 15.2 Hz, 1H); ^{13}C NMR (100 MHz, $CDCl_3$) δ (ppm): 178.5, 151.8, 148.9, 146.0, 131.5, 129.7, 126.7, 126.1, 125.1, 120.1, 114.5, 105.4. HRMS (ESI+) [M-H]- calcd for $C_{86}H_{64}N_4O_4B_2F_4CH_3COO^-$ m/z = 1373.5214, found m/z = 1373.5201.

For the characterization of the photophysical properties in solution, DTPA-BC was dissolved in solvents having different polarities at the concentration around 10^{-6} M and the solutions were placed in quartz cuvettes. Note that all solvents used for these photophysical measurements were of spectroscopic grade. For the characterization of the photophysical and ASE properties in thin films, the films were deposited onto precleaned fused silica substrates by spin-coating from chloroform solution. The thickness of these films were measured using a Dektak profilometer (AC-3) and found to be typically around 120 nm.

Absorption spectra in both solution and film were recorded using a Varian Cary 5000 spectrometer and a UV-2550 spectrometer (Shimadzu), respectively. Steady-state PL spectra were obtained using a Fluoromax-4 spectrophotometer (Horiba Scientific), and corrected following the procedure reported by Parker et al. [29] to take into account the response of the

detector [30]. The PLQY values in solution were measured using ruthenium trisbipyridine bischloride (PLQY of 0.021 in water) as a reference [31]. For the thin films, PLQYs were determined using an integrating sphere system coupled with a photonic multichannel analyzer (C9920-02, PMA-11, Hamamatsu Photonics) under a flowing nitrogen atmosphere [32].

For the time-resolved PL measurements at room temperature, thin films were placed in vacuum ($< 4 \times 10^{-1}$ Pa). A nitrogen laser (Ken-X, Usho Optical systems) delivering 500 ps excitation pulses with a wavelength of 337 nm and a repetition rate of 20 Hz was used for the photo-excitation. The transient PL emission was recorded using a streak camera (C4334, Hamamatsu Photonics). Another experimental setup was used to properly investigate the prompt fluorescence process taking place at shorter time scale. For this purpose, a Noncolinear Optical Parametric Amplifier (NOPA) pumped by a fiber femtosecond laser (Amplitude Systemes Tangerine) and a streak camera (Hamamatsu PLP system) with a time resolution around 10 ps were used. In those measurements, the pulse width and the repetition rate of the photo-excitation at the wavelength of 560 nm were 100 fs and 10 kHz, respectively.

For the characterization of the ASE properties, the samples in nitrogen atmosphere were photo-excited by a nitrogen laser (excitation wavelength of 337 nm, pulse width of 800 ps and repetition rate of 8 Hz). A set of neutral density filters were used to vary the energy of the excitation pulses. The excitation beam was focused using a cylindrical lens into a stripe of dimension 0.5 cm × 0.08 cm. The emission was detected from the edge of the organic film using an optical fiber connected to a charge-coupled device spectrometer (PMA-11, Hamamatsu Photonics).

Regarding the fabrication of OLEDs, poly(3,4-ethylene dioxythiophene): poly (styrenesul--fonate) (PEDOT:PSS) was purchased from Heraeus CleviosTM while CBP, 2,2',2''-(1,3,5-benzinetriyl)-tris(1-phenyl-1*H*-benzimidazole) (TPBi) and bis[2-(diphenylphosphino)phenyl]

ether oxide (DPEPO) were supplied by TCI chemicals. The PEDOT:PSS layers were deposited by spin-coated on top of cleaned pre-patterned ITO glass substrates and then annealed at 180 ^{o}C for 30 min. The CBP: DTPA-BC blends with different doping concentrations were spin-coated on top of PEDOT:PSS layer from a chloroform solution. DPEPO and TPBi films were then thermally evaporated and cathodes consisting of 1 nm thick LiF and 100 nm thick Al were finally deposited by thermal evaporation to complete the devices. The active area of the devices was designed to be 4 mm^2. Importantly, the devices were encapsulated in a glove box filled with nitrogen to avoid contamination by oxygen and moisture. For the characterization of the OLEDs, current(J)-voltage(V)-luminance(L) characteristics were obtained under direct current driving using a source meter (Keithley 2400, Keithley Instruments Inc.) and EQE measurement were performed using C9920-12, Hamamatsu Photonics detector. The EL spectra were recorded using an optical fiber connected to a spectrometer (PMA-11, Hamamatsu Photonics). Similarly to what we did for the PL spectra, the spectroscopic sensitivity factor of the detector was taken into account to obtain the corrected emission EL spectra following the procedure reported by Parker et al. [29].

In addition, the group of Prof. Jean-Luc Brédas from Georgia Institute of Technology have carried out quantum chemical calculations to characterize the geometric and electronic structures of DTPA-BC. The initial geometry of the dye molecule was optimized with the range-separated functional ωB97XD, using the default range-separation parameter ω of 0.2 $bohr^{-1}$ and the 6-31G(d,p) basis set [33]. Then, an iteration procedure was employed to non-empirically tune the ω parameter with the implicit consideration of the dielectric environment via the polarizable continuum model (PCM). The dielectric constant ε was chosen to be 4.0, a representative value of nonpolar organic semiconductor materials. The Tamm-Dancoff approximation (TDA) in the framework of time-dependent density functional theory (TD-DFT)

was employed to study the excited-state properties. All the excited-state properties of the molecule were examined at the TDA-tuned-ωB97XD/6-31G(d,p) level. All the quantum chemical calculations were performed with the Gaussian 09 Rev D01 program. The SOC were estimated by employing the Breit-Pauli spin-orbit Hamiltonian with an effective charge approximation implemented in the PySOC code [34].

3-3. Results and discussion

3-3-1. Quantum chemical calculations

The quantum chemical calculations based on tuned ωB97XD/6-31G(d,p) level of theory with the Gaussian 09 Rev D01 program were carried out in a previous study to examine the electronic properties of TPA-BCm and rationalize the mechanism of its TADF activity [24, 35]. It was demonstrated that the TADF process in this molecular system occurs through nonadiabatic coupling (or vibronic coupling) effect between two low-lying excited-states. Such an effect mediated by molecular vibrations has been found to play a major role in the RISC upconversion in a class of D-A-D molecules [35]. In case of TPA-BCm, several low frequency vibration modes, related to the rotations of the terminal phenyl groups were identified. These rotations induce a near degeneracy of the S_1 and S_2 states as well as the T_1 and T_2 states (i.e, conical intersection), which leads to: 1) a decrease in the ΔE_{ST} values, 2) a strong vibronic coupling between the S_1 and S_2 states and between the T_1 and T_2 states, and 3) the opening of T_1 to S_2 and T_2 to S_1 upconversion channels due to larger SOC than between T_1 and S_1. The combination of these features is what rationalizes the very efficient RISC process observed experimentally [24].

In this study, quantum chemical calculations to examine the electronic properties of DTPA-BC only at its ground-state optimized geometry were performed, since excited-state geometry optimization were computationally prohibitive due to the large size of DTPA-BC and vibrational coupling effect, which made it more complicated. The results are summarized in Figure 3-1 and Table 3-1 with the molecular structures of DTPA-BC and TPA-BCm. The substantial overlap of hole and electron wavefunctions in the S_1 state of DTPA-BC is consistent with what has been observed in TPA-BCm. Such features should be associated with very high S_0-S_1 TDM and thus a fast fluorescent k_r, which is necessary for an efficient ASE and lasing

activity as introduced in Chapter 1. On the other hand, if considering the optimized geometries, the estimated ΔE_{ST} is high, on the order of 300 meV, whereas the SOC between the S_1 and T_1 states was found to be 0.13 cm^{-1}. Compared with the reported TADF emitters, summarized in Table 3-2 and Figure 3-2 [24, 36-38], this should lead to a weak k_{RISC}. Considering the chemical structures of the TPA-BCm and DTPA-BC, similar nonadiabatic coupling effects that have been evidenced in TPA-BCm should also take place in DTPA-BC, because these effects are indeed directly related to the vibrations of the TPA groups present in both derivatives.

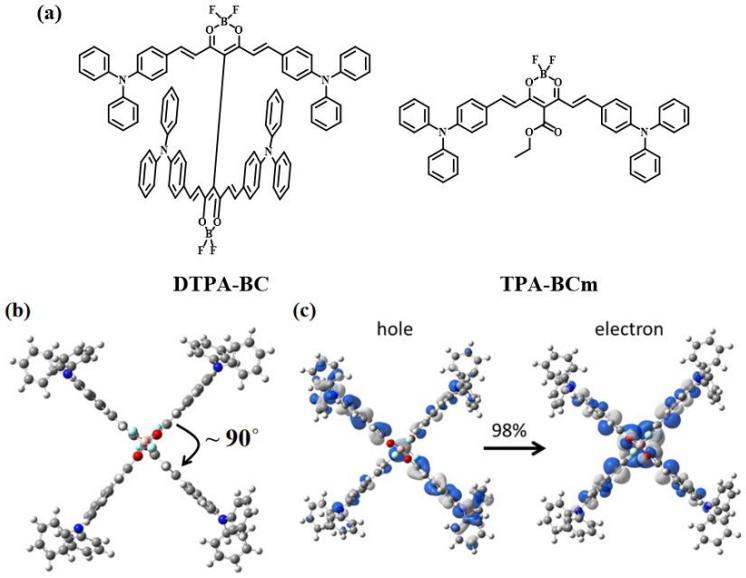

Figure 3-1. (a) Molecular structures of DTPA-BC and TPA-BCm. (b) Optimized ground-state geometry of DTPA-BC at tuned ωB97XD/6-31G(d,p) level of theory. (c) Natural transition orbitals describing the S_1 state of DTPA-BC.

Table 3-1. Calculated vertical excitation energies of the S_1, S_2, T_1, and T_2 states at that fixed geometry and estimated average SOC between the low-lying excited electronic states at the optimized ground-state geometry.

Excitation energy (eV)			SOC (cm^{-1})
E (S_1)	2.01	**S_1-T_1**	0.13
E (S_2)	2.01	**S_1-T_2**	0.32
E (T_1)	1.69	**S_2-T_1**	0.28
E (T_2)	1.69	**S_2-T_2**	0.13

Table 3-2. Summary of the calculated ΔE_{ST}, SOC, and k_{RISC} of organic emitters [24, 36, 37].

Ref.	Molecule	ΔE_{ST} (eV)	SOC_{S1-T1} (cm^{-1})	k_{RISC} (10^6 s^{-1})	TADF
24	TPA-BCm	0.37	0.04/0.12[a]	-	Yes
36	PTZ-DBTO2	0.1	2	0.07	Yes
37	CBP	0.88	< 0.01	< 0.01	No
37	α-NPD	0.76	0.68	< 0.01	No
37	CC2TA	0.16	0.30	0.11[b]	Yes
37	PIC-TRZ	0.11	0.28[a]	1.1[b]	Yes
37	4CzTPN	0.06	0.81	44.3	Yes
37	4CzTPN-Me	0.09	0.31	2.34	Yes
37	4CzIPN	0.01	0.27	18.3	Yes
37	4CzIPN-Me	0.04	0.17	3.5	Yes
37	Spiro-CN	0.01	0.61[a]	48[b]	Yes
37	PXZ-TRZ	0.09	1.54[a]	14[b]	Yes
37	ACRFLCN	0.02	0.46	43	Yes
37	4CzPN	0.00	0.61	114	Yes
37	2CzPN	0.25	0.74	0.0021	Yes

a: These values correspond to T_2 to S_1 transitions. b: The values were calculated by taking into account the ISC not only directly from T_1 to S_1 but also from T_1 via T_2 to S_1.

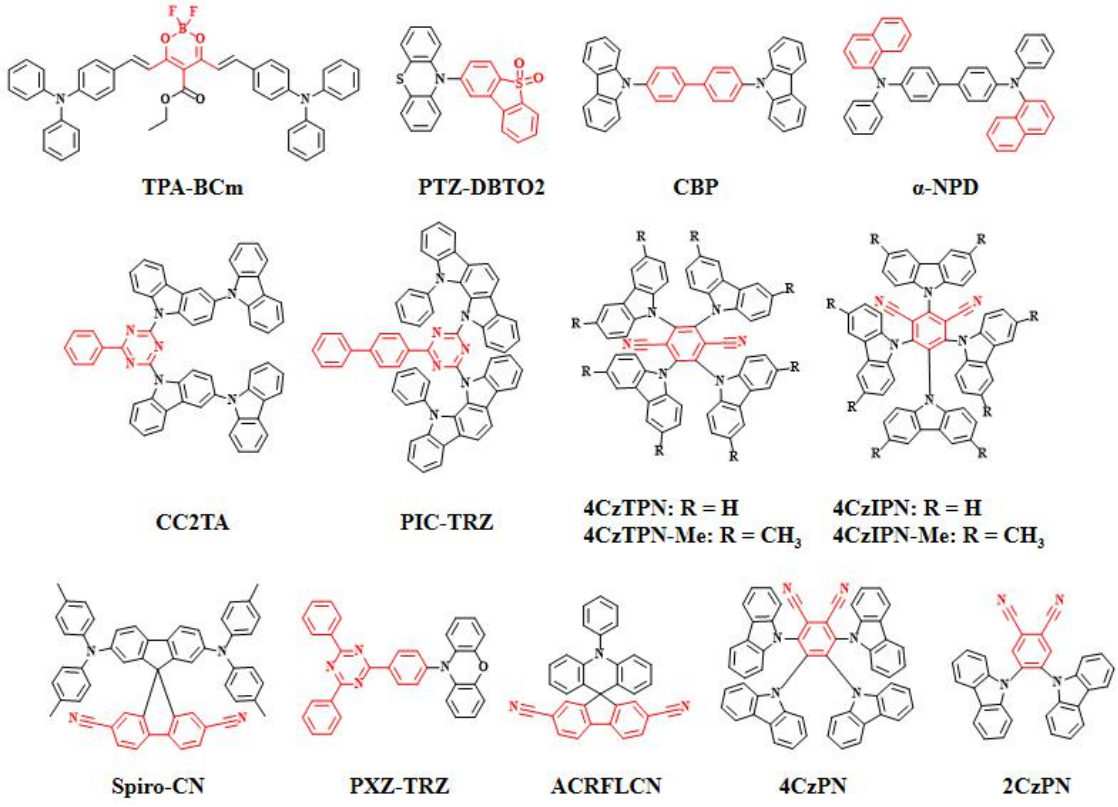

Figure 3-2. Chemical structures of the molecules discussed. The black and red color denote the donor (electron-rich) and acceptor (electron-poor) molecular fragments, respectively.

3-3-2. Photoluminescent properties

The HOMO and LUMO energy levels of DTPA-BC were determined from CV measurements and the results reported in Figure 3-3 lead to values of -5.6 and -3.7 eV, respectively. This is consistent with the ionization potential (HOMO energy) of -5.6 eV obtained from photoelectron spectroscopy measurements in air and the electron affinity (LUMO energy) of -4.0 eV approximated using the optical bandgap. It is to be highlighted that the LUMO energy obtained by electrochemistry is slightly different from the one obtained using the optical band gap. This can however be explained by the excitonic coupling which has been observed in other dimeric structure of curcuminoid boron difluoride [38]. Noticeably, the HOMO and LUMO energy levels of DTPA-BC are nearly identical with the values previously reported in TPA-BCm (HOMO: -5.5 eV, LUMO: -3.8 eV) [24].

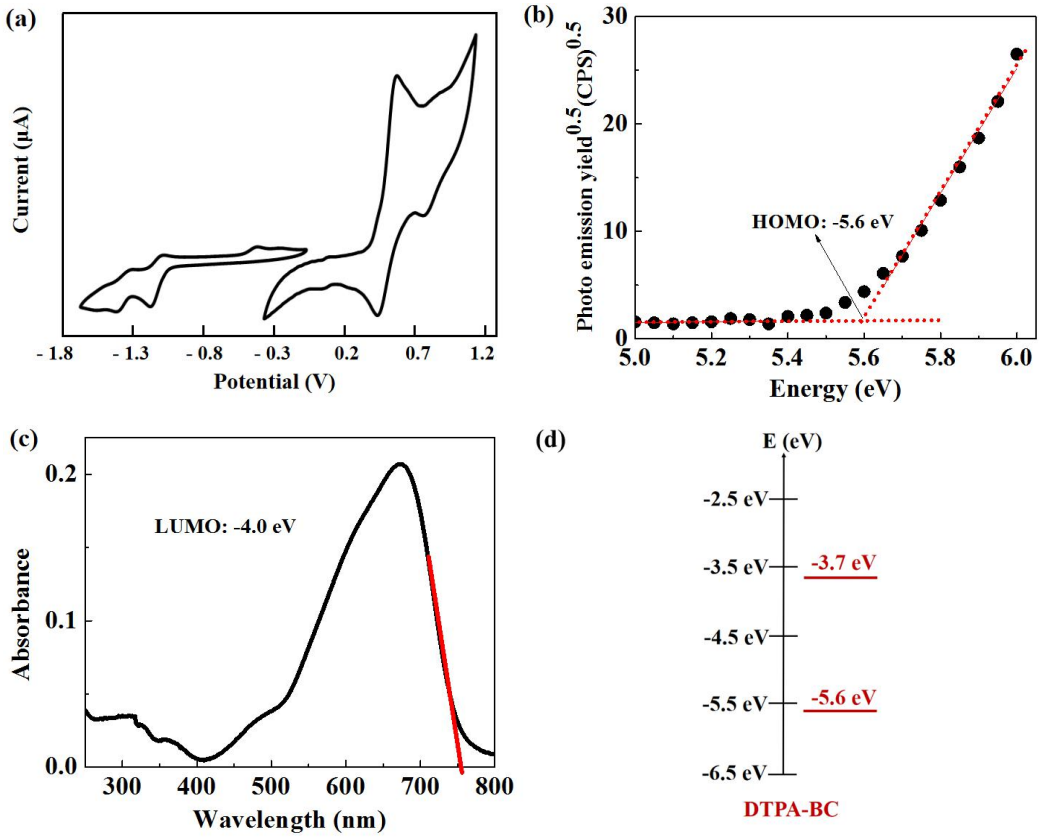

Figure 3-3. (a) CV of DTPA-BC in CH_2Cl_2 solution. (b) Ionization potential of a DTPA-BC neat film. (c) The absorption spectrum of a DTPA-BC neat film. (d) HOMO and LUMO energy levels determined by CV.

The photophysical properties of DTPA-BC were investigated at the low concentration (<1 × 10^{-6} M) in solvents of different polarities and are summarized in Table 3-3. The results reported in Figure 3-4 show the orange-red absorption and the NIR emission of the dye in solutions. Noticeably, the non-aggregated dye exhibits a molar absorption coefficient as high as 1.05 × 10^5 $M^{-1}cm^{-1}$ in CH_2Cl_2 solution which is in line with the one reported for TPA-BCm and *cis*-DCSQ1. However, such a value is not double the one obtained for TPA-BCm, which further shows the excitonic coupling in DTPA-BC. A strong positive solvatochromism for both absorption and steady-state PL spectra was also observed when increasing the solvent polarity, which is due to the CT character of the ground-state and singlet excited-states of the dye. Importantly, the PL spectrum is substantially shifted toward longer wavelengths while the PLQY gradually decreases from 41% in cyclohexane (at 649 nm) to 1.3% in CH_2Cl_2 (at 788 nm) as shown in Table 3-3 with the polarity of the solvents. Such a behavior is consistent with the data obtained for another curcuminoid boron difluoride dye possessing high ground- and excited-state dipole moments [39]. Furthermore, Lippert-Mataga plot in Figure 3-5 shows that the variation of dipole moments is similar for DTPA-BC and TPA-BCm, providing additional evidence about the larger excited-state dipole moments in those dyes compared to the ground-state ones.

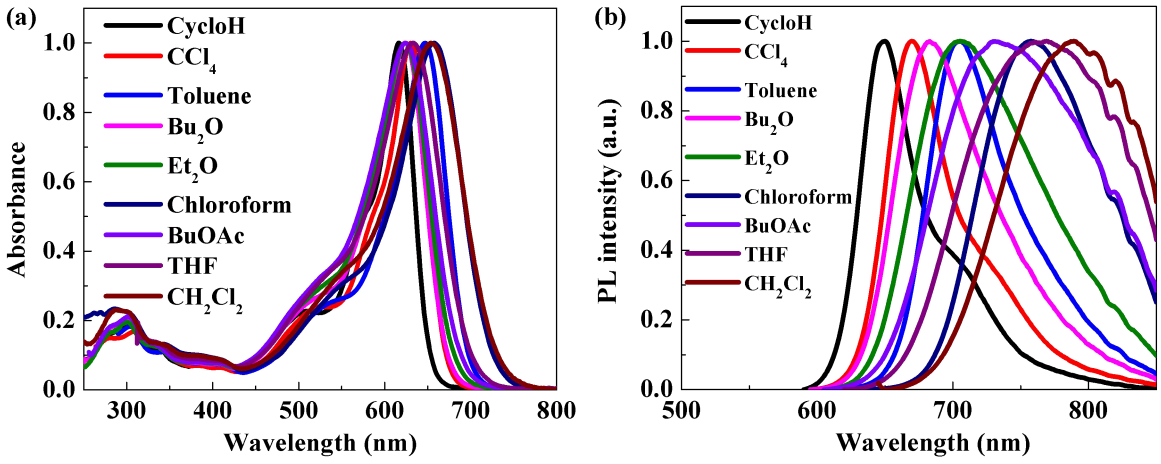

Figure 3-4. (a) Absorption and (b) Emission spectrum of DTPA-BC in different solvents.

Table 3-3. Photophysical data in solvent of various polarities.

Solvent	λ_{abs} (nm)	λ_{PL} (nm)	$\Delta\nu$ (cm^{-1})	Φ_{PL}	τ (ns)	k_r (10^8 s^{-1})	k_{nr} (10^8 s^{-1})
CycloH	616	649	825	0.410	1.86	2.20	3.17
CCl_4	630	670	948	0.397	2.00	2.00	3.02
Bu_2O	624	683	1384	0.364	2.20	1.70	2.89
Et_2O	624	706	1861	0.222	2.00	1.10	3.89
Chloroform	657	759	2045	0.172	1.88	0.91	4.40
AcOEt	627	762	2826	0.010	0.18	0.56	55.30
THF	633	767	2760	0.011	0.24	0.47	41.90
CH_2Cl_2	654	788	2600	0.013	0.36	0.36	27.60

Stokes shift $\Delta\nu$, nonradiative rate constant $k_{nr} = (1 - \Phi_{PL})/\tau$, Et_2O: ethylic ether, AcOEt: ethyl acetate, CH_2Cl_2: dichloromethane, ACN: acetonitrile.

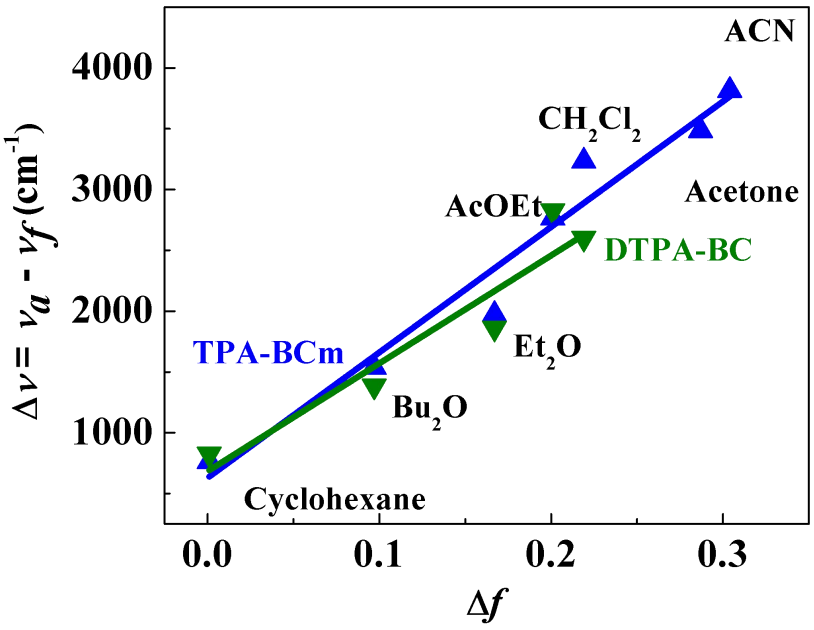

Figure 3-5. Lippert-Mataga plot for DTPA-BC and TPA-BCm. The Stokes shift ($\Delta\nu$) is shown as a function of the orientation polarizability Δf. Δf is calculated using dielectric constant (ε) and refractive index (n) of each solvent as $\Delta f = [(\varepsilon - 1)/(2\varepsilon + 1)] - 0.5\,[(n^2 - 1)/(2n^2 + 1)]$.

To gain insights into the photophysical properties of the NIR emitting dye in thin films, DTPA-BC was blended into CBP host at various doping concentrations. The doping concentration of the absorption and steady-state PL spectra of the CBP blends is displayed in Figures 3-6(a) and (b), respectively. As the doping concentration increases from 1 to 40 wt%,

the NIR PL spectrum is gradually shifted toward the longer wavelengths from 751 to 801 nm. Such a behavior has been already observed with other NIR emitters possessing a large ground-state dipole moment and is attributed to the influence of the doping concentration on the polarity of the medium together with the formation of aggregated species in highly doped thin films. There is a spectral overlap between the emission spectrum of CBP and the absorption spectrum of DTPA-BC, implying that a FRET can take place from the host to the dopant molecules. The results displayed in Figures 3-7(a) and (b) confirm that such an energy transfer takes place quite efficiently in the blends with CBP emission; the PLQY based on CBP at the lowest doping concentration of 1 wt% was 4%, and it decreased to 2% at 2 wt% and became negligible at 6 wt%. The PLQY of the NIR emission at the various doping concentrations was then characterized and the results are reported in Figure 3-6(c) and Table 3-4. The 40 wt% CBP blend exhibits a PLQY of about 4% with a maximum emission wavelength of 801 nm. A gradual increase of PLQY from 4% to 45% is then observed as the doping concentration decreases from 40 wt% to 2 wt%. Noticeably, the PLQY measured in the 1 wt% CBP blend is lower than the value of 27.5%, which is related to the observation of an incomplete energy transfer from the host to the dopant molecules. It is worth noticing that for any doping concentration of the dyes in a CBP host, the PLQY values of DTPA-BC are lower than those of TPA-BCm. This behavior is related to the red-shift of the emission which causes a larger nonradiative effect due to the larger π-conjugation between the two curcuminoid boron difluoride units and the corresponding energy-gap law.

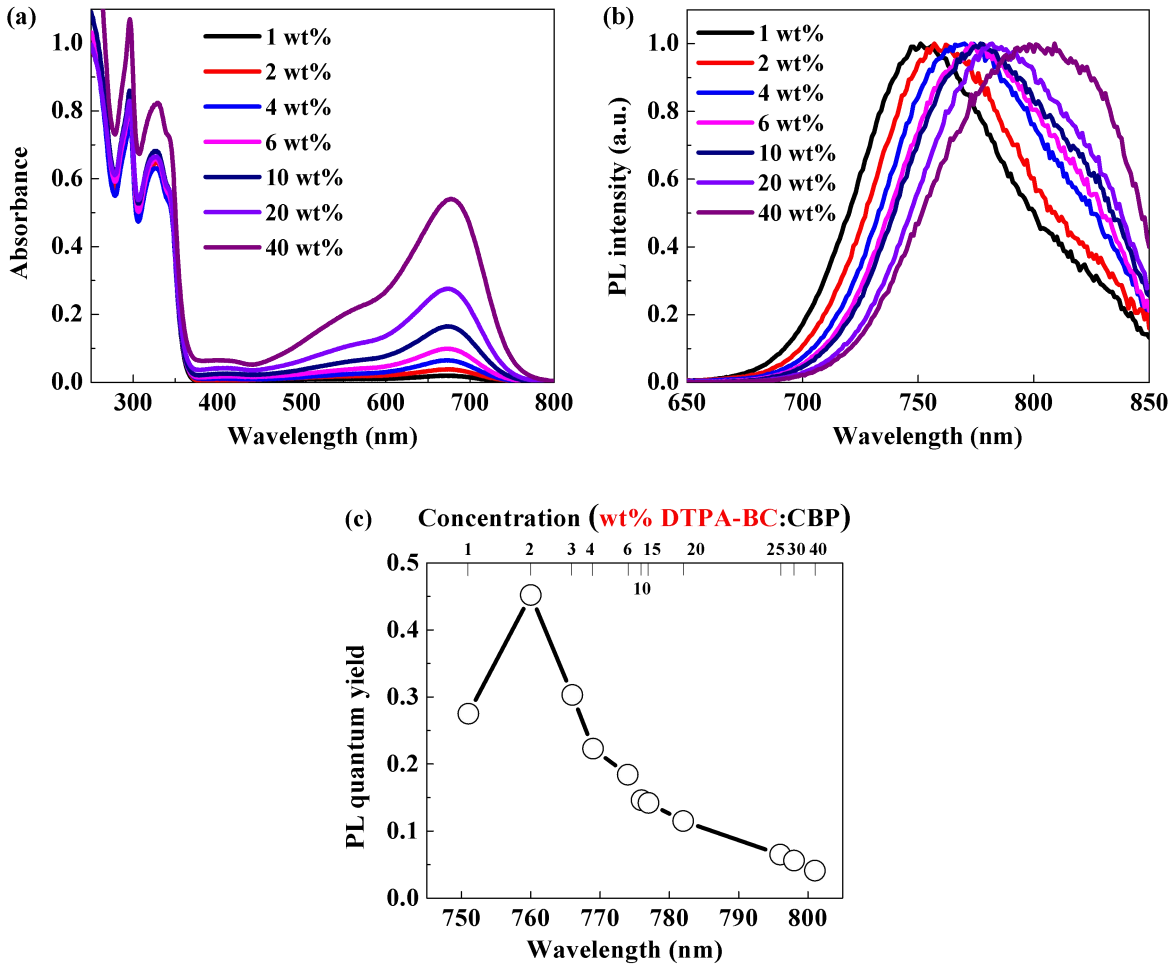

Figure 3-6. (a) Absorption and (b) Steady-state PL spectra of the DTPA-BC:CBP blends. Excitation wavelength was 610 nm. (c) Variation of the PLQY as function of emission wavelength and doping concentration.

Table 3-4. Summary of the maximum PL emission and PLQY measured in CBP blends with different doping concentrations.

DTPA-BC:CBP (wt%)	λ_{PL} (nm)	PLQY
2	760	0.452
3	766	0.303
4	769	0.223
6	774	0.184
7	775	0.169
8	775	0.158
10	776	0.146
15	777	0.142
20	782	0.115
25	796	0.065
30	798	0.056
40	801	0.041

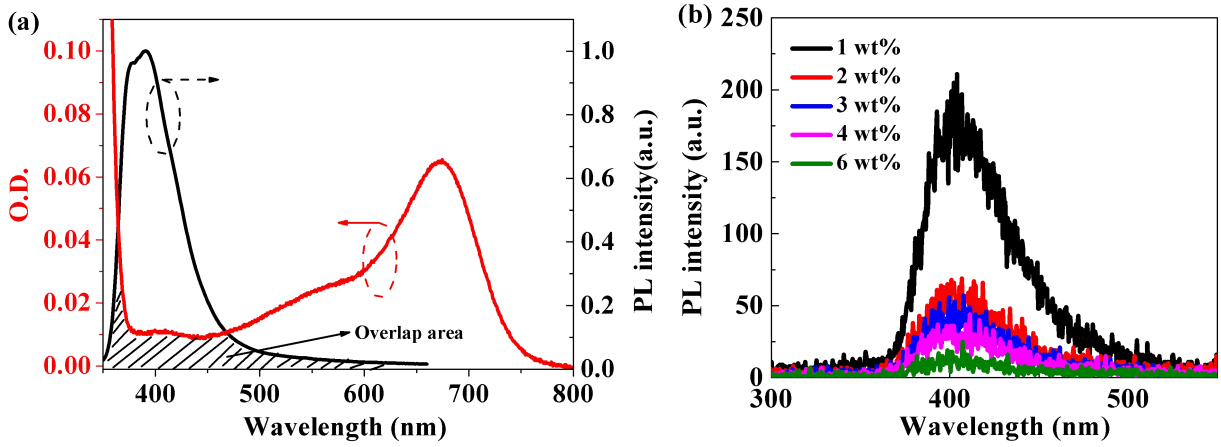

Figure 3-7. (a) Spectral overlap between the emission spectrum of a CBP film and absorption spectrum of DTPA-BC film. (O.D.: Optical Density). (b) Residual emission of CBP films with different concentrations of DTPA-BC.

Time-resolved PL measurements were then carried out in the 2 wt% CBP doped film to characterize the TADF activity of DTPA-BC. As shown in Figure 3-8(a), the PL decays obtained at room temperature reveal the presence of both prompt and delayed fluorescence components originating from the same S_1. Similarly to what has been reported in TPA-BCm [24], the delayed emission component vanishes at 77 K. These results confirm the efficient RISC process taking place at room temperature through thermal activation in borondifluoride curcuminoid derivatives. In addition, a significant wavelength dependence of the PL kinetics is observed, which can be assigned to the presence of monomeric and aggregated NIR emitting species in the blend films. Importantly, as shown in Figure 3-8(b), the TADF activity of the NIR emitter involving two RISC processes due to the presence of monomeric and aggregated species is affected by a change in the doping concentration. This can be explained by the CT character of both singlets and triplets in this specific molecular system and the changes of the effective polarity of the medium as the doping concentration varies. Here, I note that the emission is red-shifted for DTPA-BC compared to TPA-BCm which is the result of both

increased electron withdrawing character of the acetylactonate borondifluoride moiety and excitonic coupling between the two dyes covalently bound.

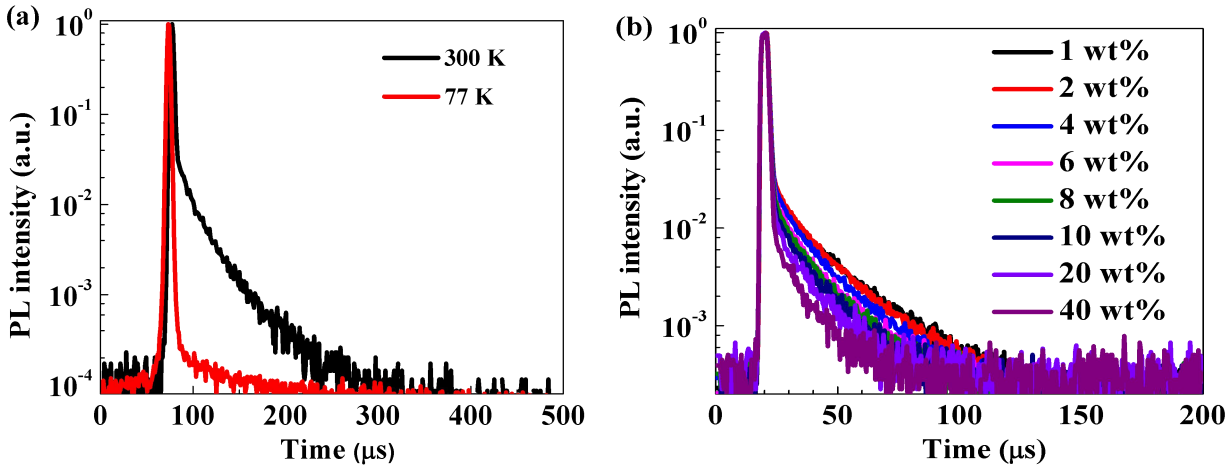

Figure 3-8. (a) PL decays of a 2 wt% DTPA-BC:CBP blend film at room temperature and 77 K. (b) PL decays in various CBP blend films with different doping concentrations at room temperature.

3-3-3. Electroluminescent properties

The EL properties of the dimeric curcuminoid derivative were examined using the following OLED architecture: glass substrate / indium tin oxide (ITO) (100 nm) / PEDOT:PSS (45 nm) / EML (80 nm) / DPEPO (10 nm) / TPBi (55 nm) / LiF (1 nm) / Al (100 nm), where PEDOT:PSS, DPEPO and TPBi play the role of HIL, HBL, and ETL, respectively. The molecular structures of PEDOT:PSS, DPEPO, and TPBi are shown in Figure 3-9.

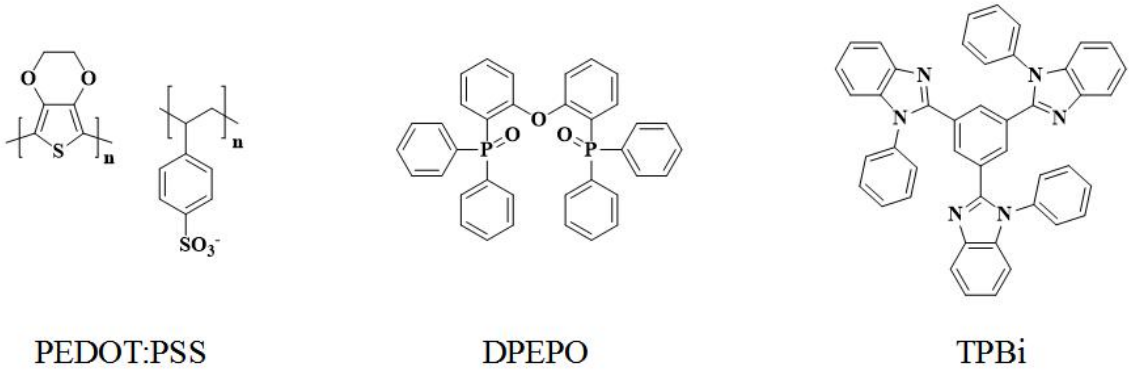

Figure 3-9. Molecular structures of PEDOT:PSS, DPEPO, and TPBi .

The energy-level diagram and the schematic representation of the device architecture are displayed in Figure 3-10(a). The EML tested in the devices were composed of the DTPA-BC:CBP blends with various doping concentrations. As shown in Figure 3-10(b), the NIR EL spectra are fully consistent with the PL spectra and shift toward longer wavelengths as the doping concentration increases. For instance, the maximum EL and PL wavelength of the 2 wt% CBP blend film is found to be around 760 nm. It is worth noting that the CBP blends with a doping concentration at 1 wt% and 2 wt% show an emission from the CBP host, indicating an incomplete energy transfer from the CBP to the NIR emitting guest molecules due to too large intermolecular spacing distances between neighboring dyes.

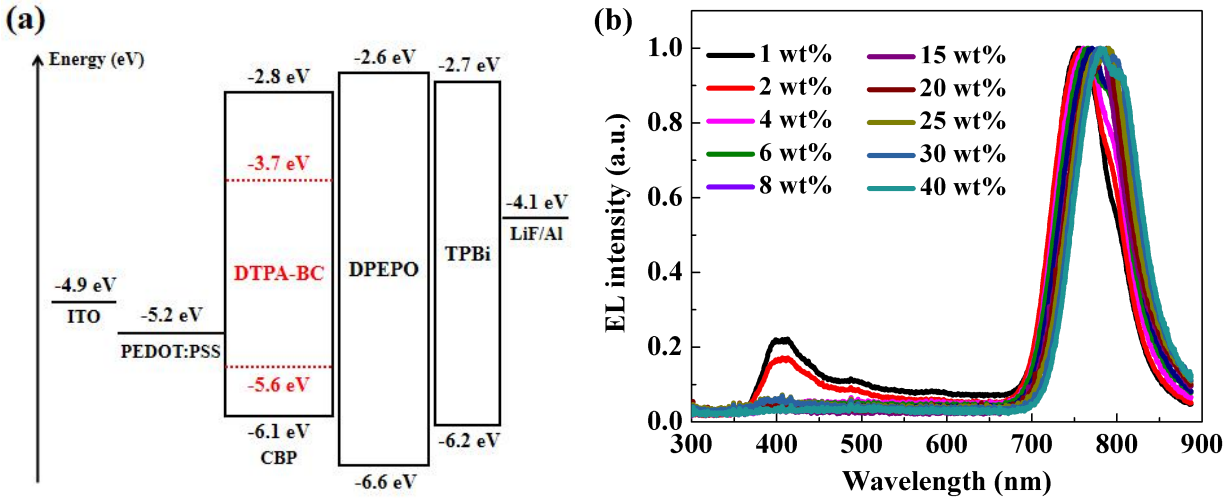

Figure 3-10. (a) The energy-level diagram and schematic representation of the OLED device architecture. (b) NIR EL spectra measured for various doping concentrations.

The EQE values were measured as a function of the current density in all devices. The results in Figure 3-11(a) clearly show an increase of the maximum EQE value as the doping concentration decreases from 40 to 2 wt%, which is in perfect agreement with the behavior of the doping concentration dependence of the PLQY. Noticeably, the most efficient device based on the 2 wt% blend exhibits a maximum EQE value of 5.1% as shown in Table 3-5. Considering its PLQY value of 45.2% and assuming a random orientation of the NIR TADF emitters, this excellent efficiency value is higher than the theoretical upper limit of 2.25% that could be obtained with a conventional fluorescent emitter and can be explained by the TADF activity of the dye. Similarly to what was observed with TPA-BCm [24], the OLEDs suffer however from a severe rolloff at high current densities. Noticeably, this rolloff decreases with the doping concentration which is in line with the decreased efficiency of the TADF process at the high concentration of dye. As shown in Figure 3-11(b), the radiance in the NIR OLEDs with different doping concentrations was also measured as a function of the applied bias voltage. The highest radiance of 6.4×10^5 mW sr^{-1} m^{-2} was obtained in the device based on the 3 wt% blend. It should be also emphasized that all devices show radiance values higher than

1.6×10^5 mW sr^{-1} m^{-2}. Such values are consistent with those obtained for TPA-BCm and are among the highest reported to date for NIR emitters.

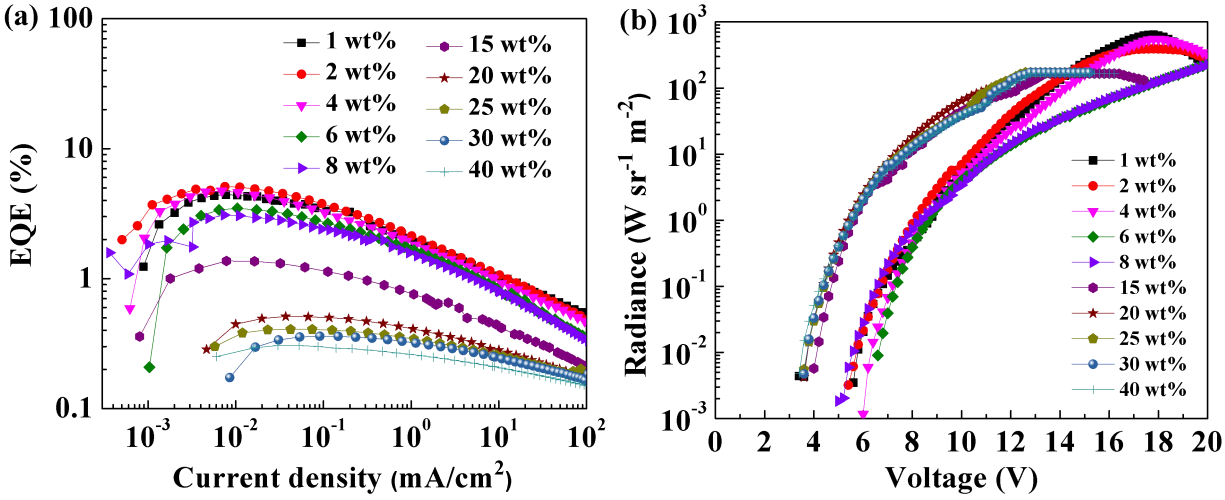

Figure 3-11. (a) EQE as a function of the current density. (b) Radiance as a function of the applied bias voltage measured for various doping concentrations.

Table 3-5. Summary of the EQE, maximum EL emission and turn-on voltage measured in CBP blends with different doping concentrations.

Doping concentration (wt%)	EQE_{max} (%)	λ_{max} (nm)	Turn-on voltage (V)
1	4.42	754	8.6
2	5.10	758	8.0
4	4.73	763	8.5
6	3.47	767	8.6
8	3.09	773	8.2
15	1.36	781	5.5
20	0.51	785	5.3
25	0.40	788	5.4
30	0.36	791	5.5
40	0.30	796	5.5

3-3-4. Amplified spontaneous emission characteristics

NIR ASE and lasing above 800 nm in organic solid-state thin films have been rarely demonstrated so far and were only achieved using insulating polymer hosts doped with commercially available NIR laser dyes [40-42]. In this chapter, I aimed at evaluating the ASE properties of the dimeric curcuminoid derivative in CBP blend films. Figure 3-12(a) shows the emission spectra measured for several excitation densities from the edge of a 120 nm thick film based on the 2 wt% DTPA-BC:CBP blend. While the spectra are identical to the steady-state PL spectrum at low pumping intensity, a line narrowing is observed when increasing the pumping intensity above the ASE threshold [43]. Noticeably, the FWHM decreases from 122 to 16.4 nm as the excitation density is increased from 0.8 to 21 $\mu J/cm^2$. To evaluate the threshold value, the output intensity is plotted against the pumping intensity in Figure 3-12(b). The observed change of slope leads to the determination of an ASE threshold value around 7.5 $\mu J/cm^2$. Similar measurements were carried out in the other CBP blends with various doping concentrations. The ASE peaks observed in these different blends are shown in Figure 3-12(c). In perfect agreement with the behavior of the PL spectrum, the ASE peak is found to gradually shift toward longer wavelength from 801 to 860 nm as the doping concentration increases from 2 to 40 wt%. The ASE threshold was also measured in the different CBP blends from the data showing the output intensity versus excitation density. The doping concentration dependence of the ASE threshold, PLQY and ASE wavelength are displayed in Figure 3-12(d) and Table 3-6 for DTPA-BC and these data are compared to those previously obtained with TPA-BCm. The decrease of the ASE threshold with the doping concentration is directly related to the reduction of the concentration PL quenching. While the lowest threshold was obtained for the 2 wt% blend (7.5 $\mu J/cm^2$), it can be seen that the 40 wt% CBP blend shows an ASE threshold of 91.4 $\mu J/cm^2$ at the ASE wavelength of 860 nm. One could expect variations of the threshold due to

different confinement of the waveguide modes due to thickness and/or refractive index variations. For the higher doping concentration samples with the formation of aggregated species, as well as increase of polarity of the medium, with concentration, narrow spectra still can be observed. Here, this spectral narrowing is normally accompanied by a large enhancement of the output intensity and accounts for the presence of gain due to stimulated emission.

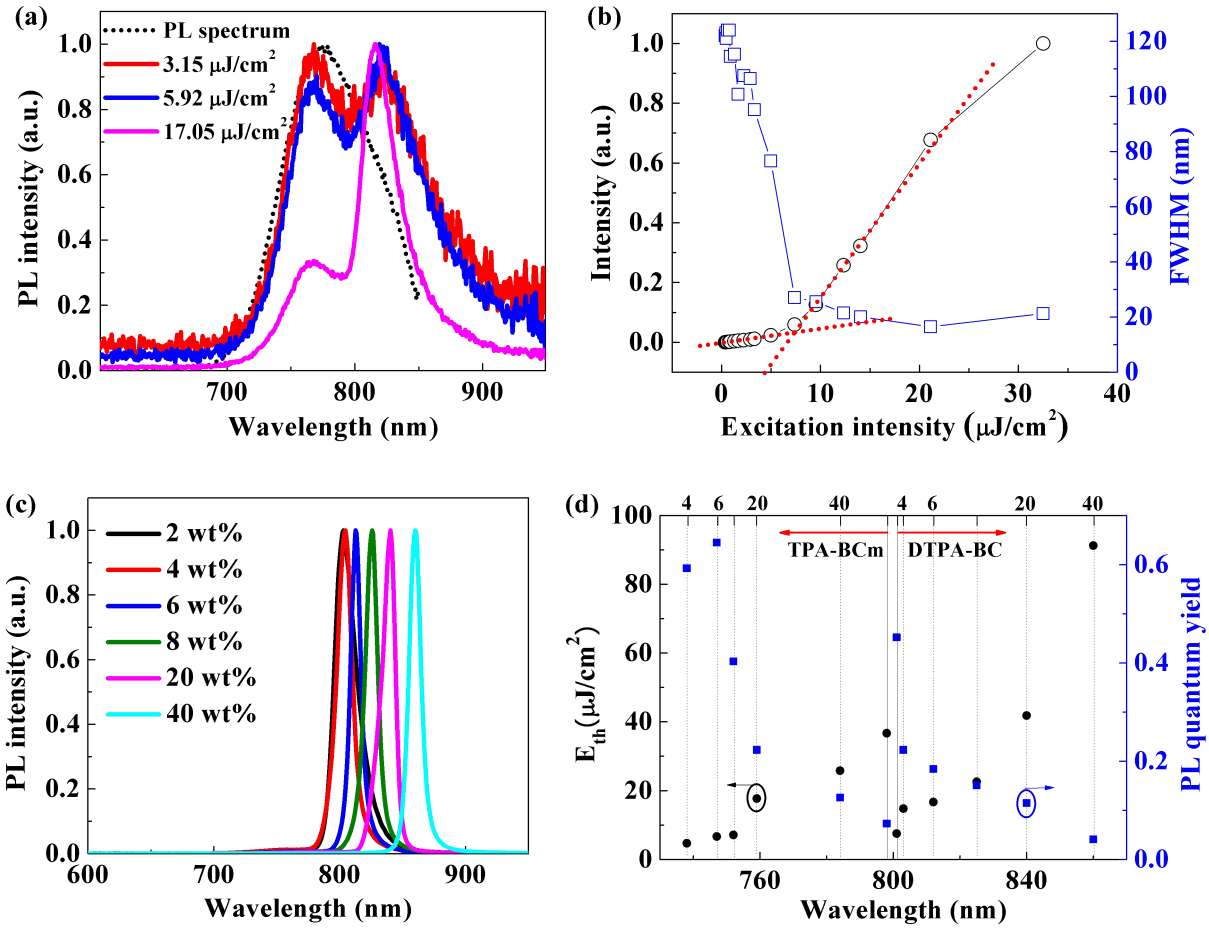

Figure 3-12. (a) Emission spectra for several excitation densities measured in a 120 nm thick film based on a 2 wt% CBP blend. (b) Output intensity and FWHM against the pumping intensity for a 2 wt% CBP blend. (c) ASE peaks observed in different blends. (d) Doping concentration dependence of the ASE threshold, PLQY and ASE wavelength for TPA-BCm and DTPA-BC.

Table 3-6. Summary of the ASE properties measured in DTPA-BC:CBP blend films with different doping concentrations.

DTPA-BC:CBP (wt%)	2	4	6	8	20	40
E_{th} (μJ/cm^2)	7.5	14.8	16.7	22.6	41.9	91.3
λ_{em} (nm)	801	804	812	825	840	860
PLQY	0.452	0.223	0.184	0.158	0.115	0.041

To my knowledge, the observation of ASE at wavelengths longer than 800 nm has not been reported so far in organic semiconducting thin films. Overall, by engineering the molecular architecture of the NIR emitters, one could vary the range of ASE wavelengths from 740 to 800 nm and 801 to 860 nm for TPA-BCm and DTPA-BC, respectively, while still keeping ASE thresholds lower than 100 μJ/cm^2. This study provides additional evidence that TADF borondifluoride curcuminoid derivatives are outstanding candidates for high performance NIR OLEDs and OSSLs.

3-4. Conclusion

The main objective of this work was to clarify whether NIR TADF EL and ASE from borondifluoride curcuminoid derivatives could be shifted toward longer wavelengths while keeping high efficiency by modifying their chemical structures. For this purpose, a novel dimeric borondifluoride curcuminoid dye was specifically designed and synthesized because of the good electron withdrawing properties of acetylacetone borondifluoride appended in *meso* position and excitonic coupling effects which can take place in such a molecular system. Steady-state and time-resolved PL measurements demonstrated that this dye exhibits highly efficient NIR TADF emission with a PLQY which can be as high as 45% in the doped thin film for a maximum emission wavelength of 760 nm. NIR TADF OLEDs with a maximum EQE of 5.1% were fabricated, which exceeds the performances typically obtained in devices based on conventional NIR fluorescent emitters. In addition, ASE with a maximum emission wavelength, which can be tuned between 801 and 860 nm, and a threshold as low as 7.5 $\mu J/cm^2$ was observed, providing additional evidence that borondifluoride curcuminoid derivatives are promising candidates for NIR OSSLs. Overall, this study demonstrates that high efficiency NIR EL and ASE from TADF curcuminoid derivatives can be effectively tuned over a broad spectral range by chemical modification.

3-5. References

[1] H. Xiang, J. Cheng, X. Ma, X. Zhou, and J. J. Chruma, *Chem. Soc. Rev*., **2013**, 42, 6128.

[2] Z. Guo, S. Park, J. Yoon, and I. Shin, *Chem. Soc. Rev.*, **2014**, 43, 16.

[3] G. Tregnago, T. T. Steckler, O. Fenwick, M. R. Andersson, and F. Cacialli, *J. Mater. Chem. C*, **2015**, 3, 2792.

[4] R. Yang, R. Tian, J. Yan, Y. Zhang, J. Yang, Q. Hou, W. Yang, C. Zhang, and Y. Cao, *Macromolecules*, **2005**, 38, 244.

[5] S. Wang, X. Yan, Z. Cheng, H. Zhang, Y. Liu, and Y. Wang, *Angew. Chem. Int. Ed.*, **2015**, 54, 13068.

[6] G. Qian, Z. Zhong, M. Luo, D. Yu, Z. Zhang, Z. Y. Wang, and D. G. Ma, *Adv. Mater.*, **2009**, 21, 111.

[7] A. D'Aléo, H. M. Sazzad, D. H. Kim, E. Y. Choi, J. W. Wu, G. Canard, F. Fages, J. C. Ribierre, and C. Adachi, *Chem. Commun.*, **2017**, 53, 7003.

[8] A. Shahalizad, A. D'Aléo, C. Andraud, H. M. Sazzad, D. H. Kim, Y. Tsuchiya, J. C. Ribierre, J. M. Nunzi, and C. Adachi, *Org. Electron.*, **2017**, 44, 50.

[9] L. H. Slooff, A. Polman, F. Cacialli, R. H. Friend, G. A. Hebbink, F. C. J. M. van Veggel, and D. N. Reinhoudt, *Appl. Phys. Lett.*, **2001**, 78, 2122.

[10] K. Tuong Ly, R. W. Chen-Cheng, H. W. Lin, Y. J. Shiau, S. H. Liu, P. T. Chou, C. S. Tsao, Y. C. Huang, and Y. Chi, *Nat. Photon.*, **2017**, 11, 63.

[11] K. R. Graham, Y. Yang, J. R. Sommer, A. H. Shelton, K. S. Schanze, J. Xue, and J. R. Reynolds, *Chem. Mater.*, **2011**, 23, 5305.

[12] L. Huang, C. D. Park, T. Fleetham, and J. Li, *Appl. Phys. Lett.*, **2016**, 109, 233302.

[13] L. Sun, J. J. Choi, D. Stachnik, A. C. Bartnik, B. R. Hyun, G. G. Malliaras, T. Hanrath, and F. W. Wise, *Nat. Nano.*, **2012**, 7, 369.

[14] A. K. Bansal, F. Antolini, S. Zhang, L. Stroea, L. Ortolani, M. Lanzi, E. Serra, S. Allard, U. Scherf, and I. D. W. Samuel, *J. Phys. Chem. C*, **2016**, 120, 1871.

[15] J. Xue, C. Li, L. Xin, L. Duan, and J. Qiao, *Chem. Sci.*, **2016**, 7, 2888.

[16] B. S. Mashford, M. Stevenson, Z. Popovic, C. Hamilton, Z. Zhou, C. Breen, J. Steckel, V. Bulović, M. Bawendi, S. Coe-Sullivan, and P. T. Kazlas, *Nat. Photon.*, **2013**, 7, 407.

[17] Y. Shirasaki, G. J. Supran, M. G. Bawendi, and V. Bulović, *Nat. Photon.*, **2013**, 7, 13.

[18] K. Y. Cheng, R. Anthony, U. R. Kortshagen, and R. J. Holmes, *Nano Lett.*, **2011**, 11, 1952.

[19] H. Uoyama, K. Goushi, K. Shizu, H. Nomura, and C. Adachi, *Nature*, **2012**, 492, 234.

[20] H. Kaji, H. Suzuki, T. Fukushima, K. Shizu, K. Suzuki, S. Kubo, T. Komino, H. Oiwa, F. Suzuki, A. Wakamiya, Y. Murata, and C. Adachi, *Nat. Commun.*, **2015**, 6, 8476.

[21] C. Li, R. Duan, B. Liang, G. Han, S. Wang, K. Ye, Y. Liu, Y. Yi, and Y. Wang, *Angew. Chem. Int. Ed.*, **2017**, 56, 11525.

[22] R. Englman and J. Jortner, *Mol. Phys.*, **1970**, 18, 145.

[23] S. W. Thomas III, G. D. Joly, and T. M. Swager, *Chem. Rev.*, **2007**, 107, 1339.

[24] D. H. Kim, A. D'Aléo, X. K. Chen, A. S. D. Sandanayaka, D. D. Yao, L. Zhao, T. Komino, E. Zaborova, G. Canard, Y. Tsuchiya, E. Y. Choi, J. W. Wu, F. Fages, J. L. Brédas, J. C. Ribierre, and C. Adachi, *Nat. Photon.*, **2018**, 12, 98.

[25] A. S. D. Sandanayaka, K. Yoshida, M. Inoue, C. J. Qin, K. Goushi, J. C. Ribierre, T. Matsushima, and C. Adachi, *Adv. Opt. Mater.*, **2016**, 4, 834.

[26] A. S. D. Sandanayaka, T. Matsushima, F. Bencheikh, K. Yoshida, M. Inoue, T. Fujihara, K. Goushi, J. C. Ribierre, and C. Adachi, *Sci. Adv.*, **2017**, 3, e1602570.

[27] H. Nakanotani, T. Furukawa, and C. Adachi, *Adv. Opt. Mater.*, **2015**, 3, 1381.

[28] H. Nakanotani, T. Furukawa, T. Hosokai, T. Hatakeyama, and C. Adachi, *Adv. Opt. Mater.*, **2017**, 5, 1700051.

[29] C. A. Parker, *Photoluminescence of Solutions*. Elsevier Publishing: Amsterdam, 1969.

[30] J. R. Lakowicz, *Principles of Fluorescence Spectroscopy. 3rd ed.* Kluwer: New-York (NY), 2006.

[31] G. A. Crosby and J. N. Demas, *J. Phys. Chem.*, **1971**, 75, 991.

[32] N. C. Greenham, I. D. W. Samuel, G. R. Hayes, R. T. Phillips, Y. A. R. R. Kessener, S. C. Moratti, A. B. Holmes, and R. H. Friend, *Chem. Phys. Lett.*, **1995**, 241, 89.

[33] T. Körzdörfer and J. L. Brédas, *Acc. Chem. Res*., **2014**, 47, 3284.

[34] X. Gao, S. Bai, D. Fazzi, T. Niehaus, M. Barbatti, and W. Thiel, *J. Chem. Theory Comput.*, **2017**, 13, 515.

[35] H. T. Sun, Z. B. Hu, C. Zhong, X. K. Chen, Z. R. Sun, and J. L. Brédas, *J. Phys. Chem. Lett.*, **2017**, 8, 2393.

[36] J. Gibson, A. P. Monkman, and T. J. Penfold, *ChemPhysChem*, **2016**, 17, 2956.

[37] P. K. Samanta, D. W. Kim, V. Coropceanu, and J. L. Brédas, *J. Am. Chem. Soc.*, **2017**, 139, 4042.

[38] M. Rivoal, E. Zaborova, G. Canard, A. D'Aléo, and F. Fages, *New J. Chem.*, **2016**, 40, 1297.

[39] F. Archet, D. D. Yao, S. Chambon, M. Abbas, A. D'Aléo, G. Canard, M. Ponce-Vargas, E. Zaborova, B. Le Guennic, G. Wantz, and F. Fages, *ACS Energy Lett.*, **2017**, 2, 1303.

[40] T. Kobayashi, J. B. Savatier, G. Jordan, W. J. Blau, Y. Suzuki, and T. Kaino, *Appl. Phys. Lett.*, **2004**, 85, 185.

[41] K. Yamashita, T. Kuro, K. Oe, and H. Yanagi, *Appl. Phys. Lett.*, **2006**, 88, 241110.

[42] S. Yuyama, T. Nakajima, K. Yamashita, and K. Oe, *Appl. Phys. Lett.*, **2008**, 93, 023306.

[43] I. D. W. Samuel, E. B. Namdas, and G. A. Turnbull, *Nat. Photon.*, **2009**, 3, 546.

Chapter 4

Near-infrared continuous-wave lasing from a thermally-activated delayed fluorescent dye in organic semiconducting thin film

4-1. Introduction

CW lasing at room temperature was observed for the first time nearly 50 years ago using an inorganic AlAs-GaAs heterostructure [1]. Following this pioneering work, a wide range of CW inorganic semiconductor laser sources has been developed, which includes for instance silicon raman, gallium nitride and InGaN lasers. Noticeably, while the fabrication of these devices generally requires the use of expensive and complex microfabrication techniques, CW lasing from solution-processed inorganic colloidal quantum wells embedded in surface-emitting microcavities was reported a few years ago [2]. Organic semiconductors are another class of materials offering promising prospects for large-area, low-cost and flexible photonic devices. While these compounds have been successfully used in high performance OLEDs and optically-pumped OSSLs, there is still no report showing CW lasing in organic semiconducting thin films. However, the operation of CW lasing from organic semiconducting films is highly desirable for practical applications in the areas of spectroscopy tools, data/visible light communication, medical diagnostics for eye and cosmetic surgery, metal-cutting machines, bar code readers and sensing [3].

Optically-pumped OSSLs have been the subject of intensive studies during the last two decades, leading to an outstanding enhancement of their performances in terms of low threshold and stability. These improvements have been essentially due to the development of novel organic light-emitting semiconducting materials with high laser gain together with significant advances in the design and engineering of high quality factor (Q factor) resonator structures. Nevertheless, current optically-pumped OSSLs operate only in the pulsed regime, and most of previous reports used photo-excitation with pulse widths typically ranging between 100 fs and 10 ns. The two main obstacles for their long pulse operation are the thermal stability of the organic lasing media under intense CW laser irradiation and the additional losses due to

the accumulation of long-lived triplet excitons. When organic molecules in their S_1 states are optically pumped under such conditions, the molecules will have the probability to undergo ISC into the T_1 states, which are basically long-lived because of the spin-forbidden process between T_1 and S_0 states. Thus accumulation of long-lived triplet excitons at high excitation density, in most cases, results in an enhanced absorption loss at the lasing wavelength by the triplets and severe quenching of emission from singlet excitons due to the STA. This must be solved to achieve quasi-CW and CW operation because it causes the lasing threshold to a significant increase and, in the worst case, ruin the lasing completely [4]. In this context, an improved management of the triplet excitons is one key issue for the realization of OSSLs operating in the CW regime.

Recently, lasing under long pulse photo-excitation of 30 ms was achieved in a mixed-order organic semiconductor DFB laser using a blue conventional fluorescent emitter with high PLQY and no triplet absorption losses at the lasing wavelength [3]. The second approach is based on the use of triplet quenchers. The triplet quenchers were introduced into films to suppress the absorption losses and emission quenching. For instance, oxygen and cyclooctatetraene have been already successfully incorporated in organic lasing media to strongly reduce or even suppress the triplet related losses [5, 6]. An anthracene derivative was also used as triplet quencher in an OSSL, which could operate under pulse excitation of nearly 100 μs [7]. However, the requirements for triplet quenchers with a low triplet energy, a short triplet lifetime, and a large difference between the energies of the singlet and triplet states, make it very difficult to search suitable triplet quenchers that satisfy these conditions without impeding lasing [4, 6]. The third approach is based on the harvesting of triplet excitons for CW light amplification. While lasing from phosphorescent, TADF and TADF assisted fluorescent materials has been already observed under short pulse photo-excitation [8-10], there is however

still no evidence that triplet can positively contribute to light amplification under long pulse photo-excitation in an organic semiconductor gain medium.

In Chapters 2 and 3, different materials for deep-red and NIR emission were developed. Considering of stability and threshold, the promising molecule TPA-BCm should be capable for CW operation. The PLQY reached a maximum value of 70% in the 6 wt% TPA-BCm:CBP blend film and NIR TADF OLEDs with a maximum EQE of nearly 10% were achieved using TPA-BCm as an emitter. This dye exhibits both excellent TADF activity and low ASE threshold in thin doped films [11]. The remarkable photophysical properties of this compound were explained by its large oscillator strength and a nonadiabatic coupling effect between low lying excited-states and this is a key factor in achieving light amplification by stimulated emission in this TADF material.

The transient absorption spectrum of a 6 wt% TPA-BCm:CBP blend film showed an excited-state absorption between 400 nm and 600 nm, and a ground-state absorption bleaching from 600 nm to 700 nm at a delay time of 1 ms. Thus, TPA-BCm has a favorable window for light amplification around 600-750 nm, leading to large net gain for the light amplification. Thus, no additional triplet absorption losses take place even under long-pulse photo-excitation [11]. In fact, it has been established that the aromatic heterocycles having a BF_2 group provides reduced triplet related losses [12].

Here, in this Chapter, NIR organic semiconductor mixed-order DFB lasers were fabricated based on spin-coated thin films containing 6 wt% of TPA-BCm doped into CBP host. The lasing properties of these devices were examined as a function of the photo-excitation pulse duration ranging from 800 ps to several minutes. The clear observation of a lasing emission for pulse width longer than 100 s (which is 4 orders of magnitude longer than the current state-of-the-art) implies that triplet excitons in TADF systems can be harvested for CW lasing via RISC

process. Overall, this study demonstrates the first NIR TADF OSSL. Thus, organic light-emitting materials with resonator structures have reached a stage where CW lasing in organic semiconductor devices becomes a reasonable objective.

4-2. Experimental

Glass substrates covered with a thermally grown silicon dioxide layer with a thickness of 1 μm were cleaned by ultrasonication using alkali detergent, pure water, acetone, and isopropanol followed by ultraviolet ozone treatment. The silicon dioxide surfaces were treated with hexamethyldisilazane (HMDS) by spin-coating at 4000 rpm for 15 s and annealed at 120 ^{o}C for 120 s. A resist layer with a thickness of around 70 nm was spin-coated on the substrates at 4000 rpm for 30 s from a ZEP520A-7 solution (ZEON Co.) and baked at 180 ^{o}C for 240 s. Electron beam lithography was performed to draw grating patterns on the resist layer using a JBX-5500SC system (JEOL) with an optimized dose of 0.1 nC/cm^2. After the electron beam irradiation, the patterns were developed in a developer solution (ZED-N50, ZEON Co.) at room temperature. The patterned resist layer was used as an etching mask while the substrate was plasma-etched with CHF_3 using an EIS-200ERT etching system (Elionix). To completely remove the resist layer from the substrate, the substrate was plasma-etched with O_2 using a FA-1EA etching system (SAMCO). The gratings formed on the silicon dioxide surfaces were observed with SEM (SU8000, Hitachi). To complete the laser devices, 6 wt% TPA-BCm:CBP blend films with a thickness of 200 nm were prepared on the gratings by spin-coating with the spin speed at 1000 rpm for 30 s. Finally, 0.05 ml of CYTOP (Asahi Glass Co. Ltd.) was directly spin-coated at 1000 rpm for 30 s onto the DFB laser devices followed by device sealing with a high thermal conductivity sapphire lid to seal the top of the laser devices, and dried in a vacuum overnight.

To characterize their lasing properties, the samples were optically pumped by a pulsed nitrogen laser (KEN-2020, Usho) and were focused on a 6×10^{-3} cm^2 area of the devices through lens and slit. The excitation wavelength, pulse width, and repetition rate were 337 nm, 0.8 ns, and 20 Hz, respectively. The excitation light was incident upon the devices at around

20° with respect to the normal to the device plane. The emitted light was collected normal to the device surface with an optical fiber connected to a multichannel spectrometer (PMA-50, Hamamatsu Photonics) and placed 3 cm away from the device. Excitation intensities were controlled using a set of neutral density filters.

To characterize the temperature dependence of ASE threshold, the samples in vacuum were photo-excited by a pulsed nitrogen laser (KEN-2020, Usho) and were focused into a stripe of dimension 0.06 cm^2 through lens and slit. The excitation wavelength, pulse width, and repetition rate were 337 nm, 0.8 ns, and 20 Hz, respectively. A set of neutral density filters were used to vary the energy of the excitation. The excitation beam was focused using cylindrical lens. The emission was detected from the edge of the organic film using an optical fiber connected to a charge-coupled device spectrometer (PMA-12, Hamamatsu Photonics). The temperature was controlled by using a cryostat (CRT-006-2000, Iwatani Industrial Gases). The measurements were done from 300 K down to 50 K, and then reversely from 50 K to 300K.

For the long pulse operation, the 6 wt% TPA-BCm:CBP blend film on DFB substrate was pulsed with a CW laser diode (OBIS LG, Coherent) to generate excitation light with an excitation wavelength of 355 nm. In these measurements, pulses were delivered using an acousto-optic modulator (Gooch & Housego) as pulse picker that was triggered with a pulse generator (WF 1974, NF Corporation). The excitation light was focused on a 1.04×10^{-5} cm^2 area of the devices through lens and slit, and the emitted light was collected using a streak camera (C7700, Hamamatsu Photonics) with a time resolution of 100 ps that was connected with a digital camera (C9300, Hamamatsu Photonics) and also collected normal to the device surface with an optical fiber connected to a multichannel spectrometer (PMA-50, Hamamatsu Photonics). The stability was checked using the same experimental setup but collected the emission intensity only with PMA-50.

The transient PL response of different pulses under excitation were also measured. The emission intensity was recorded using a photomultiplier tube (PMT) (C9525-02, Hamamatsu Photonics) and were monitored on a multichannel oscilloscope (MSO6104A, Agilent Technologies). The same irradiation and detection angles were used for this measurement as described earlier. The size of the excitation area was carefully checked by using a beam profiler (WinCamD-LCM, DataRay). The CW and lasing measurements were performed in a nitrogen atmosphere to prevent any degradation resulting from moisture and oxygen. The other measurements were performed in the air atmosphere. Third-harmonic-wave laser light with a wavelength of 355 nm and a FWHM of 5 ns from a Nd:YAG laser (Quanta-Ray GCR-130, Spectra-Physics) was used as pump light and pulsed white light from a Xe lamp was used as probe light for the transient triplet absorption measurement using a streak camera (C7700, Hamamatsu Photonics).

Regarding the optical simulation, the confinement factor (Γ) and the Q factor were calculated to design the resonant cavity. These two factors are extracted from the calculation of the eigenvalues of resonant cavity mode by solving Maxwell's equation using the finite element method in the Radio Frequency module of COMSOL 5.2a software. The computation domain is limited to one-unit domain consisting of a second-order grating enclosed by two first-order gratings. The Floquet periodic boundary conditions are applied for lateral boundaries and scattering boundary conditions are used for the top and bottom boundaries. The input parameters used for the optical simulation are the organic film thickness and the refractive indices of the layers. The CYTOP (n_{CYTOP} = 1.35) and the SiO_2 substrate (n_{SiO2} = 1.46) are considered to be semi-infinite layers. The refractive index of the 6 wt% TPA-BCm:CBP blend film, n_{eff}, was measured by using variable angle spectroscopic ellipsometry (VASE, J.A. Wollam, M-2000U) carried out at different angles from 45° to 75° by steps of 5°. The

ellipsometry data were then analyzed using an analytical software (J.A. Woollam, WVASE32) to determine refractive index of the film.

Transient 2D heat transfer simulation was performed using COMSOL 5.2a in order to probe the temperature distribution within the device. The governing partial differential equation for temperature distribution is expressed as eq. 4-1 [3]:

$$\rho C_{\mathrm{p}} \frac{\partial T}{\partial t} - k\left[\frac{\partial^2 T}{\partial r^2} + \frac{1}{r}\frac{\partial T}{\partial r} + \frac{\partial^2 T}{\partial z^2}\right] = Q(r,z,t), \qquad \text{(eq. 4-1)}$$

where ρ is the material density, C_{p} is the specific heat capacity, T is the temperature, t is the time, k is the thermal conductivity and Q is the laser heat source term. The laser pump beam has a Gaussian shape. Because of the circular symmetry of the laser beam, the heat transfer equation is solved in cylindrical coordinate. For a pulsed Gaussian laser beam, the heat source is written as eq. 4-2 [3]:

$$Q(r,z,t) = A\,\eta_{\mathrm{g}} \exp(-\beta(z - z_{\mathrm{g}}))\frac{2P}{\pi r_0^2}\exp(-\frac{2r^2}{r_0^2})H(t), \qquad \text{(eq. 4-2)}$$

where β is the absorption coefficient, A is the EML absorption of the pump beam calculated using Comsol $\{A(\lambda = 355\ \mathrm{nm}) = 8\%\}$, P is the incident pump power reaching the gain region, r and z are the spatial coordinate, r_0 is the $1/e^2$ radius of the pump laser beam (r_0 = 36.6 μm), r = 0 is center of the laser beam, z_{g} is z-coordinate of the interface between the gain region and the top layers, $H(t)$ is the rectangular pulse function with a pulse width, η_{g} is the fraction of the pump power absorbed in the gain region converted to heat in the absence of laser field given by eq. 4-3 [3]:

$$\eta_{\mathrm{g}} = 1 - \Phi_{\mathrm{PL}}\,\lambda_{\mathrm{pump}}/\lambda_{\mathrm{laser}}, \qquad \text{(eq. 4-3)}$$

where Φ_{PL}, λ_{pump}, and λ_{laser} are the PLQY, pump laser wavelength, and lasing wavelength from emitter, respectively. Concerning the boundary conditions, in the radial direction, symmetry

boundary conditions are used at the axis of rotation. Thermal insulation boundary conditions are applied at the bottom, top and edge surfaces (air convection is neglected). The radius of the device is set to 2.5 mm. The power P is 12.5 mW.

4-3. Results and discussion

4-3-1. Measurement of loss and gain coefficient

The photophysical properties of TPA-BCm have been previously examined in details in solution, neat film and CBP blends [11]. The investigation of the photophysical properties of the CBP blends indicated that the most efficient TADF, EL and ASE properties were obtained with the 6 wt% doping concentration. In this specific CBP blend, the PLQY and the ASE threshold were reported to be around 70% and 7 μJ/cm^2, respectively.

To investigate the optical net gain of the material, the variable stripe length (VSL) technique is a widespread technique commonly used to retrieve gain in materials under the form of thin films where a confined mode can propagate in-plane [13]. The technique consists of pumping the material from the top by a pump beam whose shape is tailored under the form of a thin stripe of variable length as shown in Figure 4-1(a), and the net gain can be derived by eq. 4-4 [14]:

$$I(\lambda) = \frac{A(\lambda) I_{\mathrm{p}}}{g(\lambda)} (e^{g(\lambda) l} - 1), \qquad \text{(eq. 4-4)}$$

where $I(\lambda)$ is the output intensity, $A(\lambda)$ is a constant related to the cross-section for spontaneous emission, I_{p} is the pump intensity, $g(\lambda)$ is the net gain coefficient (gain minus the loss), and l is the length of the pumped stripe.

The optical net gain was determined to be 23 cm^{-1} at an excitation energy of 88 μJ/cm^2, and as large as 34 cm^{-1} for an excitation density of 575 μJ/cm^2 as shown in Figure 4-1(b). Such a value is, for example, comparable with those previously obtained in bisfluorene-cored dendrimer films [15].

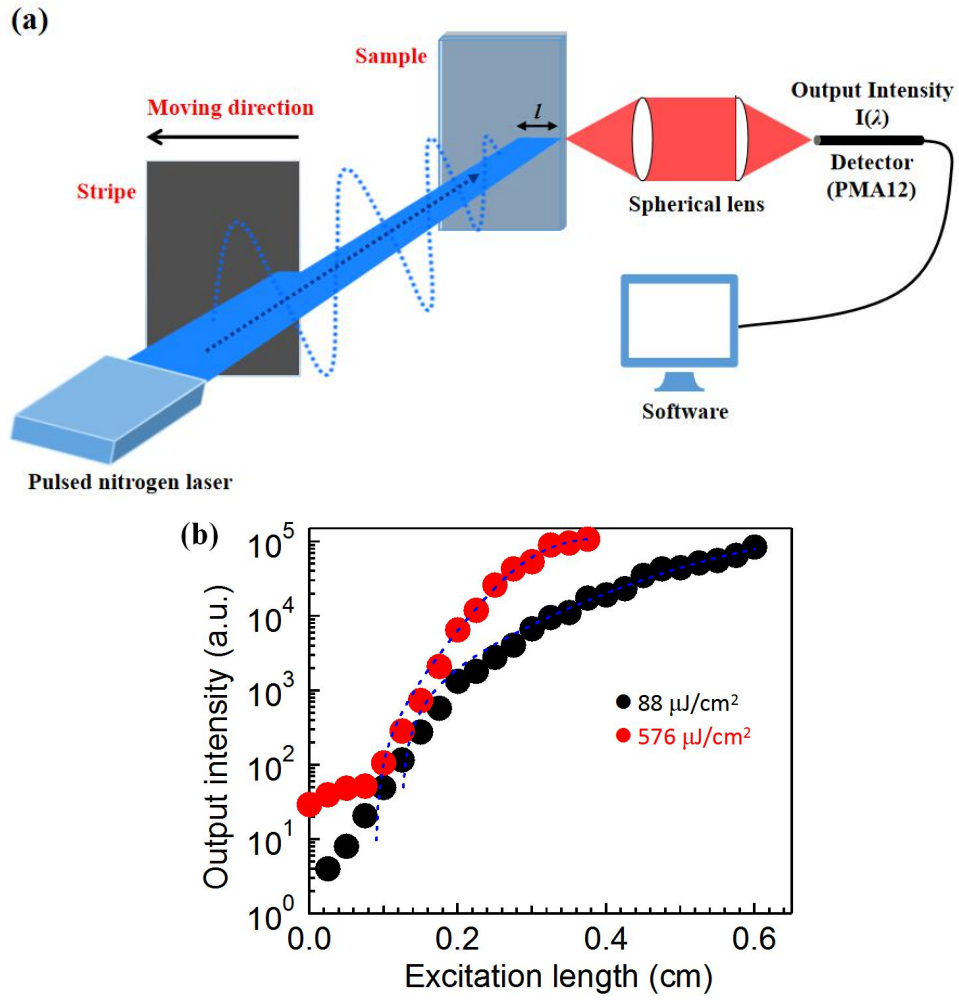

Figure 4-1. (a) Representation of VSL method. (b) The dependence of the emission intensity on the excitation length at the two different pump intensities. The dash lines fits to the data using eq. 4-4. The net gain of the waveguide can be determined from the fits.

In addition, the loss characteristics of the 6 wt% TPA-BCm:CBP blend film were also investigated by measuring the ASE intensity as a function of the distance between the pump stripe and the edge of the organic thin films as shown in Figure 4-2(a). The loss coefficient can be derived by eq. 4-5 [14]:

$$I = I_0 \exp(-\alpha x), \qquad \text{(eq. 4-5)}$$

where I_0 is the emission from the end of the pumped region, and is constant. x is the length of the unpumped region between the end of the pump stripe and the edge of the sample. α is the loss coefficient.

The results obtained in the 6 wt% TPA-BCm:CBP blend film are shown in Figure 4-2(b). From these measurements, I found a loss coefficient α of 6.5 cm^{-1}. Such a low value is close to the loss coefficient of other high-efficiency organic semiconducting lasing materials such as 4,4'-bis[(N-carbazole)-styryl]biphenyl (BSBCz) (α = 3 cm^{-1}) [3], poly(9,9-dioctylfluorene) (α = 3.5 cm^{-1}) [13], bisfluorene dendrimers (α = 4-10 cm^{-1}) [15-17], and octafluorene (α = 5.1 cm^{-1}) [18]. This result is due to the negligible self-absorption of the films at the ASE wavelength and the good quality of the waveguiding films. This latter aspect is supported by the atomic force microscope (AFM) image in Figure 4-2(c) showing the good flatness and low roughness of the CBP blend films. Based on these photophysical data, the 6 wt% TPA-BCm:CBP blend film was decided to be as laser gain medium in the present study.

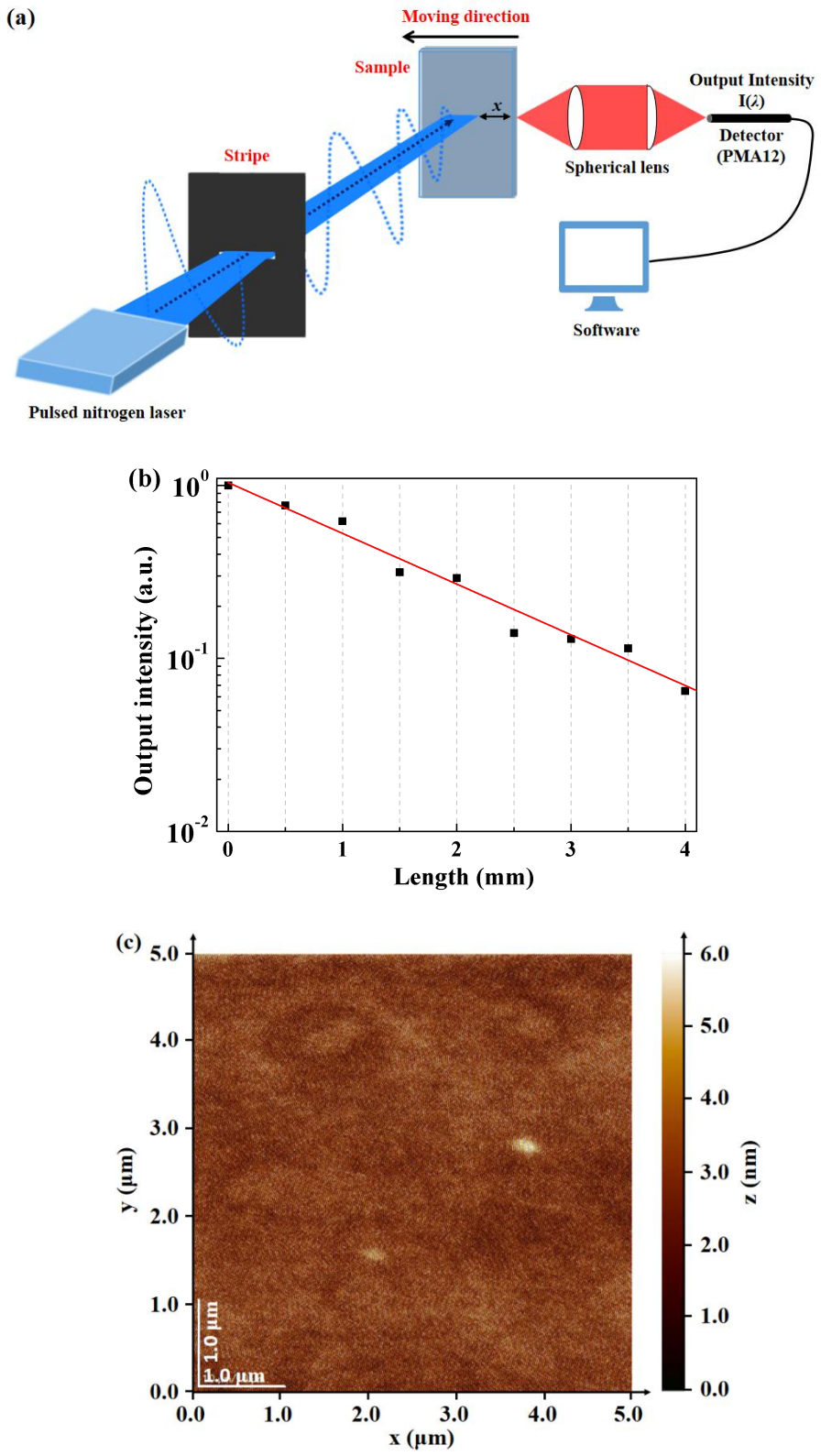

Figure 4-2. (a) Representation of loss measurement system. (b) ASE intensity plotted against the distance between the pump stripe and the edge of a 6 wt% TPA-BCm:CBP blend film. Red solid line corresponds to the fit obtained from a single exponential decay of eq. 4-5 to determine the loss coefficient. (c) AFM image of the surface of a 6 wt% TPA-BCm:CBP blend film. The root-mean-square roughness of the film is found to be around 1.3 nm.

4-3-2. Singlet-triplet exciton annihilation

Figures 4-3(a) and (b) display the transient decay, the representative ASE spectrum, stimulated emission cross-section spectrum, and transient absorption spectrum at a delay time of 1 ms of the 6 wt% TPA-BCm:CBP blend film, respectively. From these spectra, one can see that the stimulated emission cross-section is significantly larger than 2.2×10^{-16} cm^2 at the wavelength from 670 nm to 800 nm. This indicates that the curcuminoid derivatives are expected to show excellent ASE behavior and the lasing properties. More importantly, the transient absorption spectrum does not show any significant triplet absorption band in the spectral region where light amplification takes place and is a very important aspect for achieving CW lasing without the need of using triplet quenchers. To gain further insights into the potential triplet related losses, which could occur in the organic TADF laser medium at high excitation density, I then spin-coated a 6 wt% TPA-BCm:CBP blend film on a bare SiO_2 substrate and monitored the temporal evolution of PL intensity generated during the irradiation of the film by pulsed excitation light with a pulse width of 1 ms.

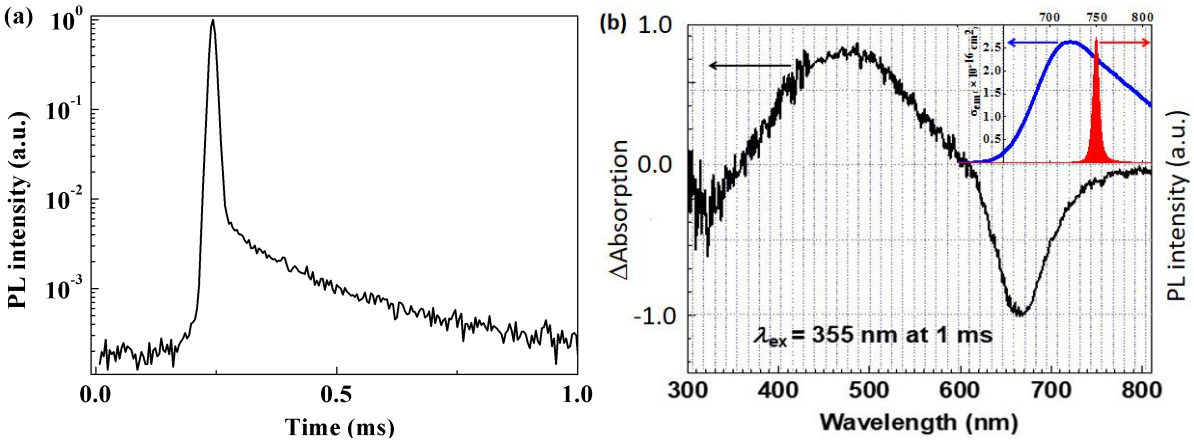

Figure 4-3. (a) Transient decay and (b) Transient absorption spectrum (black line) at a delay time of 1 ms of a 6 wt% TPA-BCm:CBP blend film with the stimulated emission cross-section spectrum (blue line) and the ASE spectrum (red area) measured from the 6 wt% TPA-BCm:CBP blend film above E_{th}.

Figure 4-4 displays the results obtained at the pumping energy of 1176 W cm^{-2} with the photo-excitation pulse duration increased to 1 ms. The transient curve shows that the emission intensity decreases in the time region I. While the stabilization of the PL intensity should occur within the transient lifetime of the delayed emission, it stabilized within ~0.1 ms. Interestingly, a gradual increase of the PL intensity was then observed after the initial rapid decrease as shown in the time region II. It would be probable that the PL intensities gradually increased because populated triplet excitons may annihilated each other, generating extra singlet excitons via TTA. These results suggest that while quenching of the emission by STA occurs in the 6 wt% TPA-BCm:CBP blend film, lasing under long pulse photo-excitation is enabled and efficient RISC and also TTA may contribute for the lasing.

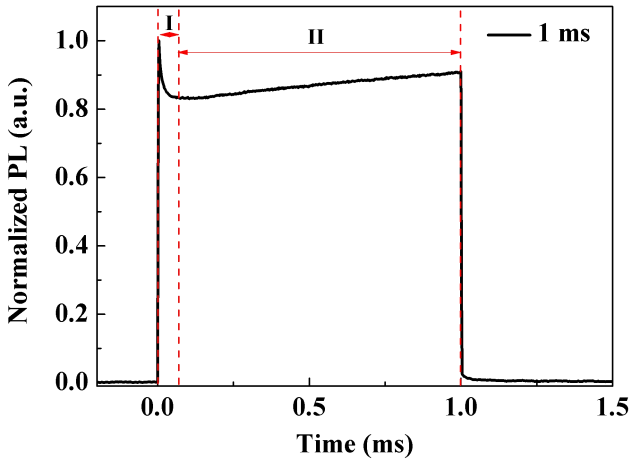

Figure 4-4. Transient PL response of the 6 wt% TPA-BCm:CBP blend film under pulse width at 1 ms with the pump intensity at 1176 W cm^{-2}.

4-3-3. Cooling effect on threshold

To investigate more about the triplet contribution, I studied the cooling effect on the threshold. For TADF molecules, there are a specific radiative transition of the excitons from the S_1 state via ISC and RISC, i.e., the delayed emission with a longer lifetime than the prompt fluorescence. The upconversion process from T_1 to S_1 generates the final emissive singlet excitons. The energy level of the S_1 state is usually located above that of the T_1 state; therefore, the RISC process in the TADF molecules becomes an endothermal process, which makes it thermally activated with stronger emission at high temperature. However, in lower temperature, the TADF process should be suppressed and the contribution from triplet excitons by the RISC process is also forbidden [19]. Thus, I tried to measure the temperature dependence of the ASE threshold by connecting the low-temperature system to ASE measurement to check the contribution from triplet excitons by the RISC process.

Data in different temperatures are shown in Figure 4-5. Interestingly, I found the threshold was almost similar at different temperatures as shown in Figure 4-6, which means that the upconversion contribution from the triplet excitons is small in the 6 wt% TPA-BCm:CBP blend film under the short pulse width (0.8 ns).

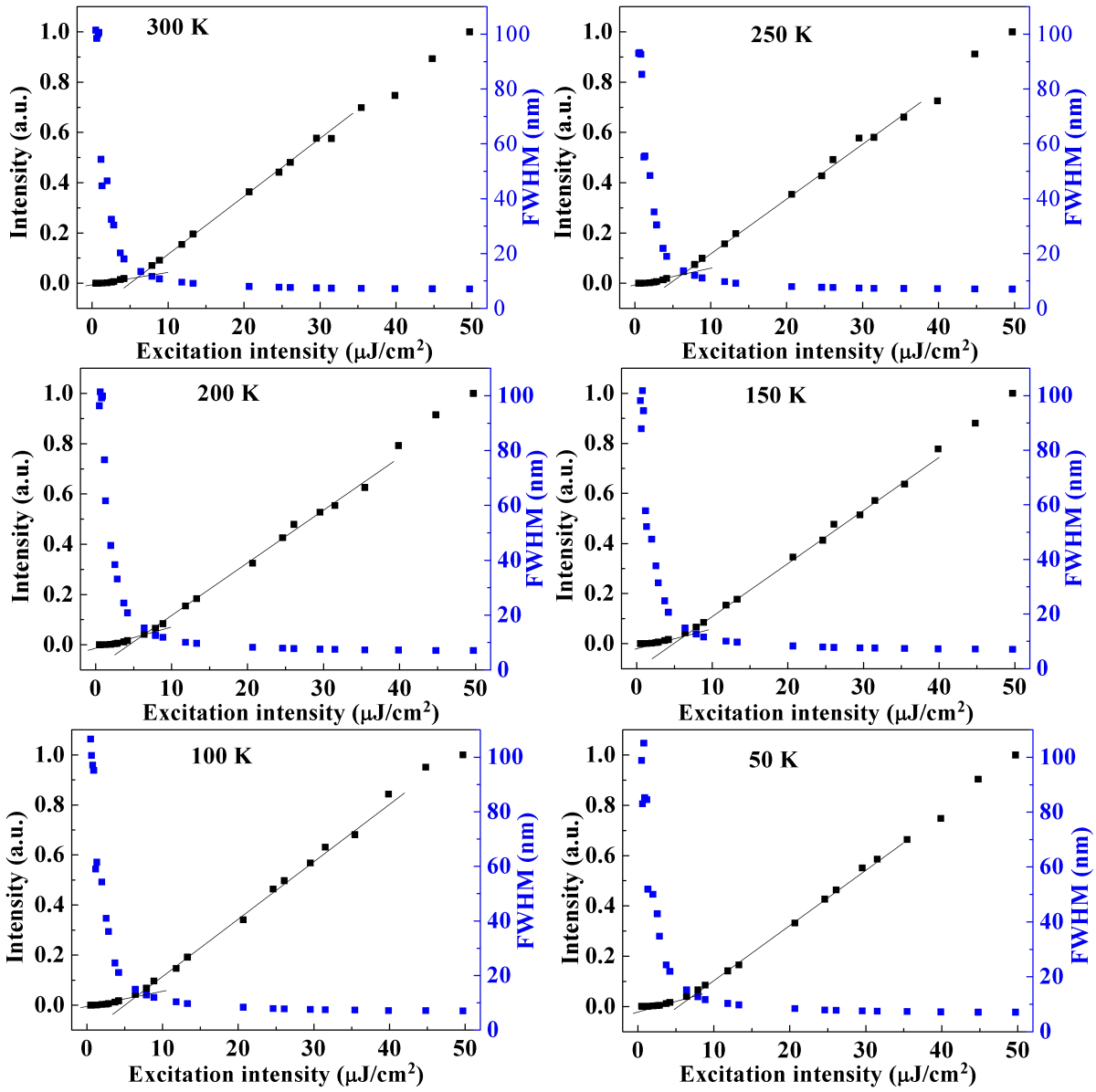

Figure 4-5. Plots of emission intensity and FWHM as a function of excitation light intensity for 6 wt% TPA-BCm:CBP blend films under different temperatures.

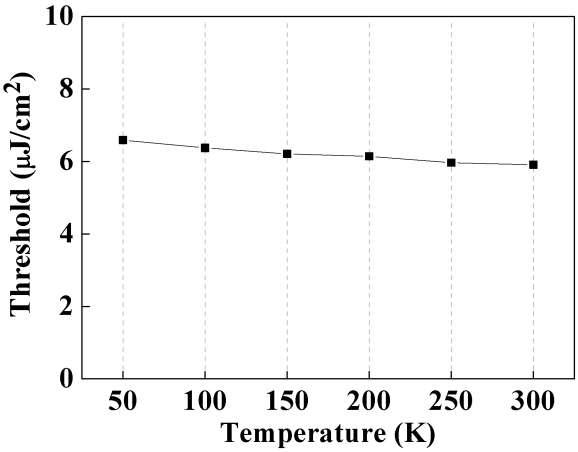

Figure 4-6. Temperature dependence of ASE threshold for a 6 wt% TPA-BCm:CBP blend film.

4-3-4. Lasing characteristics

In a DFB structure, a laser oscillation takes place when the following Bragg condition is satisfied: $\lambda = 2n_{eff}\Lambda/n$. When considering a mixed-order mode, the grating period is optimized to be $\Lambda_1 = 230$ nm (n = 1) and $\Lambda_2 = 460$ nm (n = 2) taking into account the optical properties of the 6 wt% TPA-BCm:CBP blend film [11]. A grating with $\Lambda_2 = 460$ nm provides surface-emitting lasing in a direction normal to the substrate plane. The CBP blend films with a thickness of 200 nm were spin-coated from a chloroform solution on top of the mixed-order DFB gratings. The fabrication method as shown in Figure 4-8 and architecture of the mixed-order DFB gratings are similar to those previously used to achieve long pulse operation of 30 ms in optically-pumped laser devices based on BSBCz [3]. The gratings composed of second-order Bragg scattering regions surrounded by first-order scattering regions were prepared onto silicon dioxide over 5 × 5 mm^2 area using electron beam lithography and reactive ion etching. As schematically represented in Figure 4-7, following the deposition of the light-emitting organic thin film onto the SiO_2 DFB grating, a 2 μm thick CYTOP polymer thin film was then directly spin-coated on top the structure and then covered by a sapphire lid (with a thermal conductivity of 25 W m^{-1} K^{-1} at 300 K). Such an encapsulation has been previously shown to be extremely beneficial for improving the lifetime of OSSLs under high intensity photo-excitation [3].

The lasing properties of the encapsulated organic semiconductor mixed-order DFB devices were first examined under pulsed optical pumping using a nitrogen-gas laser delivering 0.8 ns pulses at a repetition rate of 20 Hz. The excitation wavelength was 337 nm. In the case of the CBP blend films, the excitation light was mainly absorbed by the CBP host, but the large spectral overlap between the CBP emission and the TPA-BCm absorption guaranteed an efficient FRET from the host to the guest molecules to achieve a high PLQY of about 70%.

This was confirmed by the low ASE threshold of about 7 μJ/cm^2 and negligible emission from CBP even under high excitation [11].

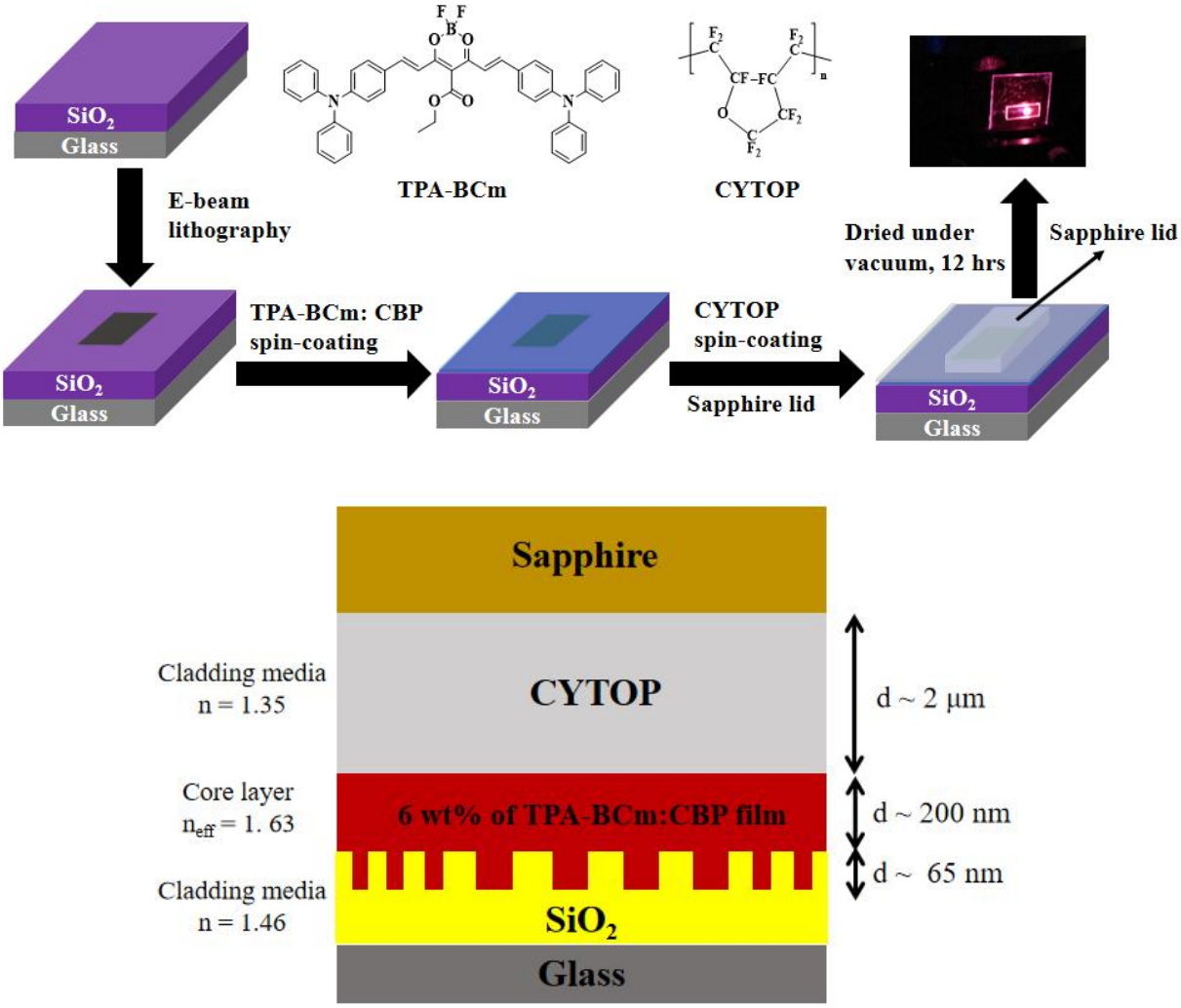

Figure 4-7. Top: schematic representation of the method used to fabricate the organic DFB lasers. The different successive steps involve the fabrication of a DFB resonator structure by e-beam lithography, thermal evaporation of the organic semiconductor thin film, and spin-coating a CYTOP polymer film followed by device sealing with a high thermal conductivity sapphire lid. Bottom: cross-sectional view of the mixed-order DFB.

Figures 4-8(a) and (b) display the emission spectra measured from the laser device at different excitation intensities. The spectra at low excitation densities display a Bragg dip at 751 nm, corresponding to the optical stopband of the mixed-order DFB grating and indicating

that the grating works well for outcoupling light from the waveguide film as surface emission. As the excitation density is gradually increased above 1 μJ/cm^2, a narrow emission peak is observed at the wavelength of 751 nm, with an intensity increasing faster than the spontaneous emission background as shown in Figure 4-8(c). Noticeably, this narrow DFB laser single mode emission with a FWHM of around 1.4 nm takes place at the long-wavelength edge of the Bragg dip. The output emission intensity is plotted as a function of the excitation density in Figure 4-8(d). The observation of a clear change of slope is a signature of a lasing threshold, which is found to be around 1.3 μJ/cm^2 (366 W cm^{-2}). As expected, this lasing threshold value is lower than that of the ASE threshold. While such a lasing threshold is higher than the lowest values reported in blue-emitting organic DFB lasers, I would like to emphasize that, to the best of my knowledge, this is the first demonstration of NIR lasing from an organic semiconductor laser and the threshold value is significantly lower than those previously reported in NIR OSSLs based on an insulating polymeric host doped with commercially available laser dyes. It should also be emphasized that the upconversion rates via RISC for the NIR TADF dye used in the present study are in the order of tenths and hundredths of μs. This implies that the 800 ps photo-excitation pulses used to optically pump the DFB laser are too short to obtain a significant contribution of the triplets for lasing action, as I discussed in previous part. In other words, the use of longer excitation pulses (with a time width at least comparable to the inverse of the k_{RISC}) is necessary to achieve an upconversion from triplet to singlet via RISC in the organic semiconductor DFB laser.

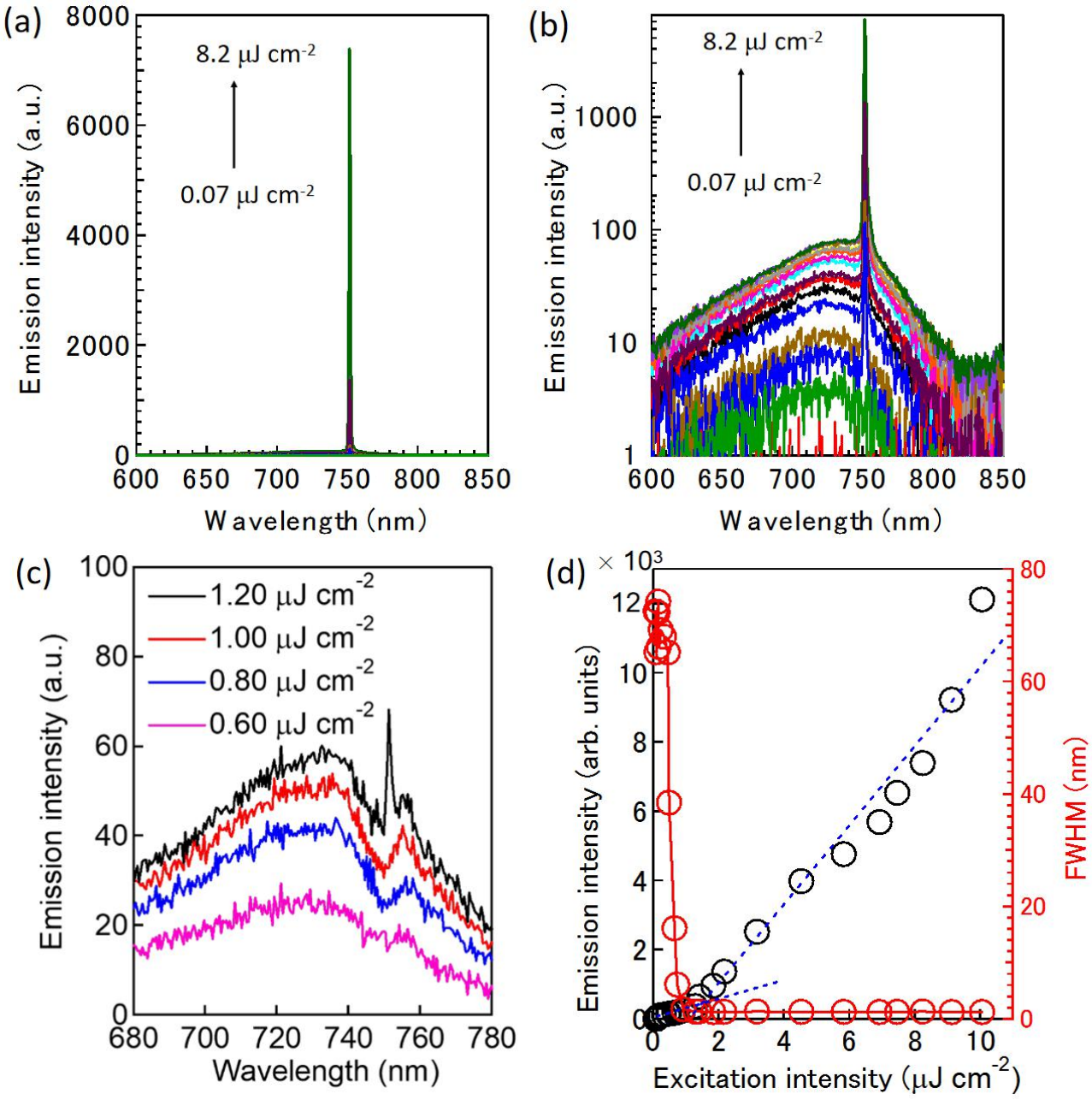

Figure 4-8. (a) Emission spectra of representative organic mixed-order DFB lasers based on 6 wt% TPA-BCm:CBP film and (b) Spectra in log scale. (c) Films at various pumping intensities below and above the lasing threshold and show the emission spectra near the lasing threshold. (d) Emission output intensity and FWHM as a function of the pumping intensity. In these experiments, the organic films were covered by spin-coated CYTOP films and a sapphire lid. The optical pumping source was a nitrogen laser emitting 0.8-ns-wide pulse excitation at a repetition rate of 20 Hz and a wavelength of 337 nm. The emission from the laser devices was collected in the direction normal to the substrate plane.

4-3-5. Toward the continuous-wave operation

Although no significant positive contribution of triplet excitons for ASE action can be expected with the pulsed photo-excitation used in previous section. However, the no triplet excited-state absorption at ASE and lasing wavelengths in this compound and good lasing characteristics of the DFB devices support me that TPA-BCm is an outstanding candidate for OSSLs operating under long pulse photo-excitation, implying that there are no additional triplet absorption losses taking place under long pulsed photo-excitation.

The performances of the organic semiconductor NIR DFB lasers were then examined for different long pulse duration varying from 0.1 ms to 500 s. For this experiment, the devices were optically-pumped by a CW laser diode emitting at 355 nm with a maximum power of 20 mW and the output was detected in the direction normal to the substrate. Figure 4-9(a) shows the emission spectra of the organic NIR DFB laser measured at various excitation densities for a pulse duration of 10 s. These data demonstrate that the NIR organic DFB laser works properly above the threshold, without any significant changes observed in terms of lasing emission wavelength and with an outstanding and unprecedented stability under such a long pulse operation. The output laser intensity as well as the FWHM of the emission spectrum were also measured as a function of the excitation density for the pulse duration of 10 s as shown in Figure 4-9(b). The abrupt changes of the output intensity lead to the determination of a lasing threshold of 630 W cm^{-2}. Under such optical pumping conditions, it can also be seen that the spectral linewidth of the laser emission is as low as 1.3 nm for an excitation density of 1400 W cm^{-2}, which is comparable to the values found using the 800 ps long pulse photo-excitation.

To gain further insights, similar measurements were carried out for various pulse duration and the results are shown in Figures 4-10(a)-(h). The influence of the pulse duration on the lasing threshold is also summarized in Figure 4-10(i). These results show that the lasing

threshold does not significantly change for excitation pulse width as long as 10 s. As the pulse duration is further increased up to 100 s, the emission spectrum of the organic DFB laser is not strongly modified but the lasing threshold gradually increases to reach a value of 940 W cm^{-2}. For longer pulse duration, the emission spectrum of the laser is dominated by the spontaneous emission and the accurate determination of the lasing threshold becomes difficult with our experimental setup. Nevertheless, it is worth noting that a lasing peak can still be observed for a pulse duration of 500 s when the excitation density is higher than 1400 W cm^{-2}. It should be mentioned that these results are fully consistent with those obtained using a streak camera as shown in Figures 4-11(a)-(e). Noticeably, the streak camera images provide evidence that the lasing wavelength do not significantly change during the lasing period as shown in Figure 4-11(f). It is worth noting that wavelengths shifts have been seen in liquid dye lasers and have been explained by a competition between triplet absorption and gain spectra [7]. The absence of such a lasing wavelength shift in my devices seems to be in agreement with the negligible triplet absorption in the spectral range where gain takes place.

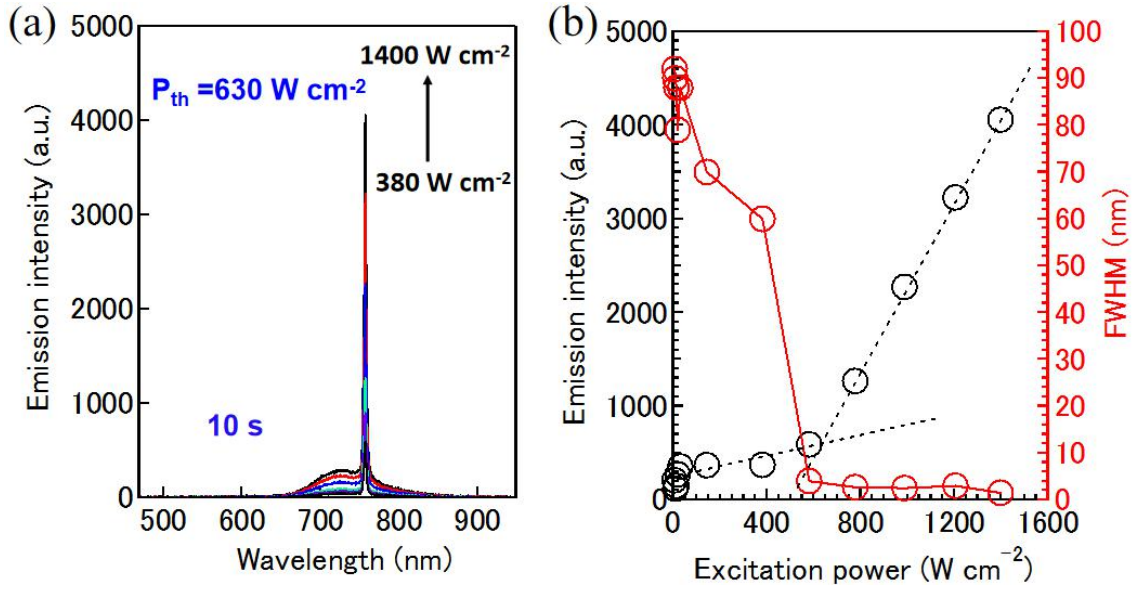

Figure 4-9. (a) Emission spectra and (b) laser output intensity and FWHM of an encapsulated mixed-order blend device as a function of the pumping intensities for pulse excitation widths of 10 s.

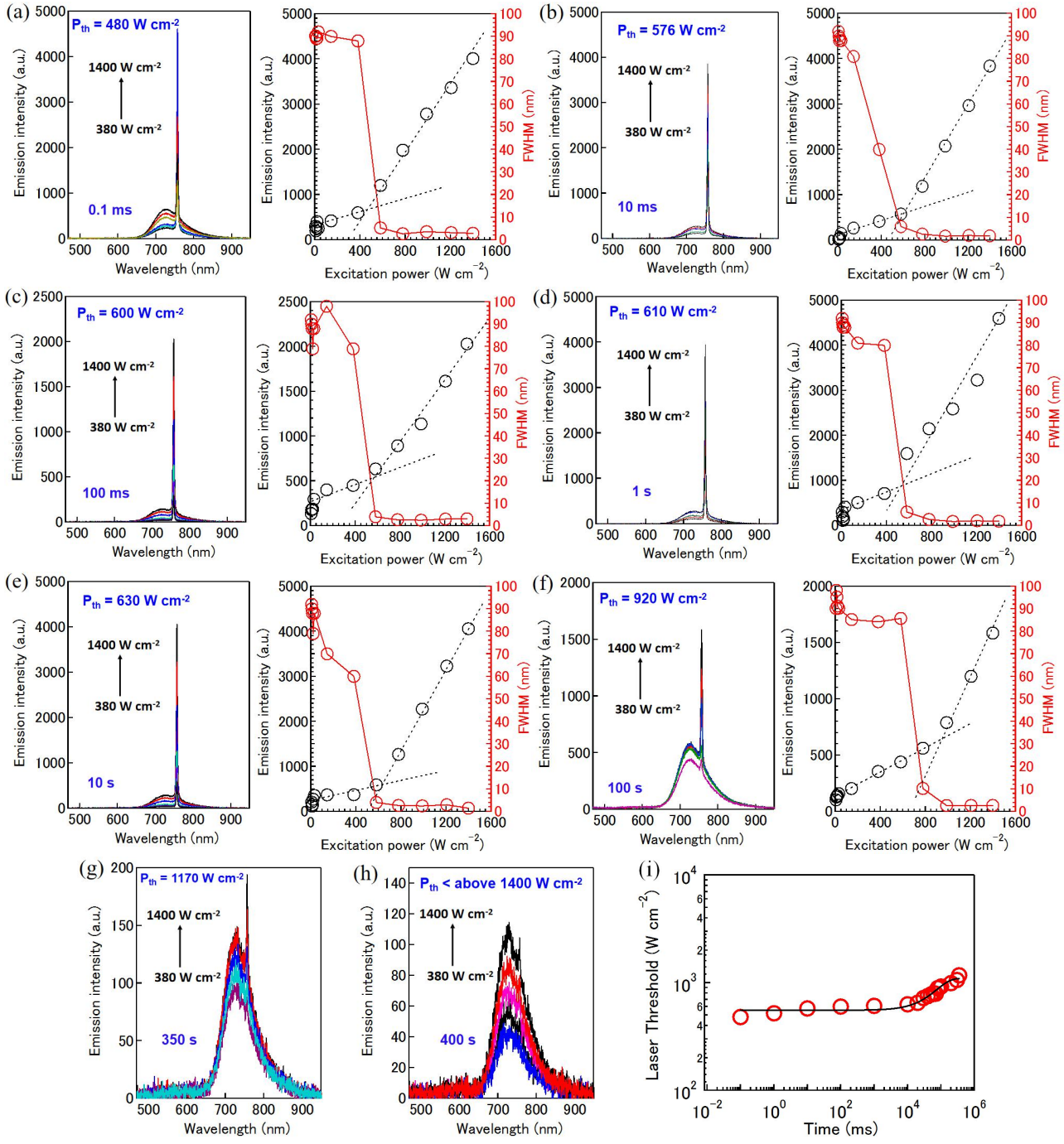

Figure 4-10. Emission spectra and laser output intensity and FWHM of an encapsulated mixed-order blend device as a function of the pumping intensities for pulse excitation widths of (a) 0.1 ms (b) 10 ms (c) 100 ms (d) 1 s (e) 10 s (f) 100 s (g) 350 s and (h) 400 s. (i) Lasing threshold as a function of excitation duration.

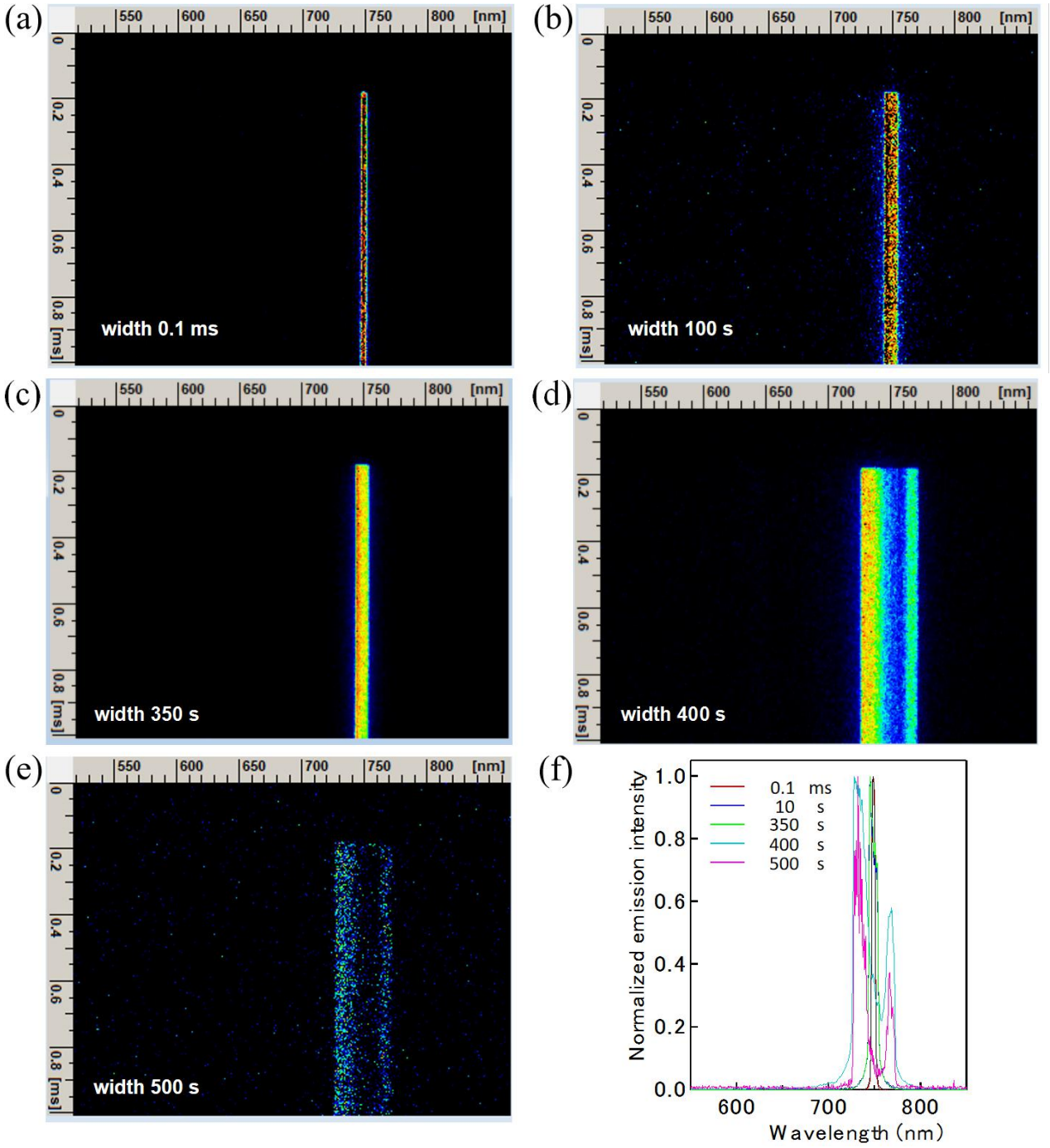

Figure 4-11. Streak camera images showing laser emission integrated over 100 pulses from an encapsulated mixed-order DFB device using a 6 wt% TPA-BCm:CBP film as gain medium and optically pumped by pulses of (a) 0.1 ms (b) 100 s (c) 350 s (d) 400 s and (e) 500 s under 1300 W cm^{-2}. (f) Emission spectra with changing pulse width.

4-3-6. Stability characteristics and thermal effect

In order to characterize the stability of the lasing output from the DFB lasers, the devices were optically pumped by a number of successive incident photo-excitation pulses with various time widths and with an excitation density of 1176 W cm^{-2}. I monitored the temporal evolution of the output intensity from the DFB laser for 4000 s. As shown in Figure 4-12, the emission intensity decreased with time and this decrease becomes faster as the incident pulse width was increased. For instance, the time period associated with a reduction of 50% from the initial value of the output intensity is around 1000 s for a photo-excitation single pulse duration of 50 μs. This time period gradually decreased to reach a value of about 80 s as the photo-excitation single pulse duration increases to 10 s.

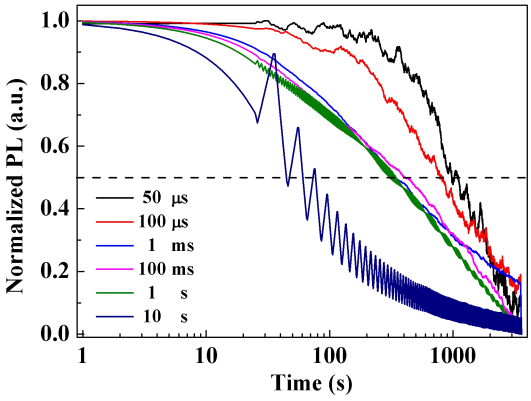

Figure 4-12. Temporal evolution of the laser output intensity under different pulse widths.

To gain further insights, I carried out some simulations to determine the temperature increment caused in the device by an intense CW irradiation, using the same method reported [17]. Table 4-1 and Figure 4-13 present the thermal and physical parameters used in the simulations taken from COMSOL database and schematic of the geometry, respectively. For the EML layer, I chose the same thermal parameters for organic materials as reported [20]. After absorption of the pump laser energy, the EML acts as a heat source. The generated heat is transferred by conduction towards the top and bottom layers. Figure 4-14 shows the

temperature rise as a function of time in the EML for different pump pulse width of 10 µs, 100 µs, 1 ms, 10 ms, 10 s, 350 s (5.8 min), 400 s (6.6 min) and 500 s (8.3 min). Figure 4-15 shows the maximum temperature rise at the end of each pump pulse in the EML. For pulses width less than 10 s, the maximum temperature rise is less than 2.5 ℃ and tends to saturate after 5 pulses. For pulses width above 5 min, the maximum temperature rise approach only 5 ℃ and also tends to saturate after 5 pulses. I concluded that the temperature rise is not expected to significantly effect the degradation of organic gain medium. Importantly, these decreases in emission output intensity with time were found to be irreversible, which is presumably due to a degradation of organic gain medium. Much more works are ongoing to clarify the degradation.

Table 4-1. Thermal and physical parameters of the materials used in the simulations.

Layer name	k (W K^{-1} m^{-1})	C_p (J kg^{-1} K^{-1})	ρ (kg m^{-3})	β (m^{-1}) at 355 nm	D^* (µm)
Sapphire	27	900	3900	0	759
CYTOP	0.12	861	2200	0	2
EML	0.2	1400	1200	7×10^5	0.110
SiO_2	1.38	703	2203	0	0.150
Glass	1.4	730	2210	0	717

D*: Layer thickness.

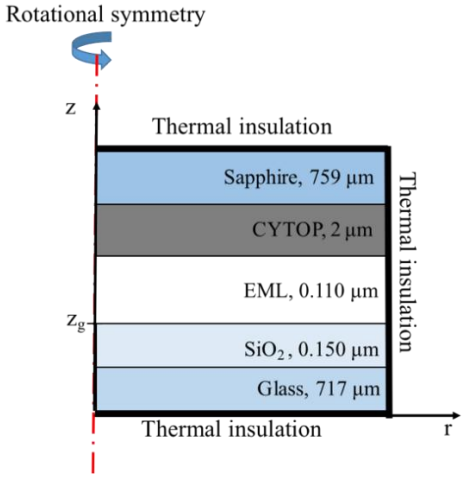

Figure 4-13. Schematic of the geometry of the laser device used for thermal simulation. (The grating is neglected in this simulation)

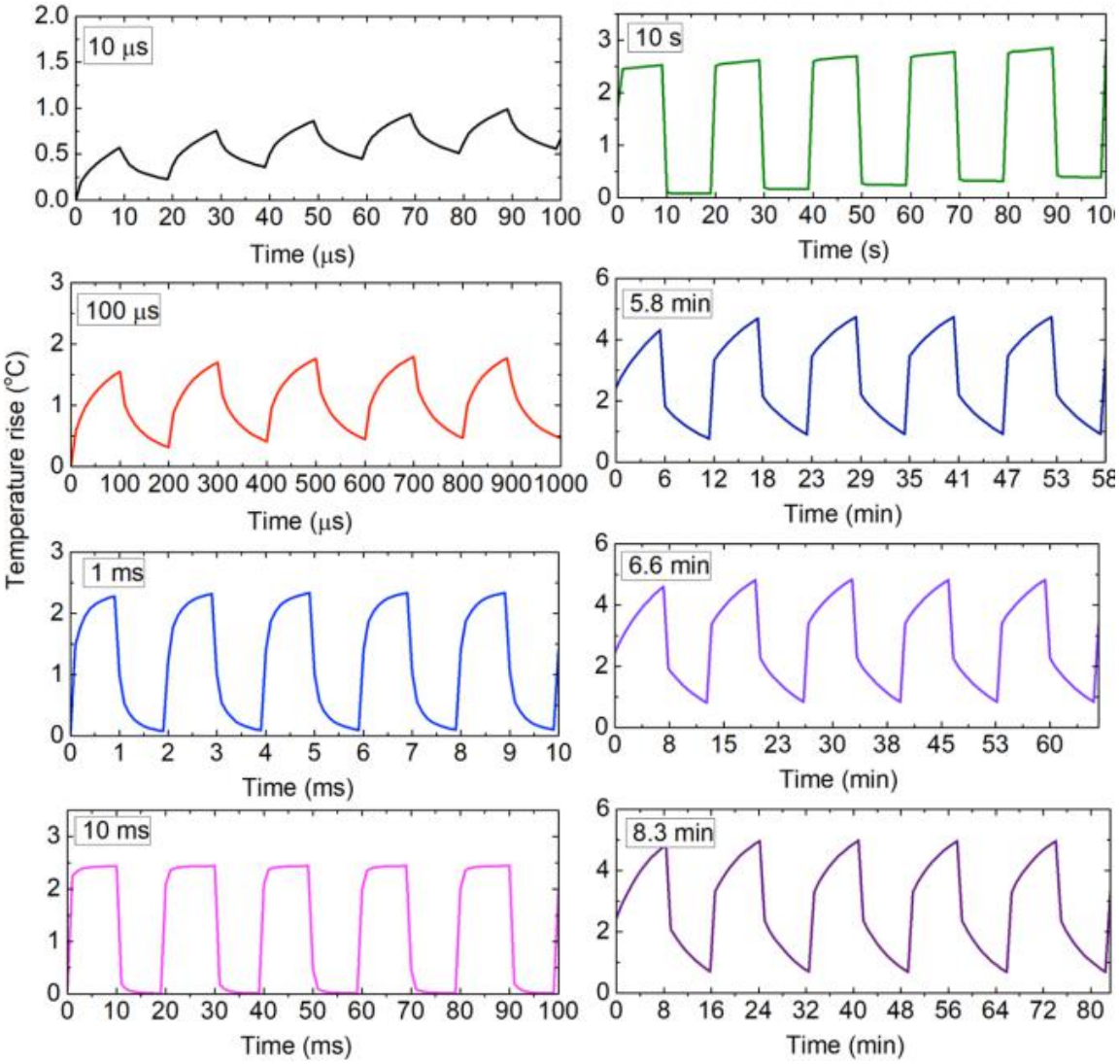

Figure 4-14. Temperature rise in the EML as a function of time for different pulse widths from 10 µs to 500 s (8.3 min).

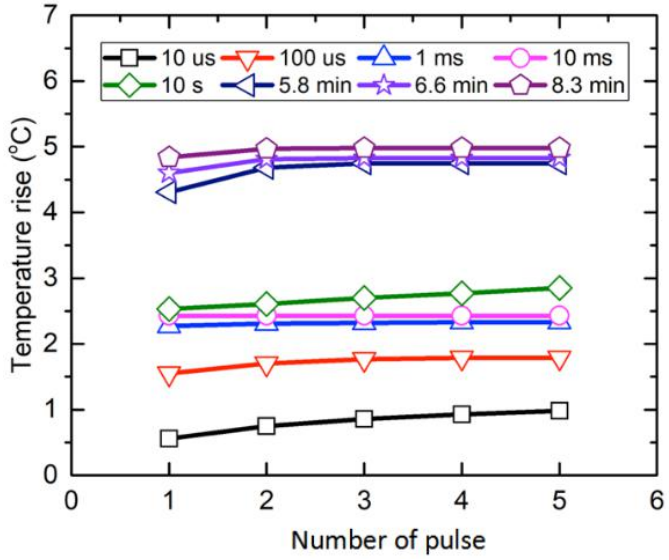

Figure 4-15. Maximum temperature rise at the end of each pulse.

4-4. Conclusion

The exciton-exciton process of TPA-BCm films aimed for lasing was studied. The STA was effectively suppressed under long pulse width because triplet excitons were transferred to singlet exctions incorporated inside the film. Since the suppressed STA can increase the density of singlet excitons, which was the species responsible for high optical gain. The mixed-order DFB could realize low lasing threshold of about 1.28 μJ/cm^2 and the narrow FWHM of about 1.4 nm. The no triplet excited-state absorption at ASE and lasing wavelengths minimized the triplet absorption losses in the resonator. Superior surface-emitting lasing from the devices under quasi-CW operation was obtained with the emission intensity and lasing threshold being dependent of the pulse width. For laser devices studied in this Chapter, the maximum duration time was 100 s and the lowest lasing threshold was about 1.28 μJ/cm^2. However, others effect such as charge carrier mobility and Joule heating etc., are also the important factors and will need further investigation for the realization of current driven NIR OSLDs.

CW lasing in organic thin films is still regarded as a major challenge in organic photonics and is of interest for various applications in the fields of sensing, communication and spectroscopy. Here, I demonstrated organic semiconductor mixed-order DFB lasers that emit in the NIR region and can operate at room temperature in the CW regime for a few minutes, and the borondifluoride curcuminoid derivative used as laser dye in these optically-pumped devices shows negligible triplet losses at the lasing wavelength. This study represents a major step towards the realization of CW OSSLs and might be relevant for the future development of OSLDs related technology.

4-5. References

[1] Z. I. Alzerov, V. M. Andreed, D. Z. Garbuzov, Y. V. Zhilyaev, E. P. Morozov, E. L. Portnoi, and V. G. Trofim, *Sov. Phys. Semicond*., **1971**, 4, 1573.

[2] Z. Yang, M. Pelton, I. Fedin, D. V. Talapin, and E. Waks, *Nat. Commun.*, **2017**, 8, 143.

[3] A. S. D. Sandanayaka, T. Matsushima, F. Bencheikh, K. Yoshida, M. Inoue, T. Fujihara, K. Goushi, J. C. Ribierre, and C. Adachi, *Sci. Adv.*, **2017**, 3, e1602570.

[4] A. S. D. Sandanayaka, K. Yoshidda, M. Inoue, C. J. Qin, K. Goushi, J. C. Ribierre, T. Matsushima, and C. Adachi, *Adv. Opt. Mater.*, **2016**, 4, 834.

[5] L. Zhao, M. Inoue, K. Yoshida, A. S. D. Sandanayaka, J. H. Kim, J. C. Ribierre, and C. Adachi, *IEEE Quantum Electron.*, **2016**, 22, 1300209.

[6] S. Schols, A. Kadashchuk, P. Heremans, A. Helfer, and U. Scherf, *Chem. Phys. Chem.*, **2009**, 10, 1071.

[7] Y. F. Zhang and S. R. Forrest, *Phys. Rev. B*, **2011**, 84, 241301

[8] Z. Y. Yu, Y. S. Wu, L. Xiao, J. W. Chen, Q. Liao, J. N. Yao, and H. B. Fu, *J. Am. Chem. Soc.*, **2017**, 139, 6376.

[9] H. Nakanotani, T. Furukawa, and C. Adachi, *Adv. Opt. Mater.*, **2015**, 3, 1381.

[10] H. Nakanotani, T. Furukawa, T. Hosokai, T. Hatakeyama, and C. Adachi, *Adv. Opt. Mater.*, **2017**, 5, 1700051.

[11] D. H. Kim, A. D'Aléo, X. K. Chen, A. S. D. Sandanayaka, D. D. Yao, L. Zhao, T. Komino, E. Zaborova, G. Canard, Y. Tsuchiya, E. Y. Choi, J. W. Wu, F. Fages, J. L. Brédas, J. C. Ribierre, and C. Adachi, *Nat. Photon.*, **2018**, 12, 98.

[12] F. P. Schäfer, *Dye Lasers*. Springer Publishing: New York, 1973.

[13] S. Forget and S. Chénais, *Organic Solid-State Lasers*. Springer-Verlag: Berlin Heidelberg, 2013.

[14] M. D. McGehee and A. J. Heeger, *Adv. Mater.*, **2000**, 12, 1655.

[15] J. C. Ribierre, G. Tsiminis, S. Richardson, G. A. Turnbull, I. D. W. Samuel, H. S. Barcena, and P. L. Burn, *Appl. Phys. Lett.*, **2007**, 91, 081108.

[16] G. Heliotis, D. D. C. Bradley, G. A. Turnbull, and I. D. W. Samuel, *Appl. Phys. Lett.*, **2002**, 81, 415.

[17] M. Inoue, T. Serevičius, H. Nakanotani, K. Yoshida, T. Matsushima, S. Jursenas, and C. Adachi, *Chem. Phys. Lett.*, **2016**, 644, 62.

[18] D. H. Kim, A. S. D. Sandanayaka, L. Zhao, D. Pitrat, J. C. Mulatier, T. Matsushima, C. Andraud, J. C. Ribierre, and C. Adachi, *Appl. Phys. Lett.*, **2017**, 110, 023303.

[19] M. Inoue, T. Matsushima, H. Nakanotani, and C. Adachi, *Chem. Phys. Lett.*, **2015**, 624, 43.

[20] Z. Zhao, O. Mhibik, T. Leang, S. Forget, and S. Chénais, *Opt. Express.*, **2014**, 22, 30092.

Chapter 5

Summary and perspective

5-1. Summary and perspective

In this thesis, molecular design, synthesis, and properties of highly efficient deep-red and NIR organic luminescent materials were studied toward OLED and CW organic laser applications.

In Chapter 2, a new deep-red ASE from an SQ derivative (*cis*-DCSQ1) was demonstrated by using a host-guest system to suppress aggregation and induce efficient energy transfer. Steady-state and time-resolved PL measurements demonstrated that this dye exhibits highly efficient deep-red emission with a best PLQY of 62% in a doped thin film. At a *cis*-DCSQ1 doping concentration of 0.5 wt%, the lowest ASE threshold was 10 μJ/cm^2 at 687 nm with the optimized thickness. However, the photochemical stability of this dye is poor because of the formation of the free radical that leads to decomposition. Further development should be based on the spectral overlap with a suitable host, keeping the high PLQY with large dipole moment based on the strongly electron withdrawing substituent, and suppressing ACQ. Also, a good thermal and photochemical stability should be considered.

In Chapter 3, a novel dimeric borondifluoride curcuminoid dye was designed and synthesized, because of the good electron withdrawing properties of acetylacetone borondifluoride appended in *meso* position, providing strong vibronic coupling effects between two low-lying excited-states. Steady-state and time-resolved PL measurements demonstrated that this dye exhibits highly efficient NIR TADF emission with a best PLQY of 45% in a doped thin film at the maximum emission wavelength of 760 nm. ASE with a maximum emission wavelength can be tuned between 801 nm and 860 nm, with a threshold as low as 7.5 μJ/cm^2 was observed, providing additional evidence that borondifluoride curcuminoid derivatives are a promising candidate for NIR organic semiconductor lasers. Overall, this study realized high efficiency NIR EL and ASE from TADF curcuminoid derivatives.

In Chapter 4, exciton-exciton annihilation of borondifluoride curcuminoid dye which had the lowest ASE threshold among all materials in this thesis was studied. As the photo-excitation pulse duration was increased up to 1 ms, a gradual increase of the PL intensity was then observed after the initial rapid decrease. It would be probable that the PL intensities gradually increased because populated triplet excitons are converted into singlet excitons via a faster RISC process from the dimer states of blend film, and become dominant over the STA process. Since the suppressed STA can increase the density of singlet excitons, which are the species responsible for high optical gain, a quasi-CW operation longer than 100 s, with the lowest lasing threshold of about 1.28 μJ/cm^2 and the lasing wavelength longer than 700 nm was achieved. Our promising new NIR organic molecule provides a new direction to realize OSLDs.

To design further red-shifted NIR materials, energy-gap tuning should be considered. By increasing the donor ability, the conjugation can be extended, leading to the shallowing of the HOMO level, and decreasing the energy-gap. Further, the introduction of a new NIR functional group should also be considered to develop advanced NIR lasing materials.

Triplet accumulation also needs to be inhibited to enable CW operation of organic lasers. Reduction of triplet accumulation plays an important role in electrically pumped lasers because spin statistics predict that 75% of the generated excitons are triplets and only 25% are singlets upon electrical excitation. As triplets usually do not contribute to lasing and they steeply accumulate in the gain media, resulted in deactivation of lasing. To minimize these losses originating from T_1 population in organic lasers, Adachi group reported a novel method, i.e., TADF assisted fluorescence (TAF) system which employs a TADF molecule as an assistant dopant for a triplet harvester and a fluorescence molecule as an end emitter [1]. By using a TADF molecule as a triplet harvester, lower ASE threshold was achieved.

Although TAF system can be applied, in principle, to reduce the threshold by employing a

suitable TADF molecule as an assistant dopant for triplet harvesting and a fluorescence lasing molecule as an end emitter, the remaining triplet exciton related losses will further limit the system and it is useless to apply the technology to CW OSSLs and OSLDs due to the slow RISC rates. To date, the maximum k_{RISC} of the TADF molecules is around 10^6 s^{-1} [2], meaning that the upconversion process still occurs in the time scale of longer than 1 μs. Thus, it provides insignificant contribution for lasing in the TAF system under pulse operation since lasing always occurs in short time scale within less than a few ns.

The RISC process between the lowest charge transfer triplet excited-state (^{3}CT) and charge transfer singlet excited-state (^{1}CT) is assumed to be very inefficient because of the forbidden SOC, and involving a locally excited triplet state (^{3}LE) in the RISC process between ^{3}CT and ^{1}CT has become a more popular explanation for the dynamic mechanism of RISC processes [3-8]. In this system, k_{RISC} depends on both the rate of vibronic-coupling (VC) between ^{3}CT and ^{3}LE and the SOC between ^{3}LE and ^{1}CT. Here, k_{RISC} can be derived in the framework of the time-dependent second-order Fermi Golden rule using eq. 5-1 [3-6]:

$$k_{RISC} = \frac{2\pi}{\hbar}\left|\frac{\left\langle \Psi_{^1CT}\left|\hat{H}_{SOC}\right|\Psi_{^3LE}\right\rangle\left\langle \Psi_{^3LE}\left|\hat{H}_{VC}\right|\Psi_{^3CT}\right\rangle}{E_{^3CT}-E_{^3LE}}\right|^2 \delta(E_{^1CT}-E_{^3LE}), \qquad \text{(eq. 5-1)}$$

where Ψ means the molecular wave functions of ^{1}CT, ^{3}CT, and ^{3}LE states. $\hat{H}_{SOC}$ and $\hat{H}_{VC}$ are the Hamiltonian describing the coupling between the states. The δ function ensures the conservation of the molecular energy for the nonradiative transition [7]. In order to have a very fast upconversion process, thus, the strength of SOC and VC have to be enhanced significantly. The key to designing TADF materials with high performance is considered as following the D-A system to form intramolecular CT states and the energy gap between ^{3}LE and ^{1}CT should be as small as possible to promote the SOC and then enable the high k_{RISC}. Meanwhile, the energy level of ^{3}CT should be slightly lower than that of ^{3}LE to hinder the ISC process from ^{1}CT to

^{3}CT and enable the VC process between ^{3}CT and ^{3}LE [3]. Recently, it has been proven that the introduction of two different donor units in the TADF emitters is also effective to lower the energy of the high-lying ^{3}LE, in which a good mixing of the ^{3}LE state with the ^{3}CT can facilitate a faster k_{RISC} [8]. By considering above conceptual ideas, the author expect advanced organic luminescent materials will be developed aimed for high efficiency deep-red and NIR OLEDs and low lasing threshold to realize OSLDs in the future.

5-2. References

[1] H. Nakanotani, T. Furukawa, and C. Adachi, *Adv. Opt. Mater.*, **2015**, 3, 1381.

[2] H. Noda, R. Kabe, and C. Adachi, *Chem. Lett.*, **2016**, 45, 1463.

[3] L. Gan, K. Gao, X. Y. Cai, D. C. Chen, and S. J. Su, *J. Phys. Chem. Lett.*, **2018**, 9, 4725.

[4] J. Gibson and T. J. Penfold, *Phys. Chem. Chem. Phys.*, **2017**, 19, 8428.

[5] P. K. Samanta, D. W. Kim, V. Coropceanu, and J. L. Brédas, *J. Am. Chem. Soc.*, **2017**, 139, 4042.

[6] X. K. Chen, D. W. Kim, and J. L. Brédas, *Acc. Chem. Res.*, **2018**, 51, 2215.

[7] T. J. Penfold, E. Gindensperger, C. Daniel, and C. M. Marian, *Chem. Rev.*, **2018**, 118, 6975.

[8] H. Noda, H. Nakanotani, and C. Adachi, *Sci. Adv.*, **2018**, 4, eaao6910.

List of publications

Original papers

1) **H. Ye**, L. S. Cui, T. Matsushima, C. J. Qin, and C. Adachi, *ACS Appl. Mater. Interfaces*, **2018**, 10, 27.

2) **H. Ye**, D. H. Kim, X. K. Chen, A. S. D. Sandanayaka, J. U. Kim, E. Zaborova, G. Canard, Y. Tsuchiya, E. Y. Choi, J. W. Wu, F. Fages, J. L. Brédas, A. D'Aléo, J. C. Ribierre, and C. Adachi, *Chem. Mater*., **2018**, 30, 6702.

3) A. S. D. Sandanayaka*, **H. Ye***, A. D'Aléo, D. H. Kim, F. Bencheikh, P. Sleczkowski, T. Fujihara, E. Zaborova, F. Fages, J. C. Ribierre, and C. Adachi, *To be submitted*. (*: these authors contributes equally)

Co-authored papers

1) M. R. Leyden, T. Matsushima, C. J. Qin, S. B. Ruan, **H. Ye**, and C. Adachi, *Phys. Chem. Chem. Phys.*, **2018**, 20, 15030.

2) G. Y. Li, **H. Ye**, Y. Geng, L. S. Cui, X. H. Ren, J. P. Ma, C. Adachi, and Y. B. Dong, *Revision*.

List of conference

1) **H. Ye**, L. S. Cui, T. Matsushima, C. J. Qin, and C. Adachi, *The 24th International Conference on Science and Technology of Synthetic Metals*, Busan, South Korea, July 1-6, 2018 (Poster).

List of abbreviations

Materials

1,2,3,5-tetrakis(carbazol-9-yl)-4,6-dicyanobenzene (**4CzIPN**)

Aluminum (**Al**)

Tris(8-hydroxyquinoline) aluminum (**Alq_3**)

4,4'-bis[(*N*-carbazole)-styryl]biphenyl (**BSBCz**)

3-(2-benzothiazolyl)-7-(diethylamino)-2*H*-1-benzopyran-2-one (**Coumarin 540**)

4,4'-bis(*N*-carbazolyl)-1,1'-biphenyl (**CBP**)

4-(dicyanomethylene)-2-methyl-6-(4-dimethylaminostyryl)-4*H*-pyran (**DCM**)

4-(dicyanomethylene)-2-methyl-6-julolidyl-9-enyl-4*H*-pyran (**DCM2**)

Bis[2-(diphenylphosphino)phenyl] ether oxide (**DPEPO**)

Indium tin oxide (**ITO**)

Lithium fluoride (**LiF**)

Poly(3-methythiophene) (**P3MT**)

Poly(3,4-ethylene dioxythiophene):poly(styrenesulfonate) (**PEDOT:PSS**)

Bis(2-phenylpyridine)iridium(III) acetylacetonate (**$(ppy)_2Ir(acac)$**)

Perylene diimide (**PDI**)

N,*N*'-di(10-nonadecyl)perylene-3,4:9,10-tetracarboxylic diimide (**PDI-N**)

4,4'-cyclohexylidenebis[*N*,*N*-bis(4-methylphenyl)benzenamine] (**TAPC**)

3-phenyl-4(1'-naphthyl)-5-phenyl-1,2,4-triazole (**TAZ**)

Triphenylamine (**TPA**)

2,2',2''-(1,3,5-benzinetriyl)-tris(1-phenyl-1*H*-benzimidazole) (**TPBi**)

Keywords

Aggregation-caused quenching (**ACQ**)

Atomic force microscope (**AFM**)

Amplified spontaneous emission (**ASE**)

Becke, three-parameter, Lee-Yang-Parr functional (**B3LYP**)

Charge transfer (**CT**)

Cyclic voltammetry (**CV**)

Continuous-wave (**CW**)

Distributed feedback (**DFB**)

Electron-blocking layer (**EBL**)

Electron-injection layer (**EIL**)

Electroluminescence (**EL**)

Emission layer (**EML**)

External quantum efficiency (**EQE**)

Electron-transport layer (**ETL**)

Förster resonance energy transfer (**FRET**)

Full width at half maximum (**FWHM**)

Hole-blocking layer (**HBL**)

Hole-injection layer (**HIL**)

Highest occupied molecular orbital (**HOMO**)

Hole-transport layer (**HTL**)

Internal quantum efficiency (**IQE**)

Intersystem crossing (**ISC**)

Lowest unoccupied molecular orbital (**LUMO**)

Near-infrared (**NIR**)

Nuclear magnetic resonance (**NMR**)

Organic light-emitting diode (**OLED**)

Organic semiconductor laser diode (**OSLD**)

Organic solid-state semiconductor laser (**OSSL**)

Phosphorescent organic light-emitting diode (**PHOLED**)

Photoluminescence (**PL**)

Photoluminescence quantum yield (**PLQY**)

Quantum dot (**QD**)

Research and development (**R&D**)

Reverse intersystem crossing (**RISC**)

Spin-orbit coupling (**SOC**)

Squaraine (**SQ**)

Singlet-singlet annihilation (**SSA**)

Singlet-triplet annihilation (**STA**)

Thermally-activated delayed fluorescence (**TADF**)

Thermally-activated delayed fluorescence assisted fluorescence (**TAF**)

Time-dependent density functional theory (**TD-DFT**)

Transition dipole moments (**TDM**)

Transverse electric (**TE**)

Transverse magnetic (**TM**)

Triplet-triplet annihilation (**TTA**)

Vibronic-coupling (**VC**)

Variable stripe length (**VSL**)

Physical symbols

Absorption coefficient (β)

Absorption wavelength (λ_{abs})

ASE/laser threshold (E_{th})

Boltzmann constant (k_B)

Charge carrier balance factor (η_r)

Charge displacement (r)

Charge transfer singlet excited-state (^1CT)

Confinement factor (Γ)

Constant (C')

Distance travelled in the gain medium (l)

Effective refractive index in an emission region (n_{eff})

Einstein's B coefficient (B)

Electronic state m (ψ_m)

Electronic state n (ψ_n)

Elementary charge (e)

Emission cross-section (σ_{em})

Energy difference between potential minima of singlet and triplet states (ΔE_{ST})

External quantum efficiency (η_{ext})

Frequency of light (ν)

Gain coefficient ($g(\lambda)$)

Heat capacity (C_p)

Intersystem crossing rate (k_{ISC})

Light outcoupling factor (η_{out})

Locally excited triplet state ($^3\boldsymbol{LE}$)

Loss coefficient ($\boldsymbol{a}$)

Lowest charge transfer triplet excited-state ($^3\boldsymbol{CT}$)

Lowest singlet excited-state ($\boldsymbol{S_1}$)

Lowest triplet excited-state ($\boldsymbol{T_1}$)

Material density ($\boldsymbol{\rho}$)

Nonradiative decay rate ($\boldsymbol{k_{nr}}$)

Order of diffraction process ($\boldsymbol{n}$)

Oscillator strength ($\boldsymbol{f}$)

Period of grating ($\boldsymbol{\Lambda}$)

Photoluminescence wavelength ($\boldsymbol{\lambda_{PL}}$)

Photoluminescence quantum yield ($\boldsymbol{\Phi_{PL}}$)

Photoluminescence lifetime ($\boldsymbol{\tau}$)

Planck's constant ($\boldsymbol{h}$)

Radiative decay rate ($\boldsymbol{k_r}$)

Reverse intersystem crossing rate ($\boldsymbol{k_{RISC}}$)

Singlet ground-state ($\boldsymbol{S_0}$)

Spin statistics factor ($\boldsymbol{\chi}$)

Steady-state absorption cross-section ($\boldsymbol{\sigma_a}$)

Steady-state population of the T_1 state ($\boldsymbol{T_1^{ss}}$)

Steady-state population of the S_1 state ($\boldsymbol{S_1^{ss}}$)

Stokes shift ($\boldsymbol{\Delta\nu}$)

Temperature ($\boldsymbol{T}$)

Thermal conductivity ($\boldsymbol{k}$)

Transition dipole moment ($\boldsymbol{\mu}$)

Triplet absorption cross-section ($\boldsymbol{\sigma_{TT}}$)

Triplet lifetime ($\boldsymbol{\tau_T}$)

Voltage ($\boldsymbol{V}$)

Velocity of light ($\boldsymbol{c}$)

Wavelength ($\boldsymbol{\lambda}$)

Acknowledgements

I would like to thank my advisor Professor Chihaya Adachi for accepting me into his group, for being so patient throughout the entire duration of my graduate student life, thesis revision, and for granting me unparalleled freedom to conduct scientific research. When I looked back, I found my research direction was not clear, and I spent a lot of time to synthesis many molecules which seemed to be imperfect now. To rearrange the topic, Prof. Adachi kindly suggested me to focus on deep-red and NIR organic luminescent materials for OLED and laser. Without this and the excellent experimental environment, the work described herein would not have been possible. I do not know how to return his favor now, but I will surely carry on the spirit of always avoiding careless mistakes, thinking originality and acting passionate for the research and life.

I also deeply grateful to the other members of my committee, Professor Hiroyuki Furuta and Professor Yuji Oki for serving on my dissertation committee and their kindly, helpful suggestions and comments on my presentation and thesis.

I would also like to thank Associate Professor Toshinori Matsushima for kindly revising my first paper and give me many support during this past years, Associate Professor Hajime Nakanotani for kindly revisions and comments on my study and presentations, Associate Professor Sandanayaka Sangarabge Don Atula for night lab life and help on experiments, especially for work related to laser, Associate Professor Youichi Tsuchiya for discussions on my study, Assistant Professor Kenichi Goushi for always great help for measurement, instrumentation, data analysis, Assistant Professor Chuanjiang Qin for teaching me synthesis and kindly help on preparing my first paper, Assistant Professor Ryota Kabe for kindly suggestions and comments during my study since my first R-MTG, Assistant Professor Masashi Mamada for great help on synthesis and discussions, Assistant Professor Takeshi

Komino for kindly teach me how to use the EQE system and theory discussions, Dr. Takashi Fujihara for great help on distributed bragg reflector fabrication and setting laser system.

In addition, I also special thank my collaborators Associate Professor Anthony D'Aléo from Aix-Marseille Université, France and Professor Jean-Charles Ribierre, without their help, the work on Chapter 3 and 4 will not be presented here. And also thank Prof. Ribierre and my previous advisor Associate Professor Soonmin Seo from Gachon University, South Korea and Assistant Professor Ju-Hyung Kim from Ajou University, South Korea for recommending me to study in this great lab. It helps me to learn and improve more during my study here. It will be great help for my future academic career.

Furthermore, I am also indebted to all my fellow Adachineses for offering their help and advice whenever I was in need. Dr. Yang Geng, Dr. Kou Yoshida, Dr. Munetomo Inoue, Dr. Li Zhao, Dr. Linsong Cui, Dr. Daehyeon Kim, Dr. Sunbin Hwang, Dr. Inseob Park, Dr. Hiroyuki Mieno, Dr. William J. Potscavage, Dr. Fatima Bencheikh, Dr. Matthew Leyden, Dr. Chin-Yiu Chan, Dr. Morgan Auffray, Dr. Umamahesh Balijapalli, Dr. Yiu Wing Wong, Dr. Ryutaro Komatsu, Dr. Gabseok Seo, Mr. Ko Inada, Mr. Jonguk Kim, Mr. Hiroki Noda, Mr. Taro Furukawa, Mr. Zesen Lin, Mr. MD Ashadul Islam, Mr. Masayuki Yokoyama, Mr. Naoto Noutsuka, Mr. Yu Esaki, Mr. Ganbaatar Tumen-Ulzii, Mr. Buddhika Sanjeewa Bandara Karunathilaka, Mr. Tai Cheng, Mr. Kazuya Jinnai, Mr. Ryo Nagata, Mr. Hiroya Arai, Ms. Momoka Miyajima, Mr. Yuu Shihara, Mr. Muhammad Hasnan Sazzad, Mr. Shibin Ruan, Mr. Toshiya Fukunaga, Mr. Satoshi Maedera, Mr. Nguyen Thanh Ba, and all other students.

And I also want to thank all the staffs of Adachi lab for kindly support on my life, study and experiments. Especially to Ms. Mayumi Kudo, Ms. Rei Sasagawa and Ms. Hiroko Kuratomi for their always kindly assistance on study and life, Ms. Keiko Kusuhara, Ms. Nozomi Nakamura, Ms. Shinobu Terakawa for their kindly help on technical support.

My research and work in this thesis owe their existence to the influence of all the members of Adachi laboratory and all persons who I met through this three and half years.

Finally, I would like to thank Ministry of Education, Culture, Sports, Science and Technology (MEXT) and Japan Science and Technology Agency (JST), ERATO, Adachi Molecular Exciton Engineering Project for financially support that made it possible to complete this study. I would also like to express my gratitude to my parents and my older brother for their moral support and unwavering love. Last but not least, I express my gratitude to my wife with all her love and support, and also for showing infinite patience in waiting for me to graduate. I can only regret the fact that my hectic research schedule had taken away a lot of the time and attention that she rightfully deserves. I dedicate this thesis to them, and hope that whatever I have accomplished to date and in the future will stand testimony to the fact that all their hard work and sacrifice over the years have not been in vain.

January. 2019

Hao Ye